UNIVERSITY OF CALGARY

Probing Trapped Antihydrogen: *In Situ* Diagnostics and Observations of Quantum Transitions

by

Timothy Peter Friesen

A THESIS
SUBMITTED TO THE FACULTY OF GRADUATE STUDIES
IN PARTIAL FULFILLMENT OF THE REQUIREMENTS FOR THE
DEGREE OF DOCTORATE OF PHILOSOPHY

DEPARTMENT OF PHYSICS AND ASTRONOMY

CALGARY, ALBERTA

January, 2014

Abstract

Antihydrogen, the bound state of a positron and an antiproton, is the simplest pure anti-atomic system and an excellent candidate to test the symmetry between matter and antimatter. This thesis focuses on the magnetic confinement of antihydrogen and the first ever resonant interaction with trapped antihydrogen, as performed by the ALPHA collaboration.

The ALPHA apparatus and the techniques that have been developed to form, trap, probe, and detect antihydrogen atoms will be described in detail. The first successful demonstration of trapped antihydrogen will then be described. In the initial demonstrations, 38 trapped antihydrogen atoms were detected after being confined for at least 172 ms. Since then, over 400 antihydrogen atoms have been trapped and confinement times of 1000 s (over 15 minutes) have been demonstrated.

Spectroscopy of these trapped antihydrogen atoms is the next major step forward. As an initial proof-of-principle demonstration, ALPHA induced and observed resonant positron spin flip (PSR) transitions between the ground states of antihydrogen. Because of the strong magnetic field dependence of these transition frequencies, the success of this experiment relied heavily on the ability to measure the magnetic field seen by the antihydrogen atoms. A novel method to measure the magnetic field *in situ* by detecting the cyclotron resonance of a trapped electron plasma is presented. This method allowed ALPHA to measure the magnetic field strength at the minimum of the magnetic antihydrogen trap to within 1.4 parts in 10^3. Hardware improvements and further study should allow this resolution to be improved by several orders of magnitude. The cyclotron resonance measurements can also be applied as a rough diagnostic of a microwave field within the ALPHA apparatus. This allowed for important diagnostics of the microwave field used to excite the PSR transitions. Finally, the experimental results demonstrating resonant PSR transitions in antihydrogen are presented. This experiment is the first ever spectroscopic measurement of antihydrogen and an important step towards future precision spectroscopy.

Acknowledgements

Working with ALPHA has been a great experience and was an incredible opportunity. At times exhausting but always rewarding. I want to thank all of the past and present members of the ALPHA collaboration that I have had the fortune to work with. To the senior scientists, including Prof. Joel Fajans, Prof. Jeff Hangst, Dr. Paul Bowe, Dr. Eli Sarid, Prof. Mike Charlton, Prof. Niels Madsen, Prof. Scott Menary, Prof. Art Olin, Dr. Dave Gill, and Prof. Francis Robicheaux, I have learned a great deal from each of you and have always appreciated the respect you have shown me and my fellow students. In particular, I must thank Prof. Walter Hardy and Prof. Mike Hayden. You have been an absolute pleasure to work with and have provided me much needed help and guidance time and time again. Without you, this work would not have been possible.

Special thanks, as well, to my supervisors Prof. Makoto Fujiwara and Prof. Robert Thompson. Makoto, your knowledge, enthusiasm, and tenacity have been a source of inspiration and motivation. Without your persistence and encouragement plasma modes may not have found their use in ALPHA and this thesis would look very different. Robert, I am extremely grateful for all of the support and guidance that you have given me from the beginning. It has been a pleasure working with and learning from both of you.

Thanks to all my fellow students and post-docs in ALPHA. Mohammad Dehghani Ashkezari, Will Bertsche, Eoin Butler, Richard Hydomako, Andrea Gutierrez, Andrea

Capra, Andrew Humphries, Arielle Little, Joseph Mckenna, Rodrigo Sacremento, Simone Stracka, Chanpreet Amole, Marcelo Baquero-Ruiz, Daniel de Miranda Silviera, James Storey, Petteri Pusa, Gorm Bruun Andresen, Tim Tharp, Chukman So, and Adam Deller, I could not have survived without you. You are all awesome.

Thanks my family for their continued love and support. More than anyone, I owe you for any success I have had or will have in the future. Thank you for standing by me even when I make poor life decisions like going to grad school.

Finally, to Itzel Lucio Martínez to whom I owe so much. It has been a long journey. Being away from you for such long stretches was excruciating, but your love and support kept me going. Without you, my sanity would have left me a long time ago. Thank you.

Publications

The following list contains the ALPHA papers published during the author's Ph.D. program. Following ALPHA collaboration policy, the authors are listed in alphabetic order.

1. C. Amole, M. D. Ashkezari, M. Baquero-Ruiz, W. Bertsche and E. Butler, A. Capra, C. L. Cesar, M. Charlton, A. Deller, N. Evetts, S. Eriksson, J. Fajans, **T. Friesen** and M. C. Fujiwara, D. R. Gill, A. Gutierrez, J. S. Hangst and W. N. Hardy, M. E. Hayden, C. A. Isaac, S. Jonsell and L. Kurchaninov, A. Little, N. Madsen, J. T. K. McKenna and S. Menary, S.C. Napoli, K. Olchanski, A. Olin, P. Pusa and C.Ø. Rasmussen, F. Robicheaux, E. Sarid, D. M. Silveira and C. So, S. Stracka, T. Tharp, R. I. Thompson, D. P. van der Werf, J. S. Wurtele. *In situ electromagnetic field diagnostics with an electron plasma in a Penning-Malmberg trap,* New J. Phys. **14**, 013037 (2014).
`http://dx.doi.org/10.1088/1367-2630/16/1/013037`

2. C. Amole, G.B. Andresen, M.D. Ashkezari, M. Baquero-Ruiz, W. Bertsche, P.D. Bowe, E. Butler, A. Capra, P.T. Carpenter, C.L. Cesar, S. Chapman, M. Charlton, A. Deller, S. Eriksson, J. Escallier, J. Fajans, **T. Friesen**, M.C. Fujiwara, D.R. Gill, A. Gutierrez, J.S. Hangst, W.N. Hardy, R.S. Hayano, M.E. Hayden, A.J. Humphries, J.L. Hurt, R. Hydomako, C.A. Isaac, M.J. Jenkins, S. Jonsell, L.V. Jørgensen, S.J. Kerrigan, L. Kurchaninov, N. Madsen, A. Marone, J.T.K. McKenna, S. Menary, P. Nolan, K. Olchanski, A. Olin, B. Parker, A. Povilus, P. Pusa, F. Robicheaux, E. Sarid, D. Seddon, S. Seif El Nasr, D.M. Silveira, C. So, J.W. Storey, R.I. Thompson, J. Thornhill, D. Wells, D.P. van der Werf, J.S. Wurtele, Y. Yamazaki, *The ALPHA Antihydrogen Trapping Apparatus,* Nucl. Instrum. Meth. A **735**, 319 (2014).
`http://dx.doi.org/10.1016/j.nima.2013.09.043`

3. C. Amole, M. D. Ashkezari, M. Baquero-Ruiz, W. Bertsche, E. Butler, A. Capra, C. L. Cesar, S. Chapman, M. Charlton, S. Eriksson, J. Fajans, **T. Friesen**, M. C. Fujiwara, D. R. Gill, A. Gutierrez, J. S. Hangst, W. N. Hardy, M. E. Hayden, C. A. Isaac, S. Jonsell, L. Kurchaninov, A. Little, N. Madsen, J. T. K. McKenna, S. Menary, S. C. Napoli, P. Nolan, K. Olchanski, A. Olin, A. Povilus, P. Pusa, C.Ø. Rasmussen, F. Robicheaux, E. Sarid, D. M. Silveira, S. Stracka, C. So, R. I. Thompson, M. Turner, D. P. van der Werf, J. S. Wurtele, A. Zhmoginov. *Autoresonant-Spectrometric Determination Of The Residual Gas Composition*

In The ALPHA Experiment Apparatus, Rev. Sci. Instrum. **84**, 065110 (2013).
`http://dx.doi.org/10.1063/1.4811527`

4. C. Amole, M.D. Ashkezari, M. Baquero-Ruiz, W. Bertsche, E. Butler, A. Capra, C.L. Cesar, M. Charlton, S. Eriksson, J. Fajans, **T. Friesen**, M.C. Fujiwara, D.R. Gill, A. Gutierrez, J.S. Hangst, W.N. Hardy, M.E. Hayden, C.A. Isaac, S. Jonsell, L. Kurchaninov, A. Little, N. Madsen, J.T.K. McKenna, S. Menary, S.C. Napoli, P. Nolan, A. Olin, P. Pusa, C.Ø. Rasmussen, F. Robicheaux, E. Sarid, D.M. Silveira, C. So, R.I. Thompson, D.P. van der Werf, J.S. Wurtele, A.I. Zhmoginov, A.E. Charman. *Description And First Application Of A New Technique To Measure The Gravitational Mass Of Antihydrogen,* Nat. Commun. **4**, 1785 (2013).
   `http://dx.doi.org/10.1038/ncomms2787`

5. **T. Friesen**, C. Amole, M. D. Ashkezari, M. Baquero-Ruiz, W. Bertsche, P. D. Bowe, E. Butler, A. Capra, C. L. Cesar, M. Charlton, A. Deller, N. Evetts, S. Eriksson, J. Fajans, M. C. Fujiwara, D. R. Gill, A. Gutierrez, J. S. Hangst, W. N. Hardy, M. E. Hayden, C. A. Isaac, S. Jonsell, L. Kurchaninov, A. Little, N. Madsen, J. T. K. McKenna, S. Menary, S. C. Napoli, K. Olchanski, A. Olin, P. Pusa, C. Ø. Rasmussen, F. Robicheaux, E. Sarid, D. M. Silveira, C. So, S. Stracka, R. I. Thompson, D. P. van der Werf, and J. S. Wurtele. *Electron plasmas as a diagnostic tool for hyperfine spectroscopy of antihydrogen,* AIP Conf. Proc. **1521**, 123 (2013).
   `http://dx.doi.org/10.1063/1.4796068`

6. C. Amole, M. D. Ashkezari, M. Baquero-Ruiz, W. Bertsche, E. Butler, A. Capra, C. L. Cesar, M. Charlton, A. Deller, S. Eriksson, J. Fajans, **T. Friesen**, M. C. Fujiwara, D. R. Gill, A. Gutierrez, J. S. Hangst, W. N. Hardy, M. E. Hayden, C. A. Isaac, S. Jonsell, L. Kurchaninov, A. Little, N. Madsen, J. T. K. McKenna, S. Menary, S. C. Napoli, K. Olchanski, A. Olin, P. Pusa, C.Ø. Rasmussen, F. Robicheaux, E. Sarid, C. R. Shields, D. M. Silveira, C. So, S. Stracka, R. I. Thompson, D. P. van der Werf, J. S. Wurtele, A. Zhmoginov, and L. Friedland. *Experimental And Computational Study Of The Injection Of Antiprotons Into A Positron Plasma For Antihydrogen Production,* Phys. Plasmas **20**, 043510 (2013).
   `http://dx.doi.org/10.1063/1.4801067`

7. **T. Friesen**, G. B. Andresen, M. D. Ashkezari, M. Baquero-Ruiz, W. Bertsche, P. D. Bowe, E. Butler, C. L. Cesar, S. Chapman, M. Charlton, S. Eriksson, J. Fajans, M. C. Fujiwara, D. R. Gill, A. Gutierrez, J. S. Hangst, W. N. Hardy, R. S. Hayano, M. E. Hayden, A. J. Humphries, R. Hydomako, S. Jonsell, L. Kurchaninov, N. Madsen, S. Menary, P. Nolan, K. Olchanski, A. Olin, A. Povilus, P. Pusa, F. Robicheaux, E. Sarid, D. M. Silveira, C. So, J. W. Storey, R. I. Thompson, D. P. van der Werf, J. S. Wurtele, Y. Yamazaki. *Microwave-plasma interactions studied via mode diagnostics in ALPHA,* Hyperfine Interac. **212**,

117 (2012).
`http://dx.doi.org/10.1007/s10751-012-0585-8`

8. G.B. Andresen, M.D. Ashkezari, W. Bertsche, P.D. Bowe, E. Butler, C.L. Cesar, S. Chapman, M. Charlton, A. Deller, S. Eriksson, J. Fajans, **T. Friesen**, M.C. Fujiwara, D.R. Gill, A. Gutierrez, J.S. Hangst, W.N. Hardy, M.E. Hayden, R.S. Hayano, A.J. Humphries, R. Hydomako, S. Jonsell, L.V. Jørgensen, L. Kurchaninov, N. Madsen, S. Menary, P. Nolan, K. Olchanski, A. Olin, A. Povilus, P. Pusa, E. Sarid, S. Seif el Nasr, D.M. Silveira, C. So, J.W. Storey, R.I. Thompson, D.P. van der Werf and Y. Yamazaki. *Antihydrogen annihilation reconstruction with the ALPHA silicon detector,* Nucl. Instrum. Meth. A **684**, 73 (2012).
`http://dx.doi.org/10.1016/j.nima.2012.04.082`

9. C. Amole, M.D. Ashkezari, M. Baquero-Ruiz, W. Bertsche, P.D. Bowe, E. Butler, A. Capra, C.L. Cesar, M. Charlton, A. Deller, P.H. Donnan, S. Eriksson, J. Fajans, **T. Friesen**, M.C. Fujiwara, D.R. Gill, A. Gutierrez, J.S. Hangst, W.N. Hardy, M.E. Hayden, A.J. Humphries, C.A. Isaac, S. Jonsell, L. Kurchaninov, A. Little, N. Madsen, J.T.K. McKenna, S. Menary, S.C. Napoli, P. Nolan, K. Olchanski, A. Olin, P. Pusa, C.Ø. Rasmussen, F. Robicheaux, E. Sarid, C. R. Shields, D.M. Silveira, S. Stracka, C. So, R.I. Thompson, D.P. van der Werf and J.S. Wurtele. *Resonant Quantum Transitions in Trapped Antihydrogen Atoms,* Nature **483**, 439 (2012).
`http://dx.doi.org/10.1038/nature10942`

10. C. Amole, G. B. Andresen, M. D. Ashkezari, M. Baquero-Ruiz, W. Bertsche, E. Butler, C. L. Cesar, S. Chapman, M. Charlton, A. Deller, S. Eriksson, J. Fajans, **T. Friesen**, M. C. Fujiwara, D. R. Gill, A. Gutierrez, J. S. Hangst, W. N. Hardy, M. E. Hayden, A. J. Humphries, R. Hydomako, L. Kurchaninov, S. Jonsell, N. Madsen, S. Menary, P. Nolan, K. Olchanski, A. Olin, A. Povilus, P. Pusa, F. Robicheaux, E. Sarid, D. M. Silveira, C. So, J. W. Storey, R. I. Thompson, D. P. van der Werf and J. S. Wurtele. *Discriminating between antihydrogen and mirror-trapped antiprotons in a minimum-B trap,* New J. Phys. **14**, 105010 (2012).
`http://dx.doi.org/10.1088/1367-2630/14/1/015010`

11. G. B. Andresen, M. D. Ashkezari, M. Baquero-Ruiz, W. Bertsche, P. D. Bowe, E. Butler, C. L. Cesar, M. Charlton, A.Deller, S. Eriksson, J. Fajans, **T. Friesen**, M. C. Fujiwara, D. R. Gill, A. Gutierrez, J. S. Hangst, W. N. Hardy, R. S. Hayano, M. E. Hayden, A. J. Humphries, R. Hydomako, S. Jonsell, S. L. Kemp, L. Kurchaninov, N. Madsen, S. Menary, P. Nolan, K.Olchanski, A. Olin, P. Pusa, C.Ø. Rasmussen, F. Robicheaux, E. Sarid, D. M. Silveira, C. So, J. W. Storey, R. I. Thompson, D. P. van der Werf, J. S. Wurtele and Y. Yamazaki. *Confinement of antihydrogen for 1,000 seconds,* Nature Phys. **7**, 558 (2011).
`http://dx.doi.org/10.1038/nphys2025`

12. G. B. Andresen, M. D. Ashkezari, M. Baquero-Ruiz, W. Bertsche, P. D. Bowe, E. Butler, C. L. Cesar, S. Chapman, M. Charlton, A. Deller, S. Eriksson, J. Fajans, **T. Friesen**, M. C. Fujiwara, D. R. Gill, A. Gutierrez, J. S. Hangst, W. N. Hardy, M. E. Hayden, A. J. Humphries, R. Hydomako, S. Jonsell, N. Madsen, S. Menary, P. Nolan, A. Olin, A. Povilus, P. Pusa, F. Robicheaux, E. Sarid, D. M. Silveira, C. So, J. W. Storey, R. I. Thompson, D. P. van der Werf, J. S. Wurtele, and Y Yamazaki. *Centrifugal separation and equilibration dynamics in an electron-antiproton plasma,* Phys. Rev. Lett. **106**, 145001 (2011).
`http://dx.doi.org/10.1103/PhysRevLett.106.145001`

13. G. B. Andresen, M. D. Ashkezari, M. Baquero-Ruiz, W. Bertsche, P. D. Bowe, E. Butler, P. T. Carpenter, C. L. Cesar, S. Chapman, M. Charlton, J. Fajans, **T. Friesen** , M. C. Fujiwara, D. R. Gill, J. S. Hangst, W. N. Hardy, M. E. Hayden, A. J. Humphries, R. Hydomako, J. L. Hurt, S. Jonsell, N. Madsen, S. Menary, P. Nolan, K. Olchanski, A. Olin, A. Povilus, P. Pusa, F. Robicheaux, E. Sarid, D. M. Silveira, C. So, J. W. Storey, R. I. Thompson, D. P. van der Werf, J. S. Wurtele, and Y. Yamazaki. *Autoresonant excitation of antiproton plasmas,* Phys. Rev. Lett **106**, 025002 (2011).
`http://dx.doi.org/10.1103/PhysRevLett.106.025002`

14. G. B. Andresen, M. D. Ashkezari, M. Baquero-Ruiz, W. Bertsche, P. D. Bowe, C. C. Bray, E. Butler, C. L. Cesar, S. Chapman, M. Charlton, J. Fajans, **T. Friesen**, M. C. Fujiwara, D. R. Gill, J. S. Hangst, W. N. Hardy, R. S. Hayano, M. E. Hayden, A. J. Humphries, R. Hydomako, S. Jonsell, L. V. Jørgensen, L., Kurchaninov , R. Lambo, N. Madsen, S. Menary, P. Nolan, K. Olchanski, A. Olin, A. Povilus, P. Pusa, F. Robicheaux, E. Sarid, S. Seif El Nasr, D. M. Silveira, C. So, J. W. Storey, R. I. Thompson, D. P. van der Werf, D. Wilding, J. S. Wurtele, and Y. Yamazaki. *Search for Trapped Antihydrogen,* Phys. Lett. B **695**, 95 (2011).
`http://dx.doi.org/10.1016/j.physletb.2010.11.004`

15. G. B. Andresen, M. D. Ashkezari, M. Baquero-Ruiz, W. Bertsche, P. D. Bowe, E. Butler, C. L. Cesar, S. Chapman, M. Charlton, A. Deller, S. Eriksson, J. Fajans, **T. Friesen**, M. C. Fujiwara, D. R. Gill, A. Gutierrez, J. S. Hangst, W. N. Hardy, M. E. Hayden, A. J. Humphries, R. Hydomako, M. J. Jenkins, S. Jonsell, L. V. Jørgensen, L. Kurchaninov, N. Madsen, S. Menary, P. Nolan, K. Olchanski, A. Olin, A. Povilus, P. Pusa, F. Robicheaux, E. Sarid, S. Seif El Nasr, D.M. Silveira, C. So, J.W. Storey, R. I. Thompson, D. P. van der Werf, J. S. Wurtele, and Y. Yamazaki. *Trapped antihydrogen,* Nature **468**, 673 (2010).
`http://dx.doi.org/10.1038/nature09610`

16. G. B. Andresen, M. D. Ashkezari, M. Baquero-Ruiz, W. Bertsche, P. D. Bowe, E. Butler, C. L. Cesar, S. Chapman, M. Charlton, J. Fajans, **T. Friesen**, M. C. Fujiwara, D. R. Gill, J. S. Hangst, W. N. Hardy, R. S.Hayano, M. E. Hayden, A. Humphries, R. Hydomako, S. Jonsell, L. Kurchaninov, R. Lambo, N. Madsen, S. Menary, P. Nolan, K. Olchanski, A. Olin, A. Povilus, P. Pusa, F. Robicheaux, E.

Sarid, D. M. Silveira, C. So, J. W. Storey, R. I. Thompson, D. P. van der Werf, D. Wilding, J. S. Wurtele, and Y. Yamazaki. *Evaporative cooling of antiprotons to cryogenic temperatures,* Phys. Rev. Lett. **105**, 013003 (2010).
`http://dx.doi.org/10.1103/PhysRevLett.105.013003`

Table of Contents

List of Tables

List of Figures

List of Symbols, Abbreviations and Nomenclature

Acronym	**Definition**
AD	Antiproton Decelerator
AEgIS	Antimatter Experiment: Gravity, Interferometry, Spectroscopy
ALPHA	Antihydrogen Laser PHysics Apparatus
ASACUSA	Atomic Spectroscopy And Collisions Using Slow Antiprotons
ATRAP	Antihydrogen Trap
CCD	Charge-Coupled Device
CERN	European Organization for Nuclear Research
CMEF	Co-rotating Microwave Electric Field
COM	Centre of Mass
ELENA	Extra Low ENergy Antiprotons
Fermilab	Fermi National Accelerator Laboratory
FPGA	Field Programmable Gate Array
GBAR	Gravitational Behaviour of Antihydrogen at Rest
LEAR	Low Energy Antiproton Ring
MCP	Multi-Channel Plate
NMR	Nuclear Magnetic Resonance
PSR	Positron Spin Resonance
TE	Transverse Electric
TM	Transverse Magnetic
TTL	Transistor-transistor logic
UHV	Ultra-high vacuum

Table 0.1: List of acronyms.

Symbol	**Definition**
(x, y, z)	Cartesian coordinates
(r, θ, z)	Cylindrical coordinates
$H/\bar{H}$	Hydrogen/Antihydrogen
$p/\bar{p}$	Proton/Antiproton
e^-/e^+	Electron/Positron
$\vec{B}$	Magnetic field
$\vec{E}$	Electric field

V_0	Applied Electric potential
d	Penning trap geometric factor
m	Particle mass
q	Particle electric charge
ω_c	Cyclotron frequency
ω_z	Axial bounce frequency
ω_-	Magnetron frequency
ω_+	Modified cyclotron frequency
$\vec{\mu}$	Magnetic dipole moment
U	Potential energy
g_J	Lande g-factor
μ_B	Bohr magneton
$\hbar$	Reduced Planck constant
$\vec{J}$	Total angular momentum vector
S	Spin angular momentum
ΔU	Magnetic trap depth
$I(\vec{r}$	Intensity distribution fit function
ω_p	Plasma oscillation frequency
n	Plasma number density
ϵ_0	Vacuum permittivity
λ_D	Debye Length
T	Temperature
k_B	Boltzmann's constant
$\phi(\vec{r})$	Electric potential
$\phi_T(\vec{r})$	Applied trap potential
$\phi_P(\vec{r})$	Plasma self-potential
$p_{r_j}, p_{\theta_j}, p_{z_j}$	Canonical momenta
P_θ, L	Total canonical angular momentum
Γ	Plasma coupling parameter
a	Inter-particle spacing
ω_r	Plasma rotation frequency
L_p	Plasma major axis length
r_p	Plasma semi-minor axis length
α	Plasma aspect ratio
$Q_\ell^m(x)$	Associated Legendre function of the second kind
r_c	Cyclotron radius
b	Distance of closest approach
$T_{\|\|}$	Temperature parallel to the magnetic field
$T_\perp$	Temperature perpendicular to magnetic field
Γ_col	Equipartition rate between parallel and perpendicular temperatures
P_ℓ	Legendre function of the first kind
Q_ℓ	Legendre function of the second kind
ω_2	Angular quadrupole frequency
$E_{\|\|}$	Kinetic energy parallel to the magnetic field
$E_\perp$	Kinetic energy perpendicular to the magnetic field

c	Speed of light
$v_\perp$	Particle velocity perpendicular to the magnetic field
$a_\perp$	Particle acceleration perpendicular to the magnetic field
τ_c	Characteristic cyclotron cooling time
τ_{net}	Net plasma cooling time
η	Evaporative cooling well depth
κ	Excess kinetic energy of an evaporating particle
α_{ev}	Evaporative cooling efficiency
N	Number of particles
γ	Rate of particle loss due to non-evaporation processes
τ_{col}	Antiproton-antiproton collision time
τ_{ev}	Evaporation time
R	Measured radius
σ_{SRR}	Spontaneous radiative recombination cross-section
α_{fs}	Fine structure constant
a_0	Bohr radius
E_{g}	Ground state binding energy
E_{e^+}	Positron kinetic energy
Γ_{SRR}	Spontaneous radiative recombination rate
Γ_{TBR}	Three-body recombination rate
f_2	Quadrupole mode frequency
ΔT	Change in plasma temperature
F_P	Purcell factor
Q	Quality factor
λ_c	Cyclotron wavelength
V	Cavity volume
$\Delta f_{c,\ell}$	Frequency shift of plasma cyclotron modes
f_d	Diocotron frequency
Δf_{FWHM}	Cyclotron resonance full-width at half maximum
$B_z(z,r)$	Mirror coil magnetic field
$\Delta\langle \text{KE}_\perp \rangle$	Average change in perpendicular kinetic energy
$E_+(t)$	Co-rotating microwave electric field
$\lvert E_0 \rvert$	Co-rotating microwave electric field amplitude
B^A	PSR experiment magnetic field setting A
B^B	PSR experiment magnetic field setting B
f_{mn}^X	Target frequency resonant with $\lvert m\rangle \rightarrow \lvert n\rangle$ transition at magnetic field X
$\lvert E(f_{mn}^X) \rvert$	Co-rotating microwave electric field amplitude at f_{mn}^X

Table 0.2: List of symbols.

Chapter 1

Introduction

For every particle there is a corresponding antiparticle with the same mass and lifetime but with an opposite charge. For the electron, there is a positively charged anti-electron or positron (e^+) and for the proton there is a negatively charged antiproton ($\bar{p}$). A positron and an antiproton can combine to form an antihydrogen atom ($\bar{H}$); the simplest pure anti-atomic system. Antihydrogen's matter counterpart, hydrogen, has played a key role in the development of quantum theory, from Bohr orbitals to the Dirac equation. Throughout this development, hydrogen spectroscopy has been invaluable for testing and motivating theory and today the hydrogen spectrum is known to high levels of precision [1, 2]. The antihydrogen atom is therefore a natural candidate to test a fundamental symmetry between matter and antimatter known as CPT-symmetry. According to the CPT theorem, any local quantum field theory with Lorentz invariance, such as the Standard Model, must be symmetric under the combined operations of charge conjugation (C), parity inversion (P), and time reversal (T) [3]. As a consequence, the spectrum of antihydrogen should be identical to that of hydrogen. In recent years experiments have made significant progress towards antihydrogen spectroscopy including: production of antihydrogen at low energies (2002) [4], magnetic trapping of antihydrogen atoms (2010) [5], and observation of resonant hyperfine transitions in antihydrogen's ground state (2012) [6].

If spectroscopy of antihydrogen can reach the precision levels achieved on hydrogen CPT-symmetry can be stringently tested.

This thesis focuses on efforts of the ALPHA (Antihydrogen Laser PHysics Apparatus) collaboration[1], and in particular the author's contributions to this work, to magnetically confine and perform the first ever spectroscopic experiment on antihydrogen. The ALPHA apparatus is located at the Antiproton Decelerator (AD) facility at CERN, just outside Geneva, Switzerland. At the time of writing, the ALPHA collaboration consists of 40 members, including the author, from 15 institutions. This thesis will place particular emphasis on the first spectroscopic measurement of antihydrogen and the non-neutral-plasma-based techniques developed to make such measurements possible.

1.1 Background and Motivation

1.1.1 CPT symmetry

Initially it was thought the laws of physics were unchanged under all three operations: C, P, and T, individually. In 1957 this was shown not to be the case by an experiment measuring the helicity (direction of a particle's spin with respect to its momentum) of neutrinos and anti-neutrinos produced by beta-decay [7]. It was found that all observed neutrinos had a left-handed helicity and all anti-neutrinos had a right-handed helicity, violating both C and P symmetries. While individually violated, the combined operation, CP, remained conserved and for a time was believed to be a true fundamental symmetry along with T-symmetry. Seven years later, however, a violation of CP symmetry was found in neutral kaons [8]. Two states of neutral kaons exist: K-short (with a lifetime of roughly 9×10^{-11} s) and K-long (with a lifetime of roughly 5×10^{-8} s). K-short has an eigenvalue of the CP operation of +1 and K-long

---

[1] `http://alpha.web.cern.ch/`

an eigenvalue of -1. To maintain CP symmetry, these particles must decay to a state with the unchanged CP eigenvalues. It was found that while K-short only decays into two pions (a CP = +1 state) and K-long usually decays to three pions (CP = -1), the latter occasionally will decay to two pions, violating CP symmetry. For many years, no violation of CP symmetry was observed outside kaon systems, leaving the possibility that CP violation was confined to these systems. In 2001, however, the BaBar and Belle experiments observed CP violation in the decay of B mesons [9, 10]. Finally, direct violation of T symmetry was only just very recently claimed to be observed (2012), again in B mesons, by the BaBar experiment [11]. Previously, indirect T-violation had been implied by CP violation under the assumption that the combined CPT symmetry holds.

With the observation of CP violation, only the combination of all three operations, CPT, remains as an apparent exact symmetry of nature. To date, CPT symmetry has held up against every experimental test performed. In terms of relative precision, the most stringent CPT symmetry test so far comes from the kaon particle-antiparticle mass difference; known to be less than 1 part in 10^{18} [12]. Other comparisons have been made on properties of electrons/positrons (mass [13], charge [14], and gyromagnetic ratio [15]), similarly for protons/antiprotons [16], and many other systems (see Ref. [17]). The hydrogen/antihydrogen system is particularly attractive for a CPT test because of the high precisions reached in hydrogen spectroscopy. The most attractive atomic transitions for study are the 1S - 2S transition, where the transition frequency is known to 4.2 parts in 10^{15} [1], and the ground state hyperfine transition, known to 1.4 parts in 10^{12} [2].

CPT symmetry is a key component of the standard model of particle physics or of any local Lorentz invariant quantum field theory. In such a theory, a violation of CPT symmetry would also imply that Lorentz symmetry is broken and the discovery of such a process would necessitate a major overhaul of our current understanding of physics. Because Lorentz and CPT symmetries are so deeply ingrained in the structure of physical theories, it is difficult to find a theoretical mechanism for violation of these symmetries that remains compatible with experimental constraints. Such mechanisms are possible, and have been investigated thoroughly, in a class of field theories known as Standard-Model Extensions [18]. The framework developed in this area has been built upon to place limits on CPT and Lorentz violation in various sectors including the hydrogen/antihydrogen system [19].

1.1.2 Gravity and Antimatter

Independent of quantum theory, Einstein developed the classical theory of general relativity, which does not specifically include the concept of antimatter. In general relativity, antimatter is just another form of energy with a corresponding weight. According to the weak equivalence principle in general relativity, the trajectory of a mass in a gravitational field is independent of its composition and structure. Antimatter particles should therefore experience the same gravitational acceleration as their matter counterparts [20]. Complicating this assertion is the incompatibility of standard quantum theory, which implies the existence of antimatter, with general relativity. While CPT symmetry implies that antimatter-antimatter gravitational interactions (e.g. an anti-apple and an anti-earth) should be identical to matter-matter interactions (e.g. an apple and earth), it says nothing about antimatter-matter interactions (e.g. an anti-apple and earth). Perhaps surprisingly, since antimatter has been produced in the lab since the 1930s, there has been no direct observation of the effects of terrestrial gravity on antimatter. While positron and antiproton experiments are relatively mature, the electromagnetic force in these charged particle systems completely overwhelms the gravitational force and even extremely small electric fields will affect the dynamics of charged antiparticles. Antihydrogen, on the other hand, is electrically neutral and relatively insensitive to such effects, making it an exciting candidate to test the weak equivalence principle.

1.2 History of Antimatter

The existence of antimatter counterparts to every matter particle is a consequence of the combination of quantum mechanics and special relativity. In 1928 British physicist Paul Dirac was the first to succeed in developing a theory that fully accounted for special relativity in quantum mechanics [21]. The now famous Dirac equation was very successful in that it accounted for the fine details of the hydrogen spectrum and provided a theoretical explanation for Pauli's theory of spin, which was still a mystery at the time. Unlike Pauli's spin theory, which resulted in two solutions to the Schrödinger equation, the Dirac equation had four solutions: two corresponding to the expected spin up and spin down solutions and two additional solutions with negative energies. While puzzling at the time, the success of the Dirac equation could not be ignored and the physical meaning of the negative energy states became a fiercely debated subject.

In an attempt to explain this problem, Dirac hypothesized that the vacuum was filled with an infinite "sea" of negative energy electrons. Excitation of an electron out of the "sea" leaves a "hole" with positive energy and a positive charge. At first, Dirac proposed that the particles described by these "holes" were protons but it was soon pointed out that the "hole" must have the same mass as an electron. This lead Dirac to conclude [22],

> "A hole, if there were one, would be a new kind of particle, unknown to experimental physics, having the same mass and opposite charge to an electron. We may call such a particle an anti-electron. ... Presumably the pro-

> tons will have their own negative-energy states, all of which normally are occupied, an unoccupied one appearing as an antiproton."

Anti-electrons, or positrons as they are commonly known, did not remain unknown to experimental physics for long. In 1932 Carl Anderson used a cloud chamber to detect the products of high-energy cosmic rays hitting a piece of lead. Electron-positron pairs were produced from the collision of cosmic rays with the lead [23, 24]. The two particles were observed to curve equally in opposite directions in the presence of a uniform horizontal magnetic field. This implied that the particles had the same momentum but opposite charge.

Twenty three years later, the antiproton was discovered by Emilio Segre and Owen Chamberlain at the newly built Bevatron accelerator [25]. In that experiment, high energy (6.3 GeV) protons were directed onto a copper target producing proton-antiproton pairs. They measured the mass of all the negatively charged particles produced and found one with the mass of a proton among the products.

Since positrons and antiprotons can be produced, it should also be possible to make the simplest form of anti-atom: antihydrogen. This was first accomplished in 1995 at the Low Energy Antiproton Ring (LEAR) at CERN [26] and later at the Antiproton Accumulator facility at Fermilab in 1998 [27]. These experiments produced antihydrogen by colliding antiprotons with nuclei in a gas-jet target, occasionally resulting in the production of an electron-positron pair. In a subset of these cases the positron and antiproton would bind to produce an antihydrogen atom. The PS210 experiment at CERN observed 9 antihydrogen atoms in this manner and the E862 experiment at Fermilab observed 99.

These anti-atoms, however, were produced at relativistic speeds and only existed on the order of 100 nanoseconds before encountering matter and annihilating, making them less than ideal for study. At the same time, other experiments at LEAR were developing techniques to trap, cool, and store antiprotons for long periods of time [28–31]. These experiments successfully used cylindrical Penning traps for this purpose. By mixing trapped clouds of positrons and antiprotons, the hope was that low energy antihydrogen could be produced for study. This was accomplished in 2002 by the ATHENA [4] and ATRAP [32] collaborations at the Antiproton Decelerator (AD) facility at CERN. While the lifetime (before annihilation on the trap walls) was only on the order of hundreds of microseconds, this was significantly longer than the nanosecond timescales of antihydrogen produced in flight. The longer lifetime and high production rates allowed studies of antihydrogen formation temperature and of antiproton cooling dynamics during antihydrogen formation [33–35].

1.3 Antihydrogen Experiments

With the success in producing cold antihydrogen, the ATRAP and ALPHA (formed in part by former ATHENA members) collaborations began focusing their efforts on the magnetic confinement of antihydrogen atoms. Ioffe-Pritchard type magnetic traps [36] were superposed with a core Penning trap in both experiments to attempt to magnetically confine the antihydrogen atoms. One open question at the outset of these experiments was whether plasmas could be stably confined in the presence of the magnetic trap fields. Charged particle confinement [37] and antihydrogen formation was soon demonstrated by ALPHA, using an octupolar magnetic field [38], and by ATRAP using a quadrupole field [39, 40]. Manipulation and diagnostics of charged antiparticle plasmas proved to be extremely useful in moving towards trappable antihydrogen. ALPHA studied antiproton diagnostics based on octupole-induced ballistic loss [41]; compression of antiprotons [42]; and imaging of antiprotons, positrons, and electrons with a microchannel plate/phosphor detector [43]. Similarly, ATRAP investigated nondestructive diagnostics of positron and antiproton plasmas [44] and antiproton stacking [45].

ATRAP and ALPHA are no longer the only antihydrogen experiments operating at CERN (or anywhere else for that matter). The ASACUSA (Atomic Spectroscopy And Collisions Using Slow Antiprotons) collaboration has been working towards producing a polarized antihydrogen beam for hyperfine spectroscopy. Recently they demonstrated antihydrogen production in a magnetic cusp trap [46], which also has the potential to trap antihydrogen. A new experiment, AEgIS (Antihydrogen Experiment: Gravity, Interferometry, Spectroscopy), is currently in the final stages of construction at the AD. Their primary goal is a direct measurement of the gravitational acceleration on antihydrogen by observing the free fall of an antihydrogen beam [47]. A second antihydrogen gravity experiment, GBAR (Gravitational Behaviour of Antihydrogen at Rest), has been proposed and is hoping to be installed at CERN in 2014. Their proposed technique is distinguished from that of AEgIS by the usage of sympathetic cooling of $\bar{\mathrm{H}}^+$ ions down to 20 μK [48]. To accommodate the increasing demand for antiprotons at CERN, a small circular accelerator will be constructed within the AD hall. The ring, known as ELENA (Extra Low ENergy Antiprotons), will further decelerate antiprotons from the AD before sending them to individual experiments [49]. The reduced energy antiproton bunches are expected to result in a factor of 100 more antiprotons captured by experiments at the AD.

1.4 Thesis Outline

This thesis is effectively split into two parts. The first part (Chapters 2 - 5) focuses on the trapping of antihydrogen. The primary difficulty in trapping antihydrogen atoms is producing them with kinetic energies low enough to be trapped by the relatively shallow magnetic trap. Fourteen orders of magnitude separate the energy of antiprotons when they are created (3.7 GeV) and the trap depth for antihydrogen (∼50 μeV). Reducing the energy of the antiprotons and positrons that are mixed to form antihydrogen is a common theme throughout the first part of this thesis. Chapter 2 outlines the important components and the basic physics of the ALPHA apparatus. This chapter will discuss the apparatus used to trap, manipulate, and measure antimatter particles. The clouds of positrons and antiprotons (as well as electrons) that are trapped and mixed to form antihydrogen are typically dense enough that they form non-neutral plasmas. The physics of these plasmas in a Penning trap is discussed in Chapter 3. While non-neutral plasmas can introduce additional experimental challenges, there are several important techniques that take advantage of their collective nature. Chapter 4 discusses the key experimental techniques that are used by ALPHA to prepare the antiproton and positron clouds to form trappable antihydrogen. Finally, in Chapter 5, all of this is brought together to demonstrate the first ever trapping of antihydrogen.

With the ability to trap antihydrogen, the second part of this thesis shifts its focus to inducing resonant positron spin flip transitions in trapped antihydrogen atoms. The frequencies of these transitions depend strongly on the strength of the magnetic field at the location of the antihydrogen atom. Chapters 6 and 7 present a method by which the static magnetic field, as well as the microwave electric field, can be measured *in situ* using electron plasmas. Using these methods, Chapter 8 describes the excitation of positron spin flip transitions in antihydrogen. Finally, Chapter 9 concludes this thesis with an outlook towards the future of ALPHA and antihydrogen research.

1.5 Author Contributions

The size of the ALPHA collaboration and the scope of the experiment makes it impossible to completely separate my work from that of the rest of the collaboration.

In writing this thesis I have attempted to focus on the areas that I have contributed the most. ALPHA is small enough that graduate students such as myself are involved in all aspects of the experimental program as a necessity. I spent the majority of the 2009, 2010, and 2011 experimental runs (May - November) working on the ALPHA experiment at CERN. During the 2011 run I spent time acting as the ‘run coordinator’ who is responsible for managing the daily activities of the experiment. In addition, I spent a portion of the spring and fall of 2012 at CERN participating in the construction of and performing measurements with a new ALPHA Penning trap. The work presented in this thesis builds upon the progress of antihydrogen experiments described in Sec. 1.3. This includes significant results such as:

1. Evaporative cooling of charged plasmas (Sec. 4.4, [50]).
2. Autoresonant excitation of antiproton plasmas (Sec. 5.1.3, [51]).
3. Trapping of antihydrogen (Chapter 5, [5]).
4. Trapping of antihydrogen for 1000 s (Sec. 5.2.5, [52]).
5. Resonant induction of positron spin flip transitions in antihydrogen (Chapter 8, [6]).

For all of the listed publications (including the above major results) I was involved in the data taking, analysis, and editing process. As part of a smaller group within ALPHA, I was heavily involved in the setup and execution of the experiment that induced resonant positron spin flip transitions in antihydrogen. In addition, I personally led the development of the plasma mode measurements (Chapter 6) and the implementation of the electron cyclotron resonance diagnostics (Chapter 7). I was the lead author of a manuscript based on this work that has been accepted for publication [53]. The work presented in Chapters 6 and 7 has benefited greatly from the help and guidance of Prof. Walter Hardy, Prof. Michael Hayden, and my supervisors Prof. Makoto Fujiwara and Prof. Robert Thompson.

Chapter 2

Apparatus

Antihydrogen experiments must have the ability to produce, trap, manipulate, and measure the characteristics of clouds of charged particles (positrons and antiprotons) as well as neutral antihydrogen atoms. This requires an apparatus that brings together methods developed in a number of fields including particle physics, plasma physics, and atomic experiments. This chapter will describe the components of the ALPHA apparatus important for producing, trapping, and studying antihydrogen. A schematic overview of the ALPHA apparatus is shown in Fig. 2.1.

2.1 Overview

The ALPHA apparatus was designed as an antihydrogen production and trapping device. At its core is a cylindrical Penning trap superposed with a magnetic minimum neutral atom trap. The antiprotons and positrons are confined, manipulated, and mixed together by the Penning trap (Sec. 2.3). When mixed, positron and antiproton clouds will form neutral antihydrogen that is unconfined by the Penning trap. Instead, antihydrogen atoms (in the proper spin states and of sufficiently low kinetic energy) are trapped by a three-dimensional magnetic minimum generated by superconducting magnets (Sec. 2.4). Because antimatter readily annihilates upon contact with matter, the inner trap system is under ultra-high vacuum (Sec. 2.5). The superconducting

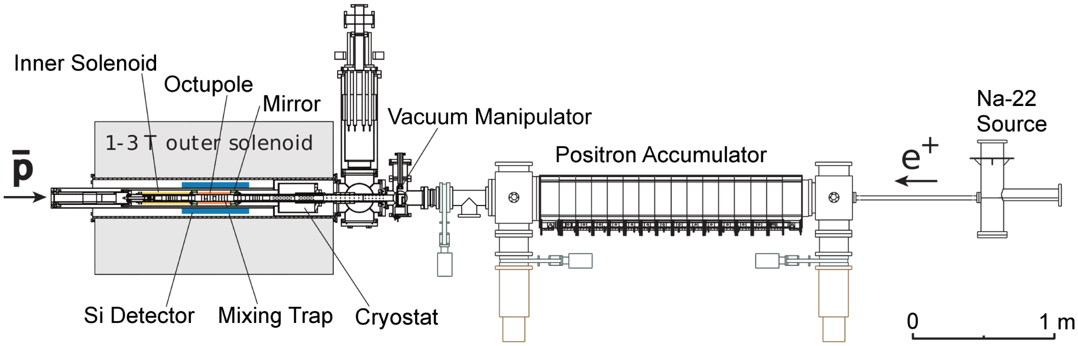

Figure 2.1: A schematic of the ALPHA apparatus. Antihydrogen formation and trapping occur in the mixing trap region. The outer solenoid is operated at 1 T for all experiments described in this thesis. Antiprotons ($\bar{p}$) are delivered from the AD to the left of the schematic. Positrons are generated by the Sodium-22 source and accumulated in the Positron Accumulator before being transferred to the main Penning trap.

magnets and the Penning trap electrodes are immersed in a liquid helium cryostat that serves several important functions: (1) The magnets are kept superconducting; (2) The cooled electrode surfaces act as a cryopump, which improves the vacuum; (3) The radiative temperature of the surfaces that surround the trapped antiprotons and positrons is reduced. Obtaining cold antiprotons and positrons will be a common theme throughout this thesis as it is one of the biggest challenges that must be overcome to trap antihydrogen.

The ALPHA experiment is provided with antiprotons by the Antiproton Decelerator (AD) facility at CERN. Unlike the other accelerators at CERN, the AD is designed to generate beams of particles at as low an energy as possible. Antiprotons are produced by the collision of high energy protons with an iridium target [54]. The antiprotons are then collected, transferred to the AD ring, decelerated, and injected in bunches into the ALPHA Penning trap (Sec. 2.2.1). At the time of writing, the AD is the only source of low-energy antiprotons in the world and home to all of the currently active antihydrogen experiments. Positrons are easy to obtain by comparison. A Surko-type positron accumulator [55] collects positrons that are emitted when radioactive sodium-22 decays to neon-22 via beta decay (Sec. 2.2.2). Positron accumulators of this type are relatively compact and are widely used in antimatter and non-neutral plasma research.

Diagnostics of the antiproton, positron, and electron clouds are critical to the success of ALPHA. The number of particles in a cloud is measured by releasing the particles onto a Faraday Cup that measures the deposited charge (Sec. 2.6.1). The cloud radial density profile is measured by instead releasing the particles onto a micro-channel plate (a spatially resolving array of electron multipliers) and phosphor screen detector (Sec. 2.6.2). While working with antimatter often presents additional challenges to an experiment, its nature can also be advantageous. Matter-Antimatter annihilations release energy in the form of charged particles and photons which can be detected and used as diagnostics. Cesium-Iodide detectors, scintillators, and a silicon annihilation reconstruction detector are all used to study the properties of positron and antiproton clouds, and of trapped antihydrogen atoms, based on the detection of their annihilations (Sec. 2.6.3, Sec. 2.6.4, and Sec. 2.6.5, respectively).

The apparatus described in the following sections was used for the vast majority of the measurements presented in this thesis. At the end of 2011 this apparatus, known as ALPHA-1, was disassembled to begin construction of the next generation of the ALPHA experiment (ALPHA-2), which has been designed to carry out spectroscopic measurements on trapped antihydrogen. Two key features of the ALPHA-2 apparatus are: (1) Laser access for spectroscopy of antihydrogen and (2) a separate Penning trap dedicated to antiproton catching and accumulation. This Penning trap, known as the ALPHA-2 catching trap, was used to provide a complimentary data set for the experiments presented in Chapter 7. The relevant details of the ALPHA-2 Catching trap are described at the end of this chapter (Sec. 2.10) and a discussion of the full

ALPHA-2 apparatus will be made in Chapter 9. Unless otherwise noted, all discussion in this chapter, and throughout the thesis, refers to the ALPHA-1 apparatus.

2.2 Particle Sources

2.2.1 Antiproton Decelerator

Antiprotons are produced through a pair production process by colliding a high energy beam of protons with a metal target. At CERN, the Proton Synchrotron facility accelerates a beam of protons up to a momentum of 26 GeV/c, which is then directed onto an iridium target. Among the products of the collisions are antiprotons, which are filtered based on their mass-to-charge ratio by a magnetic horn and directed into the antiproton decelerator (AD) with a momentum of 3.57 GeV/c [56].

The AD slows the antiproton bunches from GeV to MeV energies with a series of resonant radio-frequency cavities. An oscillating electric field is applied in these cavities opposing the bunch motion and slowing the particles. Deceleration of the beam causes the beam spread in size and momentum to increase due to the conservation of phase-space density [57]. This spread is counteracted by interspersing beam cooling phases with the deceleration cycles.

At high beam energies (3.57 GeV and 2 GeV) a technique known as stochastic cooling [58] is applied. On each circuit around the AD ring, the particles pass a pickup that measures the distance of a particle from the ideal central orbit. Based on this deflection, a correction signal is applied downstream to correct the particle orbit. The beam is not made up of just one particle, however, and a correction applied for one particle may perturb another. Fortunately, with the correct choice of correction pulse amplitude, the net effect is a reduction in the overall beam size and energy spread. At lower beam energies, where stochastic cooling is less efficient, electron cooling [59, 60] is used. A cold electron beam is injected into the AD to overlap with the antiproton bunch over a short section of the AD ring. Through Coulomb collisions, the hotter antiprotons will transfer energy to the electrons, reducing the antiproton beam's energy spread. The electrons are then removed to obtain a cooled pure antiproton beam.

After the final electron cooling stage, 3×10^7 antiprotons are extracted to an experiment in a 200 ns long bunch with a kinetic energy of 5.3 MeV. A fraction of these antiprotons are caught and further cooled in the ALPHA Penning trap using methods described in Chapter 4.

2.2.2 Positron Accumulator

Compared to antiprotons, production of positrons for ALPHA is a much smaller task. Positrons are produced by the beta-plus decay of radioactive sodium-22 in the following reaction:

$$ {}^{22}_{11}\mathrm{Na} \;\rightarrow\; {}^{22}_{10}\mathrm{Ne} + \mathrm{e}^{+} + \nu_{\mathrm{e}}. \tag{2.1}$$

Sodium-22 has a half-life of roughly 2.6 years [61], allowing for relatively high activity sources while not requiring frequent replacement.

Emitted positrons are collected in a device known as a Surko-type positron accumulator [55]. Beta-decay positrons are emitted with kinetic energies of hundreds of keV and must be slowed before they can be trapped. To accomplish this, Surko-type accumulators employ a thin layer of solid neon that the positrons pass through. As they transit through the neon, the positrons lose energy and a small fraction of the incident positrons (~ 0.4 %) will escape the neon and have energies around 50 eV [62].

The slowed positrons are then guided by a magnetic field to a cylindrical Penning trap with a 0.15 T field (see Fig. 2.2). Further cooling of the positrons is provided by nitrogen buffer gas in the Penning trap region. Kinetic energy is transferred from the positrons to the nitrogen by collisions that excite the molecules. Approximately 20%

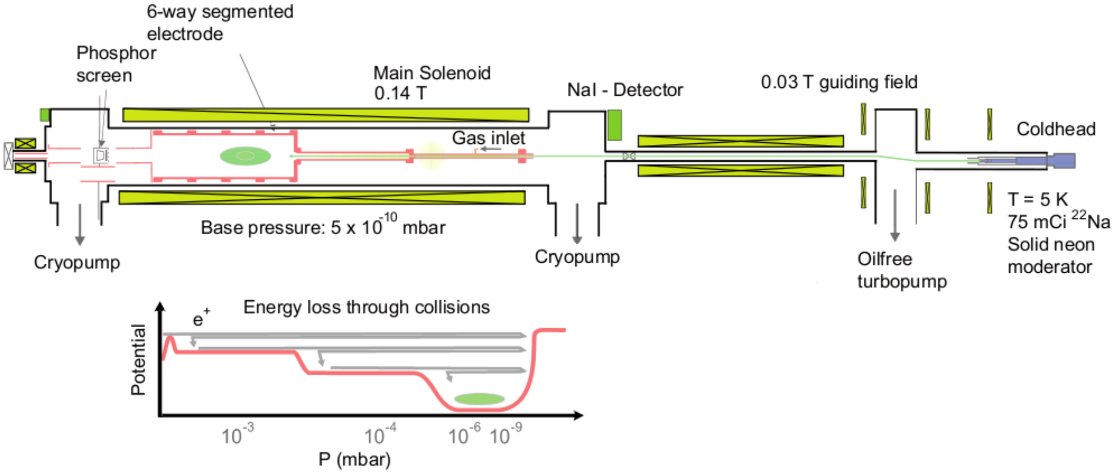

Figure 2.2: Schematic of the ALPHA positron accumulator. The positrons follow the green path from the sodium-22 source on the left to the Penning trap where they are collected. The lower plot shows the on-axis electric potential against the buffer gas pressure in the trap. (Adapted with permission from [63])

of the positrons lose sufficient energy to be captured and cool further in the trap. The accumulator Penning trap electrodes increase in radius along the trap axis away from the positron source, creating a natural pressure gradient along the trap. The on-axis potential depth also increases as a function of position and after sufficient cooling the positrons will be confined in the large radius portion of the trap. The positrons accumulate in this region of the trap for 200 s, while the rotating wall technique (see Sec. 4.2) is applied to control the positron cloud radius.

A mechanical valve separates the positron accumulator from the main ALPHA Penning trap (Sec. 2.3.2) vacuum. To avoid contaminating the main trap vacuum, the nitrogen gas in the accummulator is removed by a pair of vacuum pumps before the valve is opened and the positrons are transferred to the main trap. Approximately 2.5×10^7 positrons are recaptured in the main trap after a typical accumulation cycle.

2.2.3 Electron Gun

Electrons are also used in ALPHA, primarily for antiproton cooling after an antiproton bunch from the AD is captured in the ALPHA trap (see Sec. 4.1). In addition, electron plasmas were heavily used as magnetic field and microwave electric field diagnostics for resonant experiments with antihydrogen's hyperfine levels (see Chapters 6, 7 and 8). The 'electron gun' is a barium-oxide filament that, when heated by an electric current, emits electrons via thermionic emission. The electrons are collimated and accelerated by an electrode in front of the filament and steered into the Penning trap by magnetic fields.

2.3 Penning Trap

2.3.1 Theory

Penning traps are a class of traps that combine electric fields with a uniform magnetic field to confine charged particles in three dimensions. These traps have been used successfully for many years to make precision measurements of particles and ions [64–67] and in the study of non-neutral plasmas [68, 69]. The classic Penning trap is formed by a solenoidal magnetic field and an electric quadrupole potential:

$$\begin{aligned} \vec{B} &= B_0\hat{z}, && (2.2) \\ \phi(r,z) &= \frac{V_0}{2d^2}\left(z^2 - \frac{r^2}{2}\right), && (2.3) \end{aligned}$$

where d is a factor set by the trap geometry. An ideal electric quadrupole potential can be produced by voltages applied to hyperbolic electrodes that lie along equipotential surfaces of a quadrupole field. The equation of motion for a particle of charge q and mass m in these fields is given by the Lorentz force

$$m\frac{d^2\vec{r}}{dt^2} = q(-\nabla\phi + \frac{d\vec{r}}{dt} \times \vec{B}), \tag{2.4}$$

where $\vec{r} = (x, y, z)$. Breaking this equation into its Cartesian components gives

$$\begin{aligned} \frac{d^2x}{dt^2} &= \frac{qV_0}{2md^2}x - \frac{qB_0}{m}\frac{dy}{dt}, && (2.5)\\ \frac{d^2y}{dt^2} &= \frac{qV_0}{2md^2}y - \frac{qB_0}{m}\frac{dx}{dt}, && (2.6)\\ \frac{d^2z}{dt^2} &= -\frac{qV_0}{md^2}z. && (2.7) \end{aligned}$$

The $\hat{z}$ motion in an ideal Penning trap is decoupled from the magnetic field and undergoes simple harmonic motion with a frequency $\omega_z = qV_0/(md^2)$. The $\hat{x}$ and $\hat{y}$ motions can be solved by noting that $\omega_c = qB_0/m$ is the cyclotron frequency and by making the substitution $u = x + iy$ to obtain

$$\frac{d^2u}{dt^2} + i\omega_c\frac{du}{dt} - \frac{1}{2}\omega_z^2 u = 0. \tag{2.8}$$

This equation has a solution of the form $u = \exp(-i\omega_\pm t)$ with

$$\omega_\pm = \frac{1}{2}\left(\omega_c \pm \sqrt{\omega_c^2 - 2\omega_z^2}\right). \tag{2.9}$$

For a particle to undergo confined oscillatory motion, $\omega_\pm$ must be real and therefore would require $\omega_c^2 > 2\omega_z^2$. The low frequency solution, ω_-, is known as the magnetron frequency, which is a slow drift motion in a large circular orbit. The magnetron motion is also known as the '$\vec{E} \times \vec{B}$' motion as its drift velocity is given by $\vec{v} = \vec{E} \times \vec{B}/|\vec{B}|^2$. The high frequency solution is known as the modified cyclotron frequency and can be written as $\omega_c^{'} \equiv \omega_+ = \omega_c - \omega_m$, where $\omega_m \equiv \omega_-$. The overall motion of a particle in a Penning trap is sketched in Fig. 2.3. Typically, these three motions have a hierarchy $\omega_c \gg \omega_z \gg \omega_m$. Typical oscillation frequencies in the ALPHA Penning trap are shown in Table 2.1. A comprehensive treatment of particle motion in a Penning trap can be found in [70].

Hyperbolic electrodes allow for creation of nearly ideal quadrupole electric fields but severely restrict access to the trap for particle loading and measurement. Alternatively, a stack of cylindrical electrodes with open ends can be employed allowing

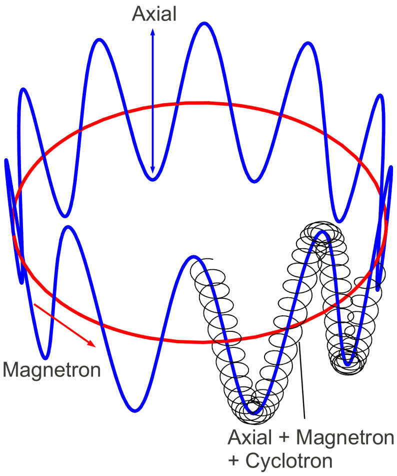

Figure 2.3: A sketch of particle motion in a Penning trap. For illustration purposes a $\omega_c : \omega_z : \omega_m$ ratio of 300:10:1 has been used.

Particle	ω_c	ω_z	ω_m
Electron/Positron	176 GHz	100 MHz	31 kHz
Antiproton	94 MHz	3.1 MHz	31 kHz

Table 2.1: Typical oscillation frequencies in the ALPHA Penning trap with a 1 T magnetic field.

for easier loading and measurement of particles, and increased flexibility in manipulating the particles [71]. While a cylindrical Penning trap, sometimes referred to as a Penning-Malmberg trap, does not produce a pure quadratic potential, the particles can still be confined. The trapped particles will undergo the same periodic motions as in a hyperbolic trap, though not at precisely the same frequencies. Compensation electrodes can be added to cylindrical Penning traps to produce sufficiently quadratic potentials for precise measurements of single particles [70]. The ALPHA Penning trap, however, is not designed to make precision measurements on single particles but rather to confine and manipulate clouds of $> 10^4$ particles. At high densities these clouds can be considered plasmas that exhibit a range of collective dynamics. These dynamics are discussed in Chapter 3.

2.3.2 ALPHA Penning Trap

ALPHA employs a cylindrical Penning trap made up of 35 cylindrical aluminium electrodes surrounded by a large superconducting solenoid, which produces a uniform 1 T field. The electrodes are gold plated and separated by small ruby spheres and ceramic insulators. The Penning trap is divided into three regions with three distinct functions (Fig. 2.4). Starting from the upstream end (with respect to incoming antiprotons from the AD) is the catching trap, followed by the mixing trap and the positron trap.

The catching trap is designed to catch the high energy antiproton bunches injected by the AD using two specially designed high voltage electrodes. These two electrodes are separated from their neighbours by ceramic spacers to avoid arcing. Multiple antiproton bunches can be collected in the catching trap region where they are also cooled (see Sec. 4.1) and compressed (see Sec. 4.2). The catching trap region is surrounded by an additional superconducting solenoid (the ‘inner’ solenoid) that can be energized to bring the local field up to 3 T for enhanced catching and cooling of

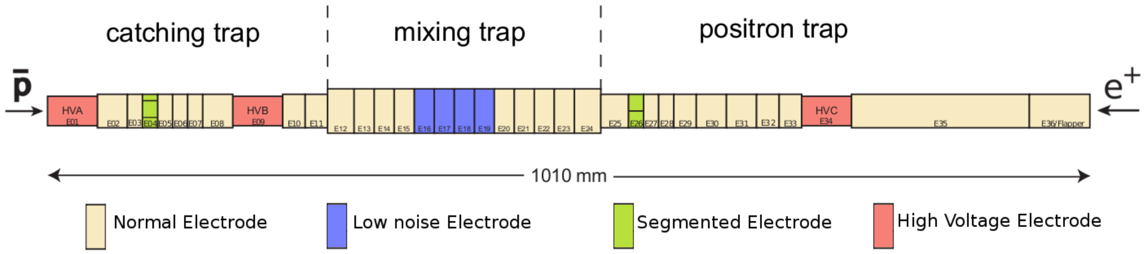

Figure 2.4: Schematic of the ALPHA Penning trap electrodes. Not pictured here is a superconducting solenoid that surrounds the electrodes, producing a uniform 1 T field along the axis.

antiprotons.

The positron trap on the other end serves a similar purpose for positrons from the positron accumulator (Sec. 2.2.2). Both the catching and positron traps include a special azimuthally segmented electrode that is used in the rotating wall technique [72] to radially compress or expand trapped plasmas (Sec. 4.2).

The core of the ALPHA Penning trap is the central 'mixing' trap region where antiprotons and positrons are mixed to form antihydrogen. These electrodes have a large trap radius and are manufactured to be as thin as possible to maximize the depth of the magnetic trap (see Sec. 2.4). Thin electrodes also minimize the amount of scattering material that antiproton annihilation products encounter before passing through the silicon detector (see Sec. 2.6.5).

The electrodes are connected to vacuum feedthroughs using copper coaxial cable connected to each electrode. These cables are connected to a circuit board that is thermally anchored to the liquid helium bath, effectively anchoring the electrodes themselves. From this point to an external connector, the coaxial cables are made of stainless steel to reduce heating from the outside world. Temperature sensors are connected to several electrodes and read a temperature of approximately 7.5 K during normal operation.

Electrode potentials are controlled by a National Instruments PXI 6733 digital to analog card (DAC). Voltage signals in a ±10 V range are fed to a set of amplifiers that output the voltage applied to the electrodes. Most electrodes are driven by amplifiers that output voltages in a ±140 V range to within 4 mV, while the central mixing trap electrodes are driven by modified low-noise amplifiers with a ±72 V output to within 2 mV. The output of the amplifiers passes through a low pass filter to reduce external noise coupling into the experiment. Voltage and timing information is pre-programmed into the DAC before each experiment.

2.4 Magnetic Trap

The Penning trap is a powerful tool for the trapping, manipulation, and mixing of antiprotons and positrons. Once antihydrogen is formed, however, a magnetic trap for antihydrogen confinement is required.

2.4.1 Theory

An antihydrogen atom has a small magnetic dipole moment, $\vec{\mu}$, due to the angular momentum of the positron and antiproton. In an external magnetic field, $\vec{B}$, the dipole moment interacts with the field with a magnetic potential energy given by

$$U = -\vec{\mu} \cdot \vec{B}. \tag{2.10}$$

Due to the large mass difference between the positron and antiproton, the contribution of the former dominates the dipole moment ($m_{e^+}/m_{\bar{p}} \approx 5.4 \times 10^{-4}$ [17]). The dipole moment is therefore, to a good approximation, given by

$$\vec{\mu} \simeq \vec{\mu_{e^+}} = -g_J \mu_{\mathrm{B}} \frac{\vec{J}}{\hbar}, \tag{2.11}$$

where g_J is the Lande g-factor, μ_{B} is the Bohr magneton and $\vec{J}$ is the positron's total angular momentum. If the antihydrogen atom is in its ground state, the orbital angular momentum is zero and the magnetic dipole moment will be solely due to the positron spin angular momentum. Given the allowed spin angular momenta, $S = \pm\hbar/2$, and that $g_S \simeq 2$, the magnetic dipole moment of ground state antihydrogen can have two states $\mu = \pm\mu_{\mathrm{B}}$ with magnetic potential energies $U = \mp\mu_{\mathrm{B}}B$. The magnetic potential energy of these two states is plotted as a function of B in Fig. 2.5.

Atoms with dipole moments aligned ($\mu = +\mu_{\mathrm{B}}$) with the magnetic field are attracted to regions of high magnetic field (minimizing U) and are known as 'high-field seekers'. Those atoms with anti-aligned dipole moments, on the other hand, are attracted to regions of low magnetic field and are 'low-field seekers'. By constructing a magnetic field with a local minimum in three dimensions, antihydrogen atoms in their 'low-field seeking' ground state can be confined. The depth of such a magnetic trap can be expressed as

$$\Delta U = 0.67\Delta B \quad [\mathrm{K}], \tag{2.12}$$

in units of temperature, where ΔB is the difference between the maximum and minimum magnetic field in Tesla. Magnetic confinement of 'high-field seekers', on the other hand, is not possible because Maxwell's equations do not allow a magnetic field with a maximum in three dimensions [73].

2.4.2 ALPHA Magnetic Trap

In ALPHA, the magnetic minimum trap is created using three superconducting magnets. Two superconducting cylindrical coils, one on either side of the trapping region, create a magnetic field minimum in the axial direction. These coils, referred to as 'mirror coils', operate at a nominal current of 600 A with a maximum of 750 A possible. Confining antihydrogen in the transverse direction is comparatively challenging. A transverse multipole field is constructed to complete the three dimensional magnetic minimum. An ideal multipole magnet of order ℓ produces a transverse magnetic

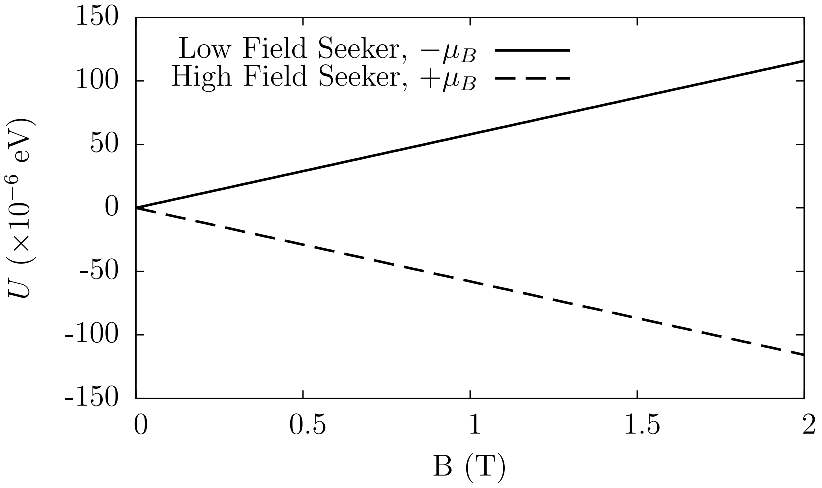

Figure 2.5: Magnetic potential energy of the hyperfine ground states of antihydrogen in the strong magnetic field limit. The dipole moment of the antiproton has been neglected here.

field that scales with radius as

$$B_\perp \propto r^{\ell-1}. \tag{2.13}$$

A quadrupole field ($\ell = 2$) can be generated with four current bars where the current in each bar flows in the opposite direction to its neighbour. Similarly, a sextupole ($\ell = 3$) or an octupole ($\ell = 4$) field can be generated with six or eight current bars, respectively. The transverse magnetic field as a function of radius for these three configurations is plotted in Fig. 2.6. In terms of trap depth, the quadrupole configuration is optimal because the effective depth of the neutral atom trap is determined by the magnetic field at the walls of the Penning trap rather than at the edge of the magnet coil. If ALPHA's inner electrode radius was reduced by 1 mm the effective depth would be reduced by 4%, 9%, and 13% for the quadrupole, sextupole and octupole configurations, respectively. Trap depth is not the only important factor, however. The addition of a multipole field breaks the azimuthal symmetry of the Penning trap magnetic field, reducing the lifetime of trapped plasmas (see Chapter 3). Higher order multipoles perturb the magnetic field near the trap axis less and provide better confinement of charged plasmas [74].

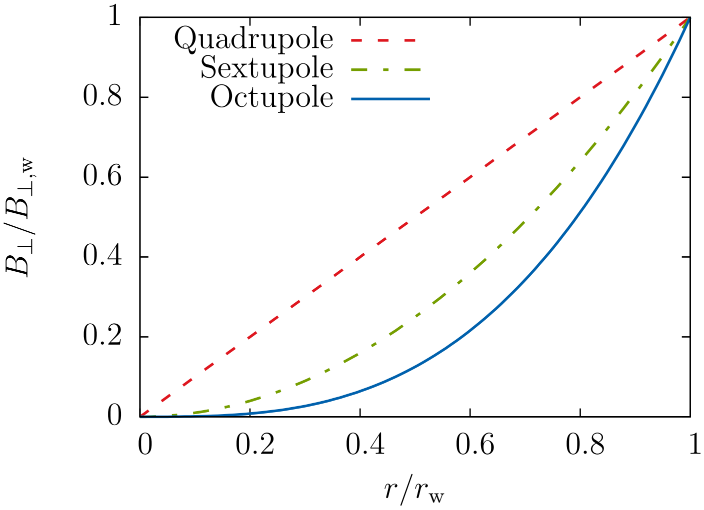

Figure 2.6: The transverse magnetic field strength ($B_\perp$) as a function of radius for quadrupole, sextupole, and octupole configurations. The field and radius have been normalized with their values at the electrode wall.

The ALPHA magnetic trap balances these requirements by creating an octupole field, for improved plasma confinement, with superconducting wire wound directly on the outside of the vacuum chamber to maximize the trap depth [75]. The separation between the electrode inner surface and the magnet winding is further reduced by making the mixing trap electrodes as thin as possible. Typically, a multipole field is produced by so-called 'race-track coils', however the turns of these coils give rise to an undesired axial field component. The ALPHA octupole avoids this by using a serpentine pattern (see Fig. 2.7) with eight windings each azimuthally staggered by 45° with respect to each other. With this pattern, the axial field is nearly completely cancelled out. The octupole was designed to operate at currents up to 1100 A but is typically run at a current of 900 A for antihydrogen trapping.

The mirror coil and octupole magnets are constructed with Niobium-Titanium superconducting wire with a critical temperature of 9 K. The magnets are immersed in the liquid helium bath of the ALPHA cryostat (see Sec. 2.5) at 4.2 K. At the

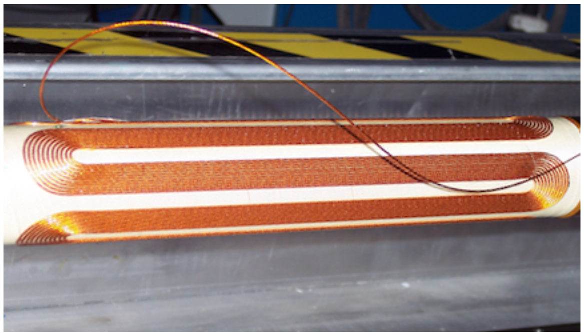

Figure 2.7: A photograph of the first layer of octupole windings (image courtesy of the ALPHA collaboration).

nominal currents used for antihydrogen trapping, the mirror coils produce a maximum longitudinal field of 1.2 T and at the electrode walls the octupole produces a transverse magnetic field of 1.5 T. The trap depth is set by the difference in the magnetic field strength between the trap minimum (B_0) and the the electrode walls (B_{w}). Because the octupole and solenoid fields are orthogonal, the difference in field strength is given by

$$\Delta B = \sqrt{B_{\mathrm{w}}^2 + B_0^2} - B_0. \tag{2.14}$$

With the trap minimum at 1 T (set by the Penning trap solenoidal field) this corresponds to a depth of 0.8 T in field or 0.5 K in temperature units for ground state antihydrogen (see Eq. 2.12).

Great care is taken to protect the ALPHA magnets from a damaging ‘quench’, which occurs when a piece of superconductor suddenly becomes resistive and begins to heat. A chain reaction can occur if even a small portion of the wire heats neighbouring sections of superconductor, bringing them above the critical temperature, which in turn results in more heating. Because of the large currents used in the wires, the heat produced can begin to boil the liquid helium, rapidly producing large volumes of helium gas and potentially posing an explosive threat to the apparatus. The onset of such events is detected by constant monitoring of the voltage drop across the magnets; a non-zero voltage indicating a quench. If a quench is detected, an insulated-gate bipolar transistor (IGBT) quickly switches to direct the current through a resistor network that dissipates the energy safely. The quench protection system also plays a key role in the detection of trapped antihydrogen. As will be discussed in Chapter 5 ALPHA detects trapped antihydrogen by turning off the trap and detecting the annihilation of the previously trapped anti-atoms. The quicker the trap can be switched off, the lower the detector background due to electronic noise and cosmic-rays will be. The quench protection system can be intentionally triggered to remove the current from the magnets with a decay time constant of 9 ms (as measured by shunt resistors in series with the magnets).

2.5 Vacuum and Cryogenics

Stable confinement of plasmas in a Penning trap requires ultra-high vacuum (UHV) conditions to prevent loss of particles due to collisions or recombination with background gas. In the case of antimatter plasmas, UHV pressures are even more important as annihilations with background gas particles will result in additional losses. The ALPHA apparatus features a UHV trap vacuum chamber and an outer vacuum chamber separated by the liquid helium volume of the cryostat (Fig. 2.8).

The trap vacuum surrounds the Penning trap electrodes and all particle trapping and manipulation occurs within this volume. At one end of the electrodes (the left side in Fig. 2.4), the trap vacuum is separated from the higher pressure vacuum of the AD by a 12.5 μm thick stainless steel vacuum window. Vacuum pumps, gauges, and valves are located at the other end of the trap vacuum (towards the right in Fig. 2.4). This portion of the vacuum also includes a moveable vacuum manipulator (Sec. 2.7), which can position a number of different instruments in line with the Penning trap axis.

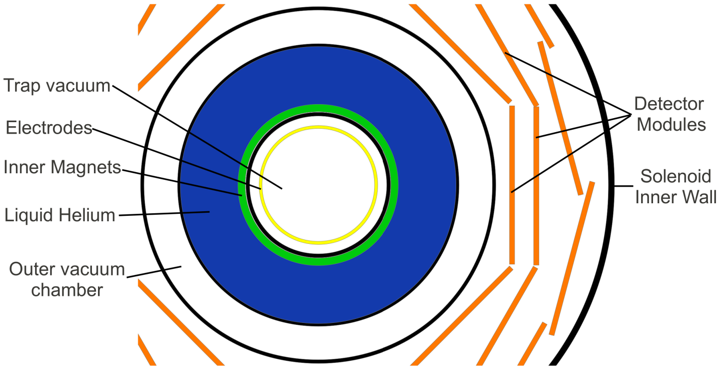

Figure 2.8: A schematic cross-section of the apparatus core showing the two vacuum chambers and the liquid helium volume.

The trap vacuum is partially surrounded by a liquid helium bath, which cools the neutral atom trap magnets and the inner solenoid. Surrounding the liquid helium volume is an outer vacuum chamber, which insulates the cold inner surfaces from the outside world. The liquid helium bath is also in thermal contact with the electrode circuitry and cools the electrodes to roughly 7.5 K. The cold surfaces of the trap vacuum cause background gas molecules that strike the walls to condense or freeze, a process known as cryopumping, further reducing the trap pressure. Vacuum gauges in the room temperature portion of the vacuum typically read 10^{-10} mbar but pressures in the Penning trap are expected to be lower than this. Based on the annihilation rate of antiprotons stored in the Penning trap, the pressure is estimated to be 10^{-13} to 10^{-14} mbar [76].

2.6 Detectors

2.6.1 Faraday Cup

The number of particles in an electron or positron plasma in the Penning trap can be measured by directing the particles onto a device known as a Faraday cup. A

Faraday cup is simply a small piece of conductor that collects the charge of the particles that hit it. If the capacitance of the conductor is known, the number of incident particles can be measured from the voltage induced by the collected charge. In ALPHA, an aluminium foil used as a degrader to slow incoming antiprotons (see Sec. 4.1) doubles as the Faraday cup. The ALPHA Faraday cup detector is sensitive to particle numbers as low as 10^6 electrons/positrons. However, the Faraday cup is not used to measure antiproton numbers. Instead, the charged byproducts of annihilations are detected by external scintillators to infer the number of antiprotons that annihilated (see Sec. 2.6.3). This allows much smaller numbers of antiprotons to be counted than possible with the Faraday cup.

2.6.2 MCP/Phosphor Screen Detector

One of the most important tools in the ALPHA apparatus is a charged particle detector that consists of a microchannel plate (MCP), a phosphor screen, and a CCD camera. This detector is used to measure both the radial density profile of plasmas and their temperature (see Sec. 3.5). The MCP is a plate of semiconducting material with an array of small channels that pass through the plate. When a particle hits the inside of one of these channels secondary electrons are produced and then accelerated by a potential difference applied between the front and back surfaces of the MCP. These electrons can in turn collide with the wall again and produce more electrons, resulting in a cascade that amplifies the original signal. The electrons leaving the MCP channels are directed onto a phosphor screen that produces visible light when excited. The light emitted by the phosphor screen is reflected by a 45° mirror to a CCD camera outside the trap vacuum. A two-dimensional image (integrated over the axial length) of a plasma is obtained by quickly releasing it from the Penning trap onto the MCP/phosphor screen. A schematic of the MCP/phosphor screen/CCD setup is shown in Fig. 2.9.

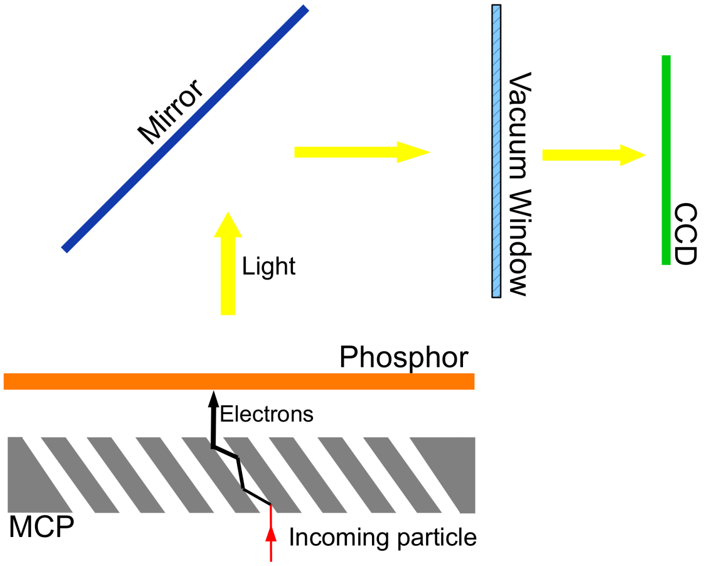

Figure 2.9: A schematic of the MCP/phosphor screen detector.

The active area of the MCP has a diameter of 41.5 mm with 12 μm diameter channels separated by 15 μm in a hexagonal array. Each pixel of the CCD camera covers roughly 30 MCP channels. The MCP/phosphor screen detector is controlled by voltages applied to the front of the MCP, the back of the MCP, and to the phosphor screen. The front voltage accelerates the incoming particles to a desired impact energy and depends on the charge sign of the particle. The back voltage creates a potential difference across the MCP that accelerates the secondary electrons and effectively controls the gain of the detector. The front-back potential difference typically varies from 400 V, for large numbers of particles, to 900 V for fewer particles and is chosen to provide adequate gain without saturating. The potential difference between the phosphor screen and the back of the MCP accelerates and guides the electrons onto the screen.

Figure 2.10 shows example images of electron, positron, and antiproton plasmas taken by the MCP/phosphor screen detector. The radius of the plasmas is determined by fitting the measured intensity distribution with a two-dimensional generalized

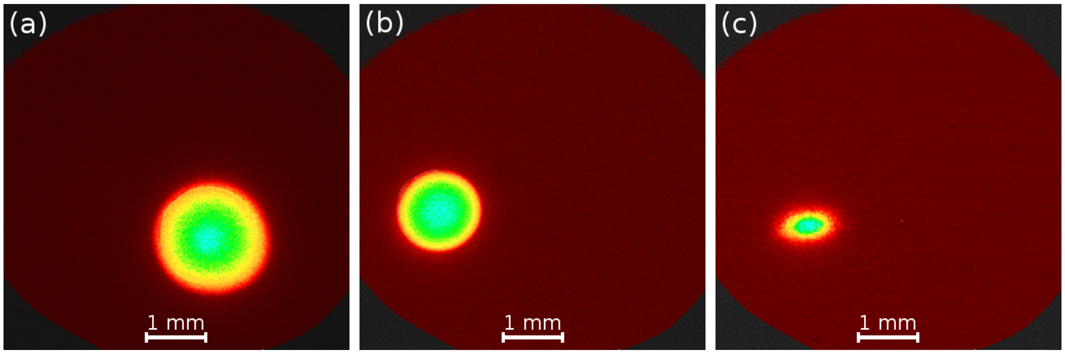

Figure 2.10: False colour images of (a) positron, (b) electron, and (c) antiproton plasmas taken by the MCP/phosphor screen detector. The scale indicates the plasma size in the trap before extraction. Colour indicates relative intensity (red to blue).

Gaussian function, given by

$$I(\vec{r}) = a \exp\left(-\left(\frac{|\vec{r}-\vec{r}_0|}{R}\right)^n\right) \tag{2.15}$$

where R is the plasma radius and a, R, $\vec{r}_0$ and n are fit parameters. While the electron and positron images have a circular shape, the antiproton image appears elliptical. This is thought to be caused by the shape of the Penning trap solenoid fringe field at the detector. At this position, 1.3 m from the trap centre, the magnetic field is only 240 G and while the positrons and electrons will be tightly bound to the field lines, the larger mass antiprotons may not tightly follow the field lines resulting in observed elliptical image. A detailed study of the MCP response to electron, positron, and antiproton plasmas in ALPHA can be found in [43].

2.6.3 Scintillators

Antiprotons will annihilate when brought into contact with protons or neutrons within a matter nucleus. These annihilations result in the release of, on average, three charged pions [77], which can be detected by their passage through scintillators sitting just outside the ALPHA apparatus. Scintillators produce light when ionizing radiation, such as a high-energy charged pion, passes through them. The scintillating paddle is connected to a photo-multiplier tube (PMT) at one end that collects and converts the light into a detectable electrical signal. When this signal is above a certain threshold a ‘count’ is registered. The scintillators also detect 511 keV gamma rays from positron-electron annihilations but the detection efficiency is low.

Twelve 40 cm x 60 cm x 1 cm scintillating paddles are mounted vertically in pairs along the trap length. The scintillators are placed in pairs and operated in time-coincidence mode - only when both paddles exceed the signal threshold is a count registered - to reduce sensitivity to electronic noise. The majority of signal particles that hit the first paddle will hit the second, registering a count in each, while false hits from electronic noise are uncorrelated. The scintillators are placed at three positions along the trap with a pair of scintillators on either side of the apparatus at each position. One of the regular uses of the scintillators is to measure the antiproton number by releasing the antiprotons onto the Faraday cup. The subsequent annihilation products are detected by opposing scintillator pairs placed at the the Faraday cup position.

2.6.4 CsI Detectors

Once in the main Penning trap, the positron plasmas are well characterized using the MCP detector and the Faraday cup. To ensure efficient and reproducible accumulation and transfer of positrons from the positron accumulator, a series of compact Cesium-Iodide (CsI) detectors are placed along the accumulator and transfer section. The CsI crystals operate as scintillating detectors that are sensitive to 511 keV gamma rays and use photodiodes to measure the light produced.

2.6.5 Silicon Detector

Perhaps the most important detector in the ALPHA apparatus is the three-layer silicon tracking detector, which surrounds the antihydrogen formation and trapping region. This detector provides the ability to detect and identify the location of single antiproton annihilations. The low background rate and spatial resolution of this detector were key to the demonstration of both the trapping of antihydrogen (see Secs. 5.1.4 and 5.2.1) and the induction of positron spin flip transitions within antihydrogen (see Sec. 8.3).

The silicon detector consists of a total of 60 silicon modules, each with an active area of 6.1 cm x 23.0 cm = 140.3 cm^2. The detector is divided axially in two halves, which together cover 46 cm along the trap and provide a solid angle coverage of $\sim$ 90% for annihilations at the axial centre. Each module has 256 signal strips that run along the long (23 cm) length of one side of the module and another 256 strips running across the short (6.1 cm) length on the other side of the module. The centres of adjacent strips are separated by 227 μm for strips along the long length of the modules and by 875 μm for strips running along the short length. When a charged pion passes through the active area of a module, charge is deposited on strips on both sides. Readout of the strips allows the hit position to be reconstructed. If the particle registers hits in all three layers of the detector, the helical path of the particle can be reconstructed. With two or more tracks, the annihilation position or vertex can be estimated. Figure 2.11 shows an example of an annihilation vertex reconstruction.

Full readout of the detector strips can be triggered by different conditions, depending on the type of measurement being made. Each full readout of the detector is known as an ‘event’. The most commonly used trigger condition is known as the ‘Si>1’ trigger, which requires at least two hits on the inner layer of the detector. This trigger is designed to accept as many annihilation events as possible, while rejecting the majority of events due to electronic noise. Full events can be read out at a peak rate of 500 Hz. Based on a cross-calibration with the external scintillators, the ‘Si>1’ trigger efficiency is estimated to be $(90 \pm 10)\%$ [79].

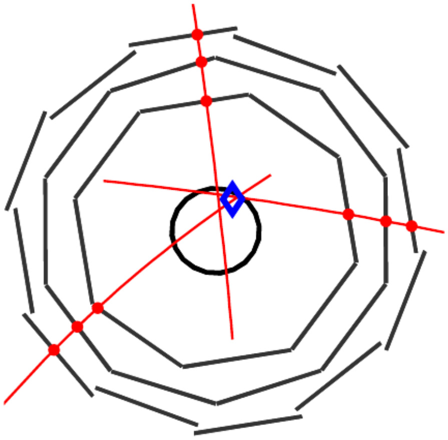

Figure 2.11: A cross-section of a reconstructed antiproton annihilation. The central circle is the electrode surface, which is surrounded by the modules of the silicon detector. The red dots indicate hit positions on the modules and the curved lines are reconstructed particle tracks. The reconstructed vertex position is indicated by the blue diamond. (Adapted with permission from [78])

Annihilation products pass through several layers of scattering material before they reach the detector, affecting the position resolution of the vertex reconstruction. Based on simulated annihilations, the resolution of the vertex reconstruction is 0.56 cm axially, 0.87 cm radially and 21.4° azimuthally (at the electrode radius of 2.23 cm, this corresponds to 0.83 cm). Full details of the detector hardware and vertex reconstruction can be found in references [79] and [80, 81].

2.7 Vacuum Manipulator

While the cylindrical Penning trap geometry gives good access to the trap volume compared to a hyperbolic geometry, there are a multitude of devices that must be positioned in line with the trap axis to function. To solve this technical challenge, the ALPHA apparatus includes a moveable vacuum manipulator, which can position different components in line with the trap axis. Mounted on the vacuum manipulator is a passthrough electrode for positron transfer from the accumulator, the electron

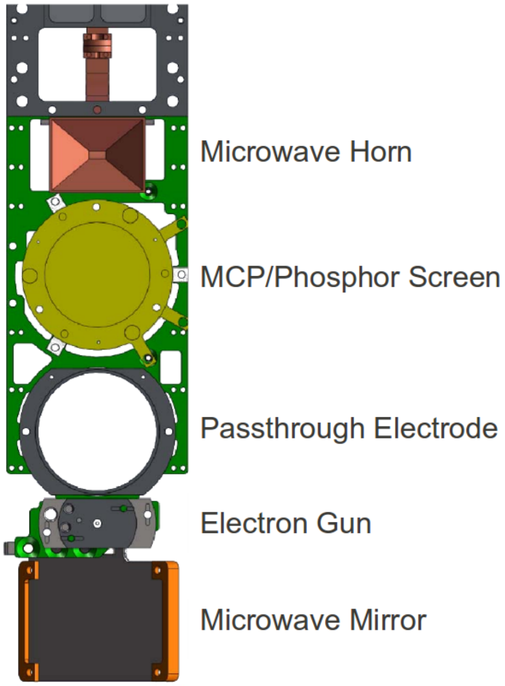

Figure 2.12: Diagram of the components mounted on the vacuum manipulator. From top to bottom the components are: microwave horn, MCP, passthrough electrode, electron gun, and microwave mirror. The entire assembly is moved up or down to position the desired component in line with the Penning trap electrodes.

gun, the MCP/phosphor screen, a microwave horn, and a microwave mirror (see Fig. 2.12). The manipulator is driven by a stepper motor that accurately and precisely positions the components during an experiment. During a given experiment (e.g. an antihydrogen trapping attempt) the manipulator will move multiple times, taking roughly 10 s to move between components.

2.8 Microwave injection

Microwave radiation at frequencies ranging from 25 to 30 GHz is generated by an Agilent 8257D synthesizer and transmitted via coaxial cable through one of two potential paths. Microwave experiments with antihydrogen (Chapter 8) use a high-power path that features a microwave amplifier, which can output up to 4 W at 28 GHz. An alternative low-power path is used for microwave experiments with electron plasmas (Chapter 7). These two paths join at a switch just before the microwave signal is coupled into a flexible rectangular wave-guide. The microwaves are then transmitted through a quartz window into a rigid waveguide within the trap vacuum that connects to the microwave horn mounted on the vacuum manipulator. Between the synthesizer and the internal horn the low-power path has an overall loss of 10.8 dB and the high-power path has an overall gain of roughly 8 dB.

2.9 Control System and Data Acquisition

Central to the ALPHA control system is the Sequencer. All of the hardware outlined here - from the Penning trap electrodes, to the superconducting magnets, to the microwave synthesizer - must be carefully linked and controlled together. The Sequencer is split into a digital sequencer that handles the triggering of instruments and any return triggers from them, and an analog sequencer that controls the timing and amplitude of voltages applied to the Penning trap electrodes. The Sequencer operates by processing a list of sequencer states that consist of the state execution time, an array of digital outputs, an optional list of input triggers required to move to the next state, and timing and amplitude for electrode signals.

The low-level Sequencer code is run on a National Instruments PXI 7811R Field Programmable Gate Array (FPGA) controller. The timing jitter of the Sequencer outputs is at the sub-nanosecond level and will respond to input triggers with a jitter of approximately 100 ns. The FPGA is connected to a breakout board that generates TTL-compatible logic to send or receive triggers. At the highest level, the user creates a highly customizable ‘sequence’ of states using a National Instruments LabVIEW application. The Sequencer provides the user with a versatile and robust control system.

Data produced by the experiment is logged primarily by the Maximum Integration Data Acquisition System (MIDAS) software.[1] MIDAS records and logs data from a wide variety of hardware and software systems including data from the scintillator and silicon detectors, as well as instruments monitoring temperatures, pressures, voltages and fields. The data is processed with custom code written in a C++ based data analysis framework known as ROOT[2], a standard package in high energy physics.

2.10 ALPHA-2 Catching Trap

In addition to the ALPHA-1 apparatus discussed in the previous section, this thesis will make reference (in Chapters 6 and 7) to measurements with a second Penning trap system, known as the ALPHA-2 catching trap. This trap was constructed as part of a new version of the ALPHA experiment (ALPHA-2), which is optimized for laser experiments with antihydrogen. The ALPHA-2 catching trap plays the role of the catching trap region of the ALPHA-1 Penning trap described in Sec. 2.3.2. With a dedicated Penning trap for antiproton catching, antiprotons can be accumulated from the AD while precision measurements on antihydrogen are made in a separate Penning trap that includes a magnetic trap and optical access for laser spectroscopy.

The ALPHA-2 catching trap operates in a very similar fashion to the ALPHA-1 trap. It features 20 electrodes with a radius of 14.8 mm and a total length of $\sim$450 mm. A uniform solenoidal magnetic field of 3 T is used during normal antiproton operation but is lowered to 1 T for the measurements presented in Chapter 7. Unlike the ALPHA-1 Penning trap, the catching trap is cooled by a closed system cryocooler from SHI Cryogenics[3] rather than a liquid helium cryostat. A vacuum manipulator, based on the ALPHA-1 design (Sec. 2.7), is used. It includes a passthrough electrode,

---

[1] MIDAS website: `http://ladd00.triumf.ca/~daqweb/doc/midas/html/`

[2] ROOT Object-Oriented Framework website: `http://root.cern.ch`

[3] `http://www.shicryogenics.com/`

an MCP/phosphor screen detector, an electron gun, and a microwave mirror. A degrading foil, which doubles as a Faraday cup, sits at the AD end of the Penning trap. Microwaves are injected perpendicular to the trap axis from an external horn mounted outside a vacuum window. The microwaves are redirected down the axis of the catching trap electrodes by the microwave mirror mounted on the vacuum manipulator.

Chapter 3

Non-neutral Plasmas in a Penning trap

Section 2.3 discussed the motion of single particles in a Penning trap but antihydrogen is formed by mixing dense clouds, consisting of 10^4 to 10^7 particles, of antiprotons and positrons. As the density of the clouds increase, they behave less like a collection of single particles and more like a plasma, exhibiting a wide range of collective behaviours. Plasmas are often described as the fourth state of matter (after solids, liquids, and gases) that form when neutral gases are ionized into equal (or nearly equal) numbers of positive (ions) and negative (electrons) charge carriers. Such plasmas, known as 'quasi-neutral' plasmas, can be found throughout the universe including astrophysical bodies (in stars, nebulae, etc...), in the solar wind, and in the Earth's magnetosphere. Quasi-neutral plasmas are also of great interest in controlled fusion experiments with the goal of harnessing fusion reactions in high temperature (10^8 K) trapped plasmas. The charged clouds used in ALPHA, on the other hand, are as non-neutral as possible, consisting entirely of a single sign of charge. Despite their non-neutrality, these clouds share many of the collective phenomena associated with quasi-neutral plasmas and are thus known as 'non-neutral' plasmas.

The physics of non-neutral plasmas is one of the most important aspects of the ALPHA experiment. From the time that the antiprotons are captured to the formation of antihydrogen, plasma effects must be considered at every step. The collective behaviour of the plasmas can result in deleterious effects such as instabilities and plasma heating. On the other hand, the collective behaviour also allows us to use powerful techniques like rotating-wall compression (Sec. 4.2) and autoresonant injection (Sec. 5.1.3). Non-neutral plasmas also exhibit a broad range of wave and oscillatory motions [82–84]. In particular, in a Penning trap there exists a set of normal modes of oscillation, which have been studied extensively [83, 85]. These modes are of special interest here as their frequencies can be used as non-destructive diagnostics that are not available when working with single particles. The use of one of these modes as a diagnostic tool (see Chapters 6 and 7) was integral to the demonstration of positron spin flips in antihydrogen (Chapter 8). This chapter will cover the relevant theory of non-neutral plasmas in Penning traps, including the confinement of non-neutral plasmas (Sec. 3.1), their thermal equilibrium state (Sec. 3.2), collision rates (Sec. 3.3), and the normal plasma modes (Sec. 3.4). In addition, this chapter will present the method by which ALPHA measures the thermal equilibrium temperature of plasmas (Sec. 3.5).

Before beginning, it is useful to define two fundamental quantities in plasma physics. The first is the plasma frequency given by

$$\omega_p = \sqrt{\frac{nq^2}{\epsilon_0 m}}, \tag{3.1}$$

where n is the number density, q is the particle charge, m is the particle mass, and ϵ_0 is the vacuum permittivity. The plasma frequency corresponds to the oscillation frequency of a plasma in response to a small charge displacement. This sets the characteristic timescale, $\tau = 1/\omega_p$, over which plasma behaviour is observed. The second quantity is the characteristic distance, known as the Debye length, over which plasma behaviour is observed. The Debye length is given by

$$\lambda_{\mathrm{D}} = \sqrt{\frac{k_{\mathrm{B}}T}{m}}\tau, \tag{3.2}$$

$$= \sqrt{\frac{\epsilon_0 k_{\mathrm{B}}T}{nq^2}}, \tag{3.3}$$

where T is the plasma temperature and k_{B} is Boltzmann's constant. For a cloud of charges to be considered a plasma, the cloud size must be large compared to the Debye length. The Debye length also sets the scale over which plasmas shield out external electric fields. Because plasmas are highly conductive by nature, plasma current will flow to cancel out electric fields within the plasma interior.

3.1 Confinement of non-neutral plasmas

Following the treatment in reference [69], a non-neutral plasma of N equal charges in a cylindrically symmetric Penning trap is considered. Static voltages are applied to electrodes on either end of the plasma and a uniform magnetic field is directed down the trap axis ($\vec{B} = B\hat{z}$). In the presence of a plasma, the electric potential can be written as

$$\phi(\vec{r}) = \phi_{\mathrm{T}}(\vec{r}) + \phi_{\mathrm{P}}(\vec{r}), \tag{3.4}$$

where $\phi_{\mathrm{T}}(\vec{r})$ is the applied trap potential in the absence of the plasma and $\phi_{\mathrm{P}}(\vec{r})$ is the plasma self-potential. For positron and electron plasmas in ALPHA the plasma self-potential, or 'space charge', is often tens of volts, which is comparable to the applied trap potentials. Working in a cylindrical coordinate system, with the z-axis defined to lie along the trap axis, the Hamiltonian governing the motion of the charges is

$$H = \sum_{j=1}^{N} \left(\frac{p_{r_j}^2}{2m} + \frac{\left[p_{\theta_j} - \frac{q}{2}Br_j^2\right]^2}{2mr_j^2} + \frac{p_{z_j}^2}{2m} \right) + q\sum_{j=1}^{N} \left(\phi_{\mathrm{T}}(\vec{r_j}) + \phi_p(\vec{r_j})\right), \tag{3.5}$$

where the canonical momenta are

$$p_{r_j} = m\dot{r}_j, \quad p_{\theta_j} = mr_j^2\dot{\theta}_j + \frac{q}{2}Br_j^2, \quad p_{z_j} = m\dot{z}_j. \tag{3.6}$$

Because the Hamiltonian is invariant under time translations, it is a constant of motion and the total particle energy is conserved. Additionally, the cylindrical symmetry of the apparatus implies that the potential is independent of θ and can be written as $\phi(\vec{r}) = \phi(r, z)$. It follows that the Hamiltonian itself is invariant under θ translations and therefore the total canonical angular momentum

$$P_\theta \equiv \sum_{j=1}^{N} p_{\theta_j} = L, \tag{3.7}$$

is conserved.

Axial confinement of the plasma can be virtually guaranteed by applying sufficiently large voltages to the electrodes but the radial confinement is less apparent. A radial confinement theorem can be constructed from the fact that total canonical angular momentum is conserved. From Eqs. 3.7 and 3.6 it follows that

$$L = \sum_{j=1}^{N} mr_j^2\dot{\theta}_j + \frac{q}{2}Br_j^2 = \text{const.} \tag{3.8}$$

In a strong magnetic field, the second term dominates and Eq. 3.8 reduces to

$$\text{const} = L \simeq \frac{qB}{2}\sum_{j=1}^{N} r_j^2. \tag{3.9}$$

Therefore, the mean-square radius of the plasma is a conserved quantity. This means that for a plasma with a mean square radius of $\langle r^2 \rangle = 1\ \text{mm}^2$ in a trap with an electrode radius of $r_\text{w} = 22.5$ mm, only a maximum of $\langle r^2 \rangle / r_\text{w}^2 = 0.2\%$ of the particles can transit out to the electrode walls (while the remainder sit at $r = 0$ to conserve $\langle r^2 \rangle$).

In experiments, of course, the total canonical angular momentum is not exactly conserved. Collisions with neutral particles can change the plasma energy and angular momentum, gradually expanding the plasma. Small errors in the magnetic field or construction of the trap will break the cylindrical symmetry and apply a small torque to the plasma. Fortunately, these effects can be made small and plasmas are routinely confined for hours or even days. The addition of a multipole field for antihydrogen trapping, however, breaks the cylindrical symmetry significantly and results in plasma heating and expansion. This was a primary motivating factor in the choice of an octupole magnet rather than quadrupole or sextupole magnets for the ALPHA neutral atom trap (see Sec. 2.4). The octupole field still results in some plasma heating and expansion but these effects are minimized by producing small radius plasmas.

3.2 Thermal Equilibrium

Non-neutral plasmas have an advantage over neutral plasmas in that they can be confined by static electric and magnetic fields in a state of thermal equilibrium [69]. This makes the plasmas controllable and predictable and the thermal equilibrium state provides a convenient theoretical description of the plasma's density and shape.

When correlations between the charges in the plasma are small, the thermal equilibrium state can be described by a Boltzmann distribution. Correlation strength is measured by the coupling parameter $\Gamma = q^2/(4\pi\epsilon_0 a k_{\mathrm{B}} T)$, where a is the inter-particle spacing. The coupling parameter is simply the ratio of the interaction energy between neighbouring charges, $q^2/(4\pi\epsilon_0 a)$, to the random energy per degree of freedom, $k_B T$. When $\Gamma \ll 1$, correlations are weak. Since the total Hamiltonian and total canonical angular momentum are both conserved, the Boltzmann distribution can be written as [69]

$$f(\vec{r},\vec{v}) = n(r,z)\left(\frac{m}{2\pi k_{\mathrm{B}} T}\right)^{3/2} \exp\left[-\frac{m}{2k_{\mathrm{B}}T}(\vec{v}+\omega_r r\hat{\theta})^2\right], \tag{3.10}$$

where the density as a function of r and z is given by

$$n(r, v) = n_0 \exp\left[-\frac{q\phi(r,z) + \frac{1}{2}m\omega_r(\omega_c - \omega_r)r^2}{k_\mathrm{B}T}\right], \tag{3.11}$$

and $\omega_c = qB/m$ is the single particle cyclotron frequency. Equation 3.10 describes a Maxwell-Boltzmann velocity distribution superimposed with a rigid-body rotation of the plasma with a frequency ω_r. This rotation is an $\vec{E} \times \vec{B}$ drift, similar to the magnetron motion of a single particle (see Sec. 2.3), where the electric field here is due to both the applied fields and self-field of the plasma.

For the interior density of the plasma (Eq. 3.11) to remain finite in the $T \to 0$ limit, the following condition must be satisfied:

$$q\phi(r,z) + \frac{1}{2}m\omega_r(\omega_c - \omega_r)r^2 = 0. \tag{3.12}$$

Therefore, in a zero temperature plasma the total electric potential is independent of z and there is no force along a magnetic field line within the plasma. The electric potential and the density distribution must also satisfy Poisson's equation, $\nabla^2\phi(r,z) = -qn(r,z)/\epsilon_0$. Substituting $\phi(r,z) = -m\omega_r(\omega_c - \omega_r)r^2/2q$ into Poisson's equation yields a constant density given by

$$n_0 = \frac{2\epsilon_0 m\omega_r(\omega_c - \omega_r)}{q^2}, \tag{3.13}$$

throughout the plasma. Above the $T \to 0$ limit the plasma density remains nearly constant up to the edge of the plasma where it drops to zero on the scale of the Debye length (see Eq. 3.3). The relationship between density and rotation frequency is the basis for the rotating wall technique that will be described in Sec. 4.2 to manipulate plasma radii.

The plasma's thermal equilibrium shape can be calculated analytically by assuming a quadratic trap potential of the form

$$\phi_\mathrm{T}(r,z) = \frac{m\omega_z^2}{2q}\left(z^2 - \frac{r^2}{2}\right), \tag{3.14}$$

where ω_z is the axial oscillation frequency of a single particle as determined by the applied trapping potential (see Sec. 2.3). Given $\phi(r,z) = \phi_{\mathrm{T}}(r,z) + \phi_{\mathrm{P}}(r,z)$ and Eq. 3.12, the plasma self-potential is given by

$$\phi_{\mathrm{P}}(r,z) = \phi(r,z) - \phi_{\mathrm{T}}(r,z), \tag{3.15}$$

$$\begin{aligned} \phi_{\mathrm{P}}(r,z) &= \frac{m\omega_r}{2q}(\omega_c - \omega_r)r^2 - \frac{m\omega_z^2}{2q}\left(z^2 - \frac{r^2}{2}\right), \\ &= \frac{m}{4q}\left(\omega_z^2 - \omega_p^2\right)r^2 - \frac{m\omega_z^2}{2q}z^2, \end{aligned} \tag{3.16}$$

where we have made the simplifying substitution, $\omega_p^2 = 2\omega_r(\omega_c - \omega_r)$, derived from Eqs. 3.13 and 3.1 (with $n = n_0$). Assuming the plasma dimensions are small with respect to the electrode radius, so that image charge effects can be neglected, the quadratic form of the plasma self-potential (Eq. 3.16) implies that the plasma is a uniformly charged spheroid [69]. The shape of the plasma can therefore be described using its aspect ratio, $\alpha = L_{\mathrm{p}}/2r_{\mathrm{p}}$, where r_{p} is the semi-minor axis length and L_{p} is the major axis length. For convenience, r_{p} and L_{p} are referred to as the plasma radius and length, respectively. By comparing the coefficients of r^2 and z^2 in Eq. 3.16 to the corresponding coefficients in the potential due to a uniformly charged spheroid, the shape of the spheroidal plasma can be related to ω_p (and therefore the plasma density) and ω_z through the following equation [83]

$$\frac{\omega_z^2}{\omega_p^2} = \frac{Q_1^0\left(\frac{\alpha}{\sqrt{\alpha^2-1}}\right)}{\alpha^2 - 1}, \tag{3.17}$$

where $Q_1^0(x)$ is the associated Legendre function of the second kind.

The above discussion assumes an ideal quadrupole potential, which is not the case in the ALPHA Penning trap. In practice, the thermal equilibrium shape is computed by using an iterative algorithm to solve the Poisson Equation and the Boltzmann distribution numerically. The algorithm begins with an initial guess for the charge distribution, which is used to calculate the electric potential from Poisson's equation.

With this potential, a new charge distribution is calculated from the Boltzmann distribution, which in turn is used to calculate a more accurate charge distribution. This process is repeated until a specified convergence level is reached. As inputs, the algorithm requires the applied electrode voltages and measurements of the particle number, radial profile, and temperature. From these calculations, the plasma density, plasma length, and the total electric potentials and fields are calculated.

3.3 Collision rate

Plasmas will relax into thermal equilibrium through Coulomb collisions between the particles. The time-scale over which this occurs is an important parameter to consider when designing experiments. In ALPHA, this time-scale is limited by the exchange of energy between components of the motion parallel to the magnetic field and perpendicular to the magnetic field. This is due to the fact that in strong magnetic fields the particles are tightly bound to magnetic field lines with a characteristic cyclotron radius $r_c = \sqrt{mk_\mathrm{B}T}/qB$ that is small compared to the distance of closest approach between particles $b = q^2/(4\pi\epsilon_0 k_\mathrm{B}T)$. This suppresses the transfer of energy between the parallel and perpendicular components of the motion. In this regime, the plasma has an anisotropic velocity distribution characterized by two different temperatures: one parallel to the magnetic field ($T_{||}$) and the other perpendicular ($T_\perp$). The collisional equipartition rate between these two temperatures, in the limit that $(T_{||} - T_\perp)$ is small, is given by [86]

$$\Gamma_\mathrm{col} = n\bar{v}\bar{b}^2 I(\bar{\kappa}), \tag{3.18}$$

where $\bar{v} = \sqrt{2k_\mathrm{B}T/m}$ is the thermal velocity, $\bar{b} = 2b$, $\bar{\kappa} = (\bar{b}/r_c)/\sqrt{2}$ is a measure of the magnetic field strength, and we have set $T = T_{||} \simeq T_\perp$. The function $I(\bar{\kappa})$ accounts for the dependence on the magnetic field strength. In the limit where $\bar{\kappa} \gg 1$, the plasma is strongly magnetized and $I(\bar{\kappa})$ approaches $I(\bar{\kappa}) \sim \exp(-5(3\pi\bar{\kappa})^{2/5}/6)$ [87].

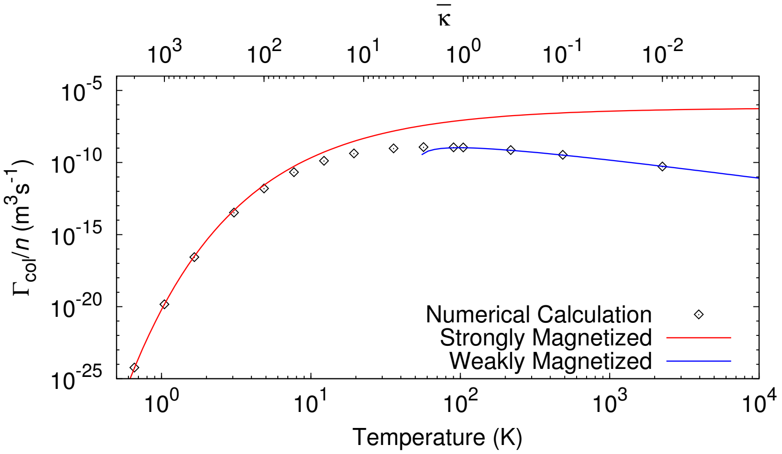

Figure 3.1: The collisional equipartition rate that the parallel and perpendicular velocity components of an electron/positron plasma in a 1 T field come into equilibrium. The points are the result of numerical calculations of $I(\bar{\kappa})$ found in [86].

In the opposite limit, where $\bar{\kappa} \ll 1$, the plasma is weakly magnetized and $I(\bar{\kappa})$ approaches $I(\bar{\kappa}) \sim \ln(\bar{\kappa})$. These two regimes can be bridged by a numerical calculation of $I(\bar{\kappa})$ that produces a smooth function over the entire range of $\bar{\kappa}$ that agrees well with experimental results [86]. Figure 3.1 plots Γ_{col}/n for electron/positron plasmas as a function of plasma temperature and $\bar{\kappa}$. In ALPHA, electron and positron plasmas typically have temperatures between 40 K and 200 K which places them in the intermediate regime ($\bar{\kappa} \approx 1$). For example, just before antihydrogen formation, typical positron plasmas ($T = 40$ K, $n = 5.5 \times 10^{13}$ m^{-3}) have a collision rate of $\Gamma_{\mathrm{col}} \sim 5 \times 10^4$ s^{-1}. Antiproton plasmas are typically hotter (> 100 K) and combined with their larger mass they typically fall in the unmagnetized regime $\bar{\kappa} \ll 1$. A typical antiproton plasma used for antihydrogen formation ($T = 200$ K, $n = 6.5 \times 10^{12}$) has a collision rate of roughly $\Gamma_{\mathrm{col}} \sim 400$ s^{-1}.

3.4 Plasma Modes

Displacements from the thermal equilibrium state will cause a non-neutral plasma to oscillate about this equilibrium. For small displacements, the motion of the plasma can be described in terms of a set of normal modes of oscillation. For a spheroidal plasma in limit that $T \to 0$, an analytical treatment of these modes exists [85]. The normal modes are parametrized by a pair of integers (ℓ, m), where ℓ is the axial mode number and m is the azimuthal mode number. A full treatment of these modes can be found in [83]. Here we are interested only in the low-order axisymmetric modes ($m = 0$), which have been studied experimentally and used as non-destructive diagnostics of plasma properties [88]. The frequencies of the $(\ell, 0)$ modes are related to the plasma density and aspect ratio through the following equation [85]:

$$1 - \frac{\omega_p^2}{\omega_\ell^2} = \frac{k_2}{k_1} \frac{P_\ell(k_1) Q_\ell^{'}(k_2)}{P_\ell^{'}(k_1) Q_\ell(k_2)}, \tag{3.19}$$

where $k_1 = \alpha(\alpha^2 - 1 + \omega_p^2/\omega_\ell)^{-1/2}$, $k_2 = \alpha(\alpha^2 - 1)^{-1/2}$, and P_ℓ and Q_ℓ are Legendre functions of the first and second kinds, respectively, while $P_\ell^{'}$ and $Q_\ell^{'}$ are their derivatives.

The two first order modes are of particular interest in ALPHA. The $\ell = 1$ mode, known as the dipole mode, is a centre-of-mass oscillation of the plasma along the z-axis (Fig. 3.2a). The frequency of this mode is equivalent to the single particle bounce frequency ω_z as given by Eq. 3.17. The $\ell = 2$ mode, known as the 'breathing' or quadrupole mode, is an oscillation of the plasma's aspect ratio (Fig. 3.2b). By measuring the frequency of these two modes the density and aspect ratio of the plasma can potentially be determined non-destructively (i.e. without releasing the plasma onto an MCP detector or Faraday cup).

For non-zero plasma temperatures, the dipole mode frequency is unchanged but the quadrupole mode frequency is shifted from the analytic result. An approximate

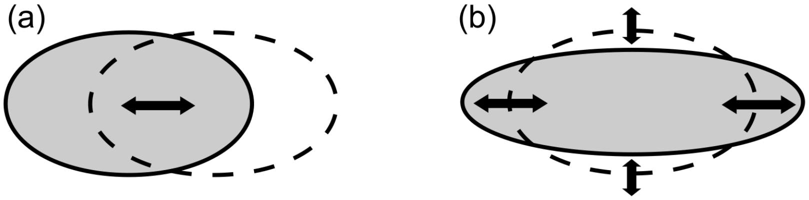

Figure 3.2: Sketch of the motions of the (a) dipole mode and (b) quadrupole mode of a non-neutral plasma.

treatment of non-zero temperature effects predicts that the quadrupole mode frequency will be shifted to a frequency given by [89]

$$(\omega_2)^2 = (\omega_2^c)^2 + 20\left(3 - \frac{\alpha^2}{2}\frac{\omega_p^2}{(\omega_2^c)^2}\frac{\partial^2 g(\alpha)}{\partial \alpha^2}\right)\frac{k_\mathrm{B}T}{mL_\mathrm{p}^2}, \tag{3.20}$$

where ω_2^c is the $T \to 0$ result. The function $g(\alpha)$ is given by $g(\alpha) = 2Q_1[\alpha(\alpha^2 - 1)^{-1/2}]/(\alpha^2 - 1)$, where Q_1 is the first order Legendre polynomial of the second kind. This temperature dependence will be exploited in Chapter 6 to realize a non-destructive measurement of changes in plasma temperature. The dipole mode is not used as a diagnostic tool by ALPHA, but rather is used to heat positron and electron plasmas by applying an RF drive at the dipole mode frequency. This method of plasma heating is used as part of a background experiment for detecting trapped antihydrogen (see Sec. 5.2.1) and to study the temperature dependence of the cyclotron resonance lineshapes measured in Chapter 7. The methods for excitation and detection of the dipole and quadrupole modes will be discussed in Chapter 6.

3.5 Temperature measurements

Extensive characterization of plasmas is critical to antihydrogen production and trapping. The number of particles in a plasma and its size are characterized in a destructive manner by lowering the confining potential on one side of the plasma, releasing the particles onto either the Faraday cup (Sec. 2.6.1) or the MCP/phosphor screen detector (Sec. 2.6.2), respectively. From the particle number and radial profile, the density and aspect ratio of the plasma can be determined. Many of the techniques and manipulations used by ALPHA are systematically studied and optimized with these diagnostic 'dumps'.

The plasma temperature can also be destructively measured by slowly (relative to ω_z^{-1}) reducing the confining well depth and measuring the energy distribution of the escaped particles. Assuming that the plasma is in thermal equilibrium, with $T = T_{||} = T_{\perp}$, the number of particles that escape as a function of well depth will be given by the Boltzmann distribution [90]

$$N(E_{||}) \propto \exp\left(-\frac{E_{||}}{k_{\mathrm{B}}T}\right), \tag{3.21}$$

where $E_{||}$ is the particle energy parallel to the trap axis. As the well depth lowers, however, the measured distribution begins to deviate from a Boltzmann distribution. This is due to the fact that the plasma itself contributes to the overall confining potential and as particles escape this self-potential will change, causing deviation from Eq. 3.21 [90]. The temperature is therefore measured by fitting an exponential to the first escaping particles, corresponding to particles from the high energy tail of the Boltzmann distribution.

For electron and positron plasmas, the energy distribution is measured by the MCP/phosphor screen detector. The microchannel plate amplifies the small number of incident particles, producing a measurable charge on the phosphor screen. Antiproton plasma temperatures are measured by instead releasing the particles onto the degrader foil/Faraday cup. The scintillating detectors placed at the degrader position (see Sec. 2.6.3) measure the number of antiproton annihilations as a function of energy. Figure 3.3 shows several examples of antiproton temperature measurements. Small corrections to the fit temperature are applied to account for the effects of the time-dependant applied and plasma potentials as well as any particle evaporation

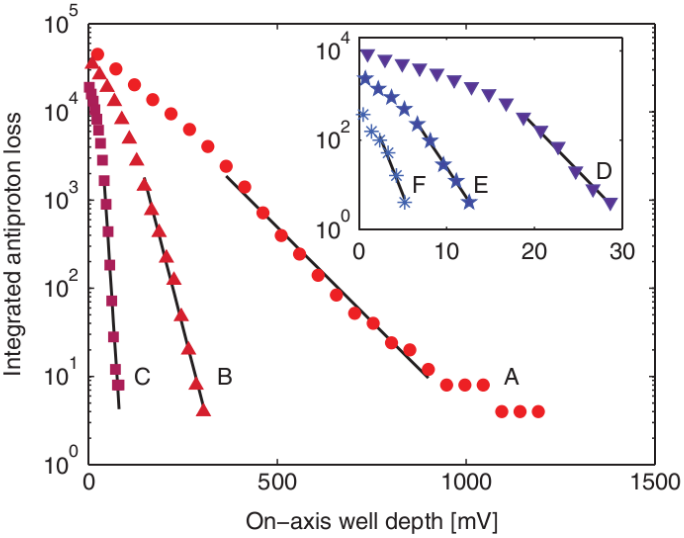

Figure 3.3: A plot of the integrated number of antiprotons lost from the well as its depth is reduced. The corrected temperatures are: A - 1040 K, B - 325 K, C - 57 K, D - 23 K, E - 19 K and F - 9 K. The measured y-axis values are adjusted to account for the 25% detection efficiency of the scintillators. (Reproduced with permission from reference [50])

(see Sec. 4.4) that may occur as the confining well is lowered [50]. For the plasmas in Fig. 3.3, the corrected temperatures are $\sim 16\%$ lower than the fit temperature.

Low plasma temperatures are critical to trapping antihydrogen. The temperature measurements discussed here are used extensively in ALPHA to characterize and optimize plasma temperatures each time plasmas are manipulated or moved.

Chapter 4

Experimental Techniques

This chapter covers some of the important experimental techniques used in ALPHA. A common theme among these techniques is the desire to obtain cold and dense antiproton and positron plasmas for antihydrogen formation. Production of antihydrogen begins with the catching and cooling of antiprotons (Sec. 4.1) delivered from the antiproton decelerator in the catching region of the ALPHA Penning trap. Simultaneously, a positron plasma is prepared in the positron accumulator (see Sec. 2.2.2) and then transferred to the positron region of the Penning trap. These plasmas are then separately prepared for eventual mixing by applying the techniques outlined in Sec. 4.2, Sec. 4.3, and Sec. 4.4. At this stage the plasmas are ready to be mixed together to form trappable antihydrogen atoms. This sequence of operations is presented in greater detail in Sec. 5.2.

The techniques described below are characterized and optimized with diagnostic measurements using the MCP/phosphor screen detector (Sec. 2.6.2 and Sec. 3.5) and the Faraday cup (Sec. 2.6.1). The order in which these techniques are presented is the same order in which they are used, starting from antiproton injection up to just before the antiprotons and positrons are mixed to form antihydrogen.

4.1 Antiproton Catching and Cooling

Antiprotons from the Antiproton Decelerator (AD) are injected into the ALPHA Penning trap at an energy of 5 MeV. The energy is reduced further when they pass through a 185 μm thick degrading foil at the upstream end of the trap [63]. As the antiprotons pass through the foil they lose energy through collisions in the foil and, while many are stopped and annihilate, a small fraction of the antiprotons emerge with reduced energies [91]. A fraction of these low energy antiprotons can then be 'caught' by high-voltage potentials in the Penning trap [92]. Antiproton catching proceeds by first applying a ∼4 keV potential to a specially designed high-voltage electrode in the catching region of the Penning trap (see Fig. 2.4). A small fraction (∼0.1%) of the incoming antiprotons are reflected back by this potential but before they can leave the trap a second high-voltage electrode is quickly energized to form a confining well (see Fig. 4.1). The catching and subsequent cooling of antiprotons is assisted by an additional superconducting solenoid that surrounds the catching region of the Penning trap. This solenoid is energized to bring the total field from 1 T to 3 T for catching and cooling of antiprotons and then switched off again. The increased magnetic field has been observed to increase the number of antiprotons that are captured [93].

The captured antiprotons are still at very high energies and are cooled further using electron cooling [28]. Electrons self-cool quickly in a strong magnetic field by the emission of cyclotron radiation. If electrons are combined with the antiproton cloud, collisions will transfer energy from the antiprotons to the electrons, which then cool via cyclotron radiation. The rate of energy loss by a charged particle orbiting in a magnetic field due to the emitted radiation is given by the Larmor formula [94]

$$\frac{dE_\perp}{dt} = -\frac{q^2}{6\pi\epsilon_0 c^3} a_\perp^2, \tag{4.1}$$

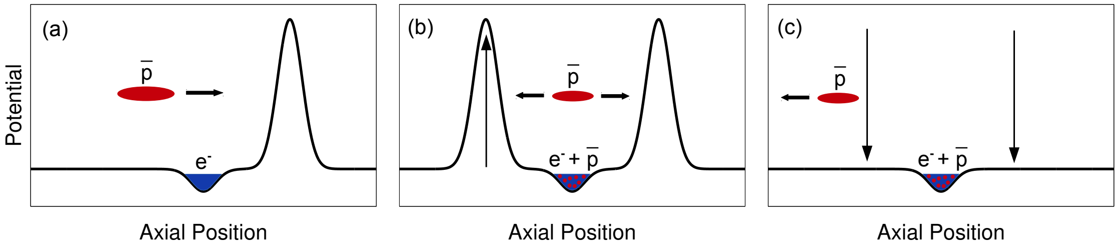

Figure 4.1: Sketch of the antiproton catching sequence. (a) An electron plasma (blue) is preloaded into the well before the antiproton beam (red) arrives. (b) The high-voltage well is formed and collisions between the antiprotons and electrons cool a portion of the antiprotons into the electron well. (c) When the high-voltage well is removed, the cold antiprotons remain trapped with the electron plasma while the remaining high-energy antiprotons escape.

where $E_\perp$ is the kinetic energy perpendicular to the magnetic field and $a_\perp = \omega_c v_\perp$ is the perpendicular acceleration due to the cyclotron motion. The axial and magnetron motions of the particles will also radiate but because their frequencies are typically in the radio-frequency range, the emission rates are negligible. Noting that $E_\perp = mv_\perp^2/2$ is the perpendicular kinetic energy, Eq. 4.1 can be written as

$$\frac{dE_\perp}{dt} = -\frac{1}{\tau_c}E_\perp, \tag{4.2}$$

where the characteristic cyclotron cooling time is

$$\tau_c = \frac{3\pi\epsilon_0 mc^3}{q^2\omega_c^2} = \frac{3\pi\epsilon_0 m^3 c^3}{q^4 B^2}. \tag{4.3}$$

Assuming the two perpendicular degrees of freedom come into equilibrium with the axial degree of freedom, the net plasma cooling rate can be obtained by multiplying Eq. 4.3 by a factor of 2/3. In a 3 T field, the net cooling time for antiprotons is $\tau_{\mathrm{net},\bar{p}} \sim 1 \times 10^9$ s, (slightly) too long to be an effective cooling mechanism. Electrons in a 3 T field, on the other hand, lose energy much faster with a cooling time of $\tau_{\mathrm{net},e^-} \sim 0.2$ s. To cool the antiprotons, an electron plasma is pre-loaded into the confining well before the beam arrives (see Fig. 4.1). The combined electron-antiproton plasma will continue to cool until equilibrium is reached. After a set time, the high-voltage electrodes are discharged and the fraction of antiprotons that have been cooled (typically ~50%) remain trapped in the electron well, while the remainder escape and annihilate.

4.2 Rotating Wall

Control of the plasma radius and density is also an important tool in non-neutral plasma experiments and especially in antihydrogen formation and trapping. Creating smaller, denser plasmas increases the formation rate of antihydrogen (see Sec. 5.1.1) while also reducing the perturbative effect of the octupole magnetic field.

Non-neutral plasmas can be compressed by applying a torque to the plasma to increase the plasma's rotation frequency. Because the plasma density is proportional to its rotational frequency (Eq. 3.13), the density will similarly increase. In the rotating wall technique, torque is applied by a rotating transverse electric field generated by a special segmented electrode (Fig. 4.2). A voltage

$$V_i = V_0 \sin(\omega_{RW} t - \theta_i), \tag{4.4}$$

is applied to each electrode segment. The phase of the ith segment, θ_i, is shifted by an amount $2\pi/N$, where N is the number of segments, from that of its neighbour. The rotating wall technique was developed to compress and extend the storage time of electron [95], ion [72], and positron plasmas [96]. In the initial studies, the torque was applied by tuning the frequency to specific rotational modes of the plasma [97]. More recent work has shown that compression is possible without directly coupling to these modes but instead applying a high amplitude drive [98]. In this so-called 'strong drive' regime, the plasma rotation frequency is driven towards the rotating wall frequency with good compression observed over a wide range of frequencies.

In ALPHA, the rotating wall technique is routinely used to compress electron, positron, and antiproton plasmas. Unlike electron and positron clouds, antiproton clouds do not respond directly to the rotating wall field [42] in the regime studied.

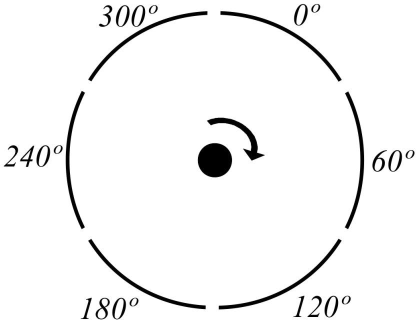

Figure 4.2: A sketch of a six-segment electrode used to apply a rotating wall electric field. The relative phase of the signals applied to each electrode is labelled.

Antiprotons are compressed by mixing them with an electron plasma, which is then compressed by the rotating wall field. If the electron compression proceeds slowly enough, the antiproton cloud size will roughly follow that of the electron cloud. An example of rotating wall compression of an electron plasma can be seen in Figure 4.3.

The application of a rotating wall drive will heat the plasmas, reducing the effectiveness of the compression [72]. To counteract this effect a cooling mechanism is required. For electron and positron plasmas in a 1 - 3 T magnetic field, the cyclotron cooling rate is sufficient to maintain the balance. Antiprotons, which radiate much more slowly, are cooled sympathetically through collisions with the electrons.

4.3 Electron Removal

After antiproton catching, cooling, and compression, it is necessary to remove the electrons and obtain a pure antiproton plasma. If the electrons are not removed before the antiprotons are mixed with positrons, they could potentially deplete the positron plasma through electron-positron annihilations and/or the formation of positronium (an electron-positron atom). Additionally, injecting large amounts of charge into the

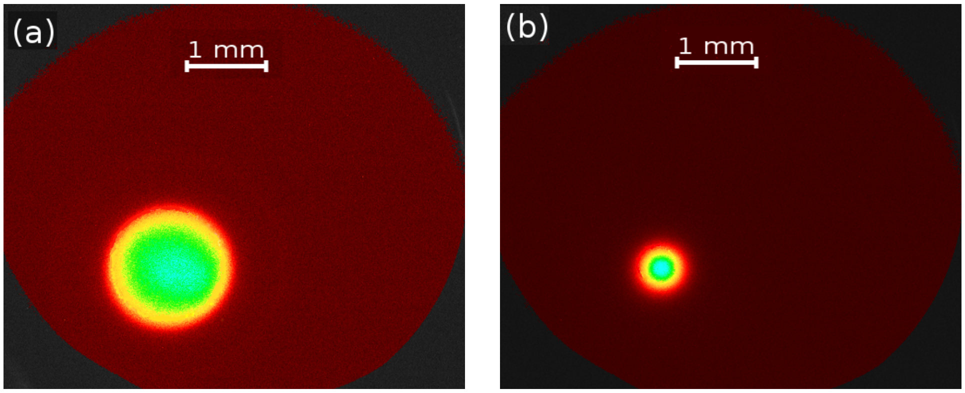

Figure 4.3: False colour images from the MCP/phosphor screen detector of (a) an uncompressed electron plasma and (b) one compressed by the rotating wall technique. Colour indicates relative intensity (red to blue).

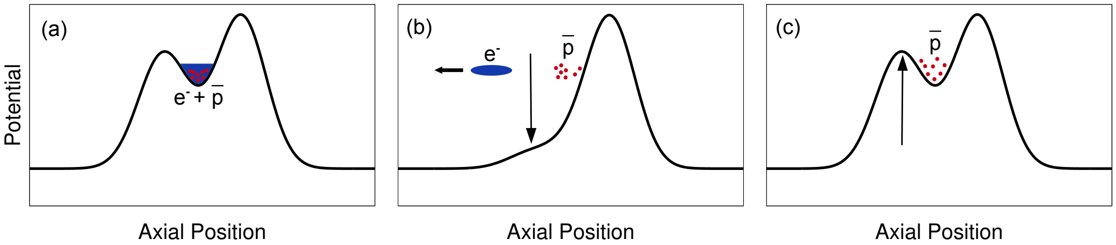

Figure 4.4: A sketch of the electron removal sequence. The combined electron-antiproton plasma (a) is separated by removing one side of the confining well (b). The electrons will escape before the confining well is reformed (c) but the antiprotons will not have time to escape.

positron plasma will heat it significantly and reduce the formation and trapping rates of antihydrogen (Sec. 5.1.1).

Electrons are removed from the antiproton plasma by quickly dropping one side of the confining potential and bringing it back up in a span of roughly 100 ns. Electrons, being much less massive than antiprotons, will rapidly leave the well when the barrier is dropped while the antiprotons will be too slow to escape before the barrier is re-raised. This sequence is illustrated in Fig. 4.4.

The quick change in applied potential as well as the sudden absence of the electron space charge unavoidably heats the antiproton plasma. To reduce the final temperature of the pure antiproton plasma, the electron removal procedure is divided into two steps. First, at least 95% of the electrons are removed by an initial round of electron removal cycles (typically 1 - 3). This leaves the resulting antiproton-electron plasma at temperatures above 1000 K, however the remaining electrons will re-cool the plasma via cyclotron radiation and collisions with the antiprotons. After re-cooling, the confining potentials are reduced (because there is now much less space charge) and a final electron removal cycle will remove the remainder of the electrons. By lowering the confining well depth, the antiproton heating due to the final electron removal cycle is minimized. The applied potentials and timings at each step are carefully optimized using the diagnostic dumps.

After catching, electron cooling, rotating wall compression, and electron removal, the antiprotons energies are reduced from 5×10^6 eV to energies on the order of 10^{-2} eV. The final antiproton plasmas have typical temperatures of 200 - 1000 K and radii of roughly 0.8 mm.

4.4 Evaporative cooling

Evaporative cooling is a powerful technique, which was key to producing the first ever Bose-Einstein-Condensates in the mid 1990's [99–101]. Since then it has become a standard technique in atomic physics and has been used to achieve temperatures as low as 450 pK [102]. Evaporative cooling operates by selectively removing the high kinetic energy particles from a system. This happens naturally in a collection of trapped particles where the high-energy tail of the Maxwell-Boltzmann distribution exceeds the trap depth. These evaporating particles will escape and carry away more than than the average particle kinetic energy from the system, decreasing the temperature of the remaining cloud. If the well depth is further reduced this process continues, driving the system to even lower temperatures.

While evaporative cooling has found common use in neutral particle systems, charged particle evaporation has only found limited applications for trapped ions at high (∼100 eV) energies [103]. The work described in this section represents the first implementation of evaporative cooling to a system of cold charged particles and was key in the trapping of antihydrogen.

One of the fundamental differences between charged and neutral systems is the higher collision rate of charged particles due to the Coulomb interaction. Higher collision rates allow for faster rethermalization of the system as particles escape, making charged particle evaporation feasible at lower particle numbers and densities than neutral systems. However, the self-potential of trapped charged particles makes controlling the confining well depth non-trivial. The self-potential can be calculated numerically from diagnostic dumps as described in Sec. 3.2. The measurements used as input for the calculation typically fluctuate on the order of 10%, resulting in a similar uncertainty in the plasmas' self-potentials. For antiproton plasmas, the space charge is typically ∼30 mV but can be in the 10 V range for positron and electron plasmas. Another difference arises from the type of interaction used for confinement of neutral atoms compared to charged particles. Neutral atoms in evaporative cooling experiments are often confined by static magnetic traps that require strong magnetic fields to create even a small confining well (eg. the ALPHA magnetic trap involves fields of 1 - 2 T but only has a depth of ∼40 μeV). While it is a challenge to create deep wells, this means that the depth of the well can be finely controlled with relatively coarse adjustments to the magnetic field. For example, a change of 1 A in the ALPHA superconducting magnets can change the magnetic trap depth by about 40 neV. Charged plasmas, on the other hand, are relatively easily confined by electrostatic wells, but a change of only 0.1 mV in the applied potentials will change the trap depth by ∼90 μeV (roughly 1 K$\times k_\mathrm{B}$). This means that the electronic noise level can

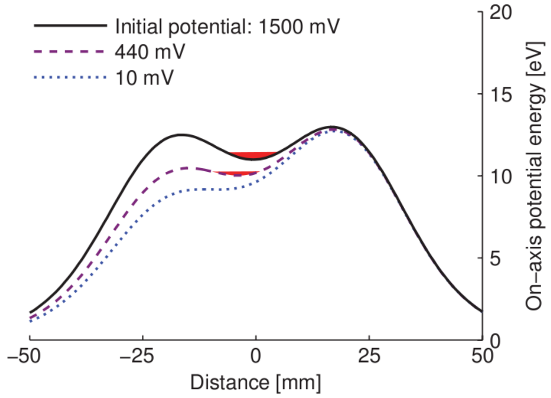

Figure 4.5: Plot of the on-axis potentials used during evaporative cooling of antiprotons (indicated in red). (Reproduced with permission from [50])

be a limiting factor in the minimum achievable temperature.

In ALPHA, evaporative cooling proceeds by confining a non-neutral plasma (consisting of electrons, positrons, or antiprotons) in a deep initial well such that virtually no evaporation occurs. One side of the confining well is slowly lowered by linearly ramping the applied voltage to a predetermined final value (see Fig. 4.5). The first demonstration of evaporative cooling on charged plasmas was performed with antiproton plasmas of approximately 45000 antiprotons at 1040 K in a 1500 mV deep well. These plasmas were evaporated to six different final well depths down to (10 ± 4) mV with ramp times of 300, 100, 30, 10, and 1 seconds. The final temperatures and remaining fraction of particles were found to be independent of the ramp time used with the exception of the 1 s ramp where far fewer particles remained. The resulting temperatures and fractions remaining are plotted as a function of the final well depth in Fig. 4.6.

These results can be modelled by following the treatment in reference [104]. The depth of the potential is denoted as $\eta k_{\mathrm{B}}T$, where T is the plasma temperature, and the average potential and kinetic energy per particle is $(\delta + 3/2)k_{\mathrm{B}}T$. The term δ depends on the well shape and is approximated by $\delta \simeq 1/2$ in ALPHA [105]. The

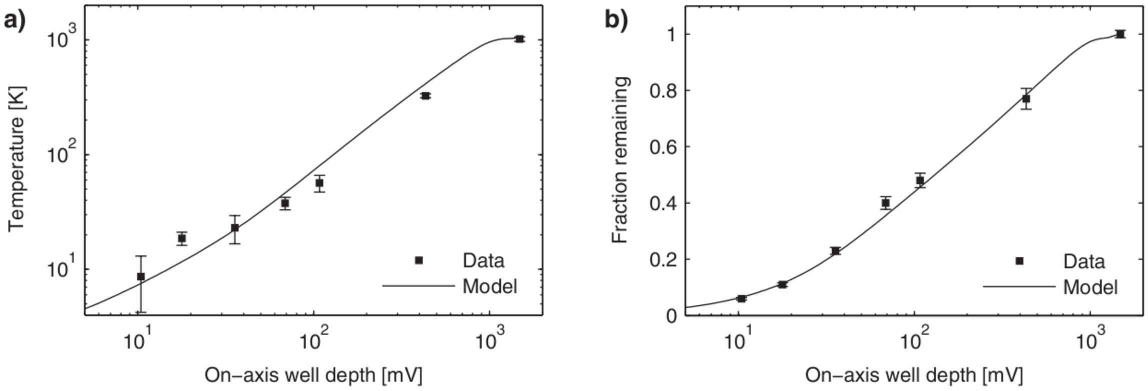

Figure 4.6: (a) Temperature versus the on-axis final well depth. The error bars represent the combined uncertainty of the temperature fit and of the applied potentials. (b) Fraction of antiprotons remaining after evaporative cooling versus the on-axis well depth. Each sample initially contained roughly 45000 antiprotons. (Adapted with permission from [50])

average energy of an evaporated particle is given by $(\eta+\kappa)k_{\mathrm{B}}T$, where κ is a measure of the excess kinetic energy above η and is typically between 0 and 1. The efficiency of the cooling is described by

$$\alpha_{\mathrm{ev}} = \frac{\eta+\kappa}{\delta+3/2} - 1, \tag{4.5}$$

which is the ratio of the average excess energy per evaporated particle to the average energy of the trapped particles. The rate of particle evaporation can be modelled as [50]

$$\frac{dN}{dt} = -\frac{N}{\tau_{\mathrm{ev}}} - \gamma N, \tag{4.6}$$

where N is the number of particles, τ_{ev} is the evaporation timescale, and γ is the rate of particle loss due to non-evaporative processes. For antiprotons, γ is dominated by the rate of annihilation on background gas ($\sim 10^{-4}$ s^{-1} per antiproton). The cooling rate of the antiprotons is given by

$$\frac{dT}{dt} = -\alpha_{\mathrm{ev}}\frac{T}{\tau_{\mathrm{ev}}} + P, \tag{4.7}$$

where P is a heating term. The evaporation time τ_{ev} is related to the antiproton-antiproton collision time τ_{col} by [50]

$$\frac{\tau_{\text{ev}}}{\tau_{\text{col}}} = \frac{\sqrt{2}}{3}\eta e^{\eta}. \tag{4.8}$$

The depth, η, can be estimated from knowledge of the time dependent self and applied potentials. The on-axis self-potential is estimated to be 1.5 μV per antiproton from the antiproton density profiles. The total self-potential during evaporation was measured by counting the antiproton annihilations as they evaporate out of the well and hit the degrader. Knowing the initial number of antiprotons, the self-potential of the remaining particles can be tracked. From η and the collision time, τ_{col} [86], the temperature and remaining number can be modelled as a function of well depth using Eqs. 4.5, 4.6 and 4.7. As seen in Fig. 4.6, there is good agreement between the model and experiment.

The radial profile of the antiproton plasmas was also studied as a function of particles lost. Evaporating particles are most likely to originate from the radial centre of the plasma, where the total potential is weakest. The hollowing of the plasma profile produces an unstable configuration, causing particles to redistribute to fill in the hollow region. The redistribution process must conserve the total canonical angular momentum (Eq. 3.7), which means the plasma will expand as a result. The expansion can be accurately modelled using the following relationship between the measured radius and the particle number

$$R = R_0\sqrt{N/N_0}, \tag{4.9}$$

assuming all of the evaporating particles leave precisely on-axis. Here the final measured radius and particle number are denoted as R and N, respectively, and the pre-evaporation radius and number are given by R_0 and N_0. The measured plasma sizes agree well with this simple models. The antiproton plasmas, consisting of ~45000 antiprotons, start with a measured radius of $R_0 = 0.6$ mm and expand to $R = 3$ mm in the shallowest well. The radial redistribution of the particles during evaporative cooling converts some of the electrostatic potential energy into kinetic energy. This process, known as Joule heating, adds the heating term P to Eq. 4.7 that competes with evaporative cooling. The magnitude of P is estimated to be $(-dN/dT) \times 5$ mK [50], and is not expected to be the limiting factor in the achievable antiproton temperatures.

Antiprotons were used for the initial demonstration of evaporative cooling but the technique has also been applied to positrons. Positron plasmas are typically higher density ($\sim 10^8$ cm^{-3}) than the antiproton plasmas ($\sim 10^6$ cm^{-3}) used in ALPHA. The positron collision rates are roughly an order of magnitude greater than antiproton collision rates so evaporation can be performed much faster. Additionally, the positron plasmas have a much higher self-potential that can be a significant fraction of the vacuum well depth. This complicates the choice of final well depth which is typically optimized through extensive characterization with plasma size and temperature measurements.

Evaporative cooling of antiprotons and positrons is one of the key techniques to producing cold, trappable antihydrogen. In the case of antiprotons, because of their large mass compared to positrons, they largely determine the kinetic energy of the formed antihydrogen atom. While a significant number of antiprotons may be lost during evaporation, reducing the number of antihydrogen atoms that can be formed, the number of particles at low energies will actually increase. In the measurements above for example, the number of antiprotons with energies below the magnetic trap depth for ground state antihydrogen $(0.5 \times k_\mathrm{B})$ is increased by roughly two orders of magnitude despite losing over 90% of the antiprotons [50].

Chapter 5

Antihydrogen Production and Trapping

With the techniques presented in Chapter 4, antiproton and positron plasmas can be cooled, compressed, and prepared to form trappable antihydrogen. The first half of this chapter will cover the production of antihydrogen, including an introduction to antihydrogen formation mechanisms, as well as a novel way to mix antiprotons and positrons developed by ALPHA. The second half presents a detailed discussion of the antihydrogen trapping experiments carried out in 2010, the method of detecting trapped antihydrogen and the relevant background signals, and ultimately the results of the first successful trapping of antihydrogen.

5.1 Production

5.1.1 Formation Mechanisms

When positrons and antiprotons are mixed together, the positrons will bind to the antiprotons to form antihydrogen atoms. There are several possible binding mechanisms to consider, each with a third particle that carries away the binding energy.

5.1.1.1 Spontaneous Radiative Recombination

The simplest process is spontaneous radiative recombination (SRR) wherein a photon carries away the excess binding energy. The reaction can be summarized as

$$e^+ + \bar{p} \to \bar{H} + h\nu, \tag{5.1}$$

where h is Planck's constant and ν is the frequency of the photon. The cross-section for the capture of a positron to a state with principal quantum number n is given by [62]

$$\sigma_{\text{SRR}}(n, E_{e^+}) = \frac{2^5 \pi \alpha_{\text{fs}}^3 a_0^2 E_{\text{g}}}{3\sqrt{3} n E_{e^+} (1 + n^2 E_{e^+}/E_{\text{g}})}, \tag{5.2}$$

where α_{fs} is the fine structure constant and a_0 is the Bohr radius. The binding energy of the lowest atomic state is given by E_{g} and the kinetic energy of the positron in the rest frame of the antiproton is E_{e^+}. The overall capture rate per antiproton can be calculated by integrating Eq. 5.2 over the velocity distribution of the positrons and over all possible quantum states. The rate can be expressed in terms of the positron density n_{e^+} and temperature T as [106]

$$\Gamma_{\text{SRR}}(n_{e^+}, T) = 3 \times 10^{-17} \sqrt{\frac{4.2\ \text{K}}{T}} \frac{n_{e^+}}{\text{m}^{-3}}\ \text{s}^{-1}. \tag{5.3}$$

For a plasma at 4.2 K with a density of 10^{13} m^{-3}, Γ_{SRR} is approximately 3×10^{-4} s^{-1} per antiproton. At a more typical positron temperature observed in ALPHA of 120 K with a density of 10^{13} m^{-3}, Γ_{SRR} is approximately 6×10^{-5} s^{-1} per antiproton.

5.1.1.2 Three-Body Recombination

Antihydrogen formation can also be assisted by a second positron that serves to carry away the excess energy

$$e^+ + e^+ + \bar{p} \to \bar{H} + e^+. \tag{5.4}$$

This process occurs if two positrons collide close to an antiproton, and is expected to be the dominant process in a dense and cold plasma. In a strong magnetic field, the steady-state recombination rate is given by [107]

$$\Gamma_{\text{TBR}} = Cn_{e^+}^2 vb^5, \tag{5.5}$$

$$= C(8 \times 10^{-18}) \left(\frac{4.2\text{ K}}{T}\right)^{9/2} \left(\frac{n_{e^+}}{\text{m}^{-3}}\right)^2 s^{-1}, \tag{5.6}$$

where $v = \sqrt{k_{\text{B}}T/m_{e^+}}$ is the positrons thermal velocity, $b = q^2/(4\pi\epsilon_0 k_{\text{B}}T)$ is the distance of closest approach, and C is a constant. Equation 5.6 can be thought of as the flux of the positrons into a cross-section b^2, $(n_{e^+})vb^2$, multiplied by the probability of finding another positron in that volume, $(n_{e^+})b^3$. The constant C has been calculated numerically for a magnetic field of 1 T and varies from $C = 0.11$ at $T = 4$ K to $C = 0.19$ at $T = 16$ K [108]. In a plasma of density $n_{e^+} = 10^{13}$ m^{-3} at $T = 4$ K the three-body recombination rate is predicted to be $\Gamma_{\text{TBR}} = 1.1 \times 10^2$ s^{-1} per antiproton, six orders of magnitude more than Γ_{SRR}. However, at a positron temperature of 120 K, assuming $C = 0.19$, the strong temperature dependence of Eq. 5.6 will suppress Γ_{TBR} to 4×10^{-5} s^{-1} per antiproton, comparable to the predicted radiative recombination rate.

5.1.1.3 Temperature Dependence

Despite theoretical efforts, the temperature dependence of antihydrogen formation is still not well understood. Experimentally, the ATHENA collaboration studied this temperature dependence by heating the positron plasma and then observing the antihydrogen production rate as the plasma cooled back to equilibrium [109]. A temperature dependence of $T^{-1.1\pm0.5}$ was observed for temperatures between 100 meV ($\sim 1.2 \times 10^3$ K) and 1470 meV ($\sim 1.7 \times 10^5$ K). A similar study in ALPHA found a temperature dependence of $T^{0.5\pm0.1}$ [76] up to temperatures of 1000 K, in rough agreement with the ATHENA result.

Three-body recombination is expected to be the dominant process in ALPHA (and previously in ATHENA) due to the high rates of production observed. The observed temperature scaling, however, is not consistent with the $T^{-4.5}$ scaling predicted by Eq. 5.6. The scaling alone is, in fact, consistent with that of radiative recombination ($T^{-0.5}$). However, the absolute formation rate predicted by Eq. 5.3 is much smaller than observed experimentally [109]. One likely reason for the discrepancy between Eq. 5.6 and observed scalings is that the former assumes that recombination is a steady state process in which positrons are continually interacting with antiprotons. In this process, positrons are typically captured into states with binding energies less than the thermal energy of the surrounding positrons. The majority of the captured positrons will therefore be re-ionized due to collisions with other positrons. Sometimes, however, these collisions will scatter the positrons into states with sufficient binding energies to prevent ionization from collisions and external electric fields. In experiments, however, the antiproton can leave the positron plasma; halting this process. This can affect the rate at which antihydrogen is formed and lower the average binding energy. Detailed simulations of antihydrogen formation that take this effect into account were able to roughly reproduce results of ATHENA and ATRAP [110].

5.1.2 Trappable antihydrogen

After formation, an antihydrogen atom is considered trappable if it is in a low-field seeking state and has low enough kinetic energy ($< 0.5\ \mathrm{K}\times k_\mathrm{B}$) that it cannot escape the magnetic trap (see Sec. 2.4). Naively, it would be expected that half of all antihydrogen atoms produced will be in a low-field seeking state. However, in a strong magnetic field the unbound positron has a tight cyclotron orbit relative to the orbit of a positron bound to an antiproton. In order for a low-field seeking atom (with negative $\mu \cdot \vec{B}$) to be formed, the cyclotron orbit of the approaching positron must overlap the antiproton [108]. Therefore, the fraction of low-field seeking atoms formed can be roughly estimated as the ratio of the area of the cyclotron motion to the area of the bound positron orbit. For example, a positron in a plasma at 4 K in a 1 T field will have a cyclotron radius of ∼60 nm while a bound positron in an $n = 70$ (corresponding to a binding energy of ∼32 K) state has a radius of ∼260 nm. The fraction of low-field seeking states would therefore be expected to only be $(60/260)^2 = 0.05$. As the positron temperature increases, the cyclotron radius approaches the bound positron orbit and the fraction of low-field seeking states will approach 0.5.

Because of the large antiproton to positron mass difference, the initial kinetic energy of the antihydrogen atoms will be dominated by the kinetic energy of the antiprotons. When antiprotons and positrons are brought together, however, collisions between the two species can bring them into thermal equilibrium before the majority of antihydrogen atoms are formed [111]. It is therefore critical to minimize not only the pre-mixing antiproton temperature but that of the positron plasma as well. In addition to the thermal energy, the antiprotons also rotate about the trap axis with the positron plasma. At equilibrium, the antiprotons rotate with the positrons at a frequency given by Eq. 3.13 and a velocity

$$v_r = \omega_r r = \frac{n_{e^+} q r}{2\epsilon_0 B}, \tag{5.7}$$

where n_{e^+} is the positron density, r is the radial position of the antiproton and B is the magnetic field strength. By minimizing the radial extent of the antiproton plasma, the number of antihydrogen atoms formed close to the trap axis ($r = 0$) will be maximized. The n_{e^+} dependence of Eq. 5.7 suggests that reducing the positron density will increase the number of trappable antihydrogen atoms, however this density also enters into the formation rates for radiative recombination (Eq. 5.3) and three-body recombination (Eq. 5.6). For typical positron temperatures in ALPHA (40 - 100 K), Eq. 5.7 does not contribute significantly to the overall antiproton kinetic energy. For example, an antiproton at $r = 1$ mm in a positron plasma with $n_{e^+} = 10^{13}$ m^{-3} will have a rotational velocity $v_r = 633$ m/s, which is roughly equal to the thermal velocity of a 15 K distribution. The optimal positron density for forming trappable

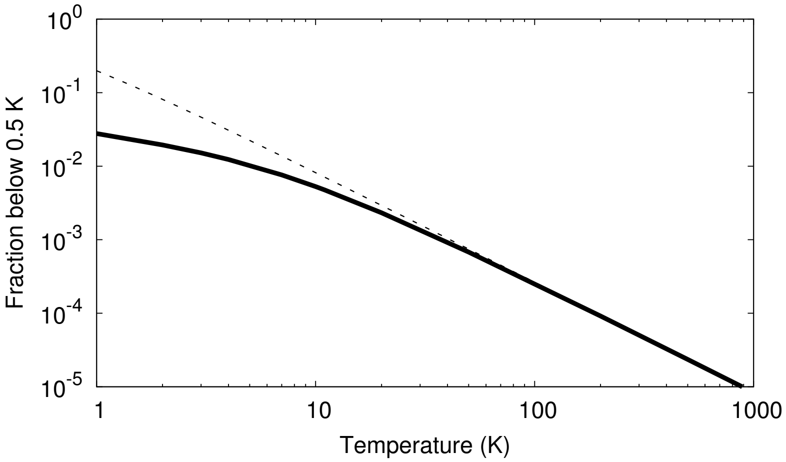

Figure 5.1: Fraction of antihydrogen atoms formed with a kinetic energy less than $0.5\times k_{\mathrm{B}}$ (solid line) as a function of formation temperature. The fraction is numerically calculated assuming a uniform positron density of 5×10^7 up to a radius of 1 mm. The dashed line represents the fraction if the rotational energy is ignored. The kinetic energy of the atom is dominated by the thermal energy of the positrons above ∼50 K.

antihydrogen remains an open question.

Assuming a uniform density plasma with a radius of 1 mm, the fraction of antihydrogen atoms that have a kinetic energy less than 0.5 $\mathrm{K}\times k_{\mathrm{B}}$ is shown in Fig. 5.1. In the most optimistic case, where antihydrogen is formed at ∼4 K (i.e. the temperature of liquid helium) and 50% of the atoms are low-field seekers, the trappable fraction is only 0.006. If a total of 1×10^4 antihydrogen atoms are produced in a mixing cycle, this amounts to 60 trappable atoms. In a more realistic scenario, taking a typical positron temperature of 40 K, up to roughly 5 trappable atoms are expected. It should be noted that this is a rough estimate at best as there are many details of the formation that are not fully understood at this time. The small number of trappable antihydrogen atoms expected further emphasizes the importance of optimizing the antihydrogen production and detection techniques.

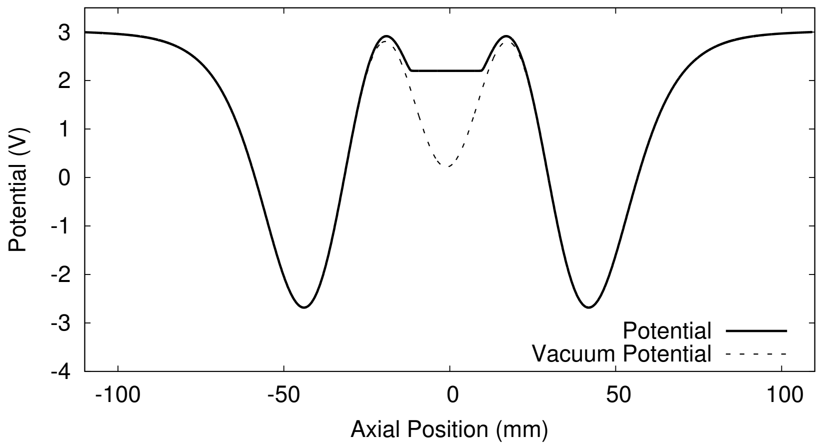

Figure 5.2: A plot of the on-axis potential of the nested well configuration. The solid curve shows an example of the full potential when a positron plasma is placed in the central well. The dashed line indicates the potential in the absence of any plasmas.

5.1.3 Autoresonant Mixing

Antiprotons and positrons have opposite charges so bringing them together is not as simple as moving each plasma longitudinally with potential manipulations. In order to confine both species simultaneously, a nested well potential (Fig. 5.2) is constructed [106]. One species is trapped in the central well while the other will be confined by the larger, inverted, well. Initially, one of these species is confined in one of the side wells shown in Fig. 5.2 and then its longitudinal energy is excited in some manner such that it has sufficient energy to overlap with the central plasma. Because their mass is much larger it might be expected that keeping the antiprotons at rest in the central well and exciting the positrons would be the optimal configuration. However, positrons cool quickly in a strong magnetic field ($\tau_c \sim 4$ s at 1 T) so they would only interact with the antiprotons for a short time before losing energy and cooling into the side wells; stopping the reaction. For this reason, the positrons are placed in the central well and the antiprotons are injected into them.

The simplest mixing method is to release the antiprotons from a higher potential

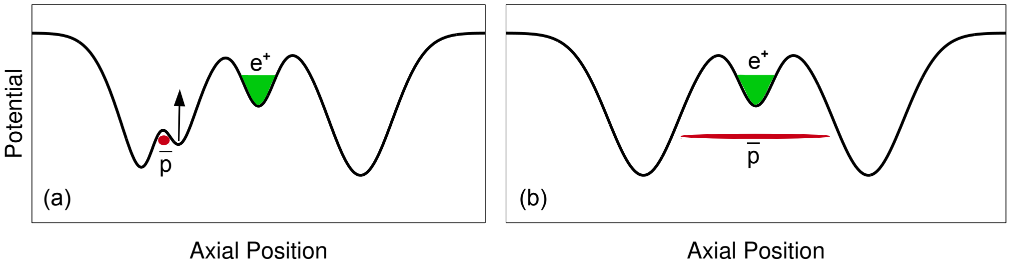

Figure 5.3: A sketch of antiprotons (red) being injected into the positron plasma (green) by releasing them from a higher potential well. (a) One side of the antiproton confining well is removed, releasing the antiprotons into the larger nested well (b) where they will interact with the positron plasma confined in the middle.

into the nested well, as pictured in Fig. 5.3. This method was used effectively by the ATHENA and ATRAP collaborations to produce the first 'cold' antihydrogen [4, 32]. Antiprotons injected in this manner, however, have many electron-volts of excess kinetic energy and are thus not suitable for forming trappable antihydrogen atoms. The positrons and antiprotons can be mixed more 'gently' by using a technique known as 'incremental mixing' [38]. In this scheme, the antiprotons start in the side-well next to the positron plasma (see Fig. 5.4). The potential barrier between the antiproton and positron wells is then slowly (with respect to the bounce time of the antiprotons) reduced until the antiprotons can escape the side-well and mix with the positrons. Incremental mixing is a large improvement over the simple injection procedure used by ATHENA but still results in antiprotons which are too energetic to form trappable antihydrogen.

To inject antiprotons into the positron plasma with minimal excess kinetic energy, ALPHA developed a new technique known as 'autoresonant injection'. Autoresonance is a general phenomena that can occur when a non-linear oscillator is subject to a drive with a swept frequency. To illustrate this effect, consider a simple pendulum. In the limit of small oscillations the pendulum behaves as a linear oscillator, with a frequency

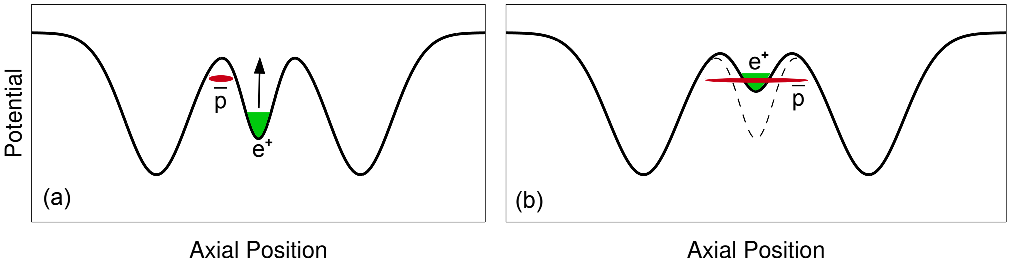

Figure 5.4: A sketch of the incremental mixing scheme. (a) The antiprotons (red) are initially confined in the side well at a well defined longitudinal energy. In (b), the central potential has been raised until the antiprotons can overcome the potential barrier and enter the positron plasma. The initial vacuum potential is indicated by the dashed line.

independent of amplitude. At high amplitudes, however, the pendulum's oscillation frequency is a monotonic function of the oscillation amplitude. If the pendulum is driven at a fixed frequency, its amplitude will grow briefly but its frequency will also change, causing the pendulum to go out of phase with the drive. Instead, if a variable frequency drive that slowly sweeps through the resonance is applied, the pendulum will phase lock to the drive and its frequency will follow that of the drive. This phenomenon is known as autoresonance.

Autoresonance occurs in a variety of systems and applications including plasma modes [112], planetary dynamics [113], atomic physics [114], and Bose-Einstein condensates [115]. For the purposes of mixing, the oscillator considered here is the centre-of-mass (COM) motion (see Sec. 3.4) of the antiproton plasma in the axial potential well. This motion is excited by applying a radio-frequency drive to an electrode near the confining well. The drive frequency starts above the COM frequency and sweeps through resonance to some final frequency. The COM oscillation will autoresonantly lock to the drive, allowing the final energy of the oscillator to be controlled by setting the final drive frequency.

A swept frequency drive starting at a frequency 2.5% above the COM resonance

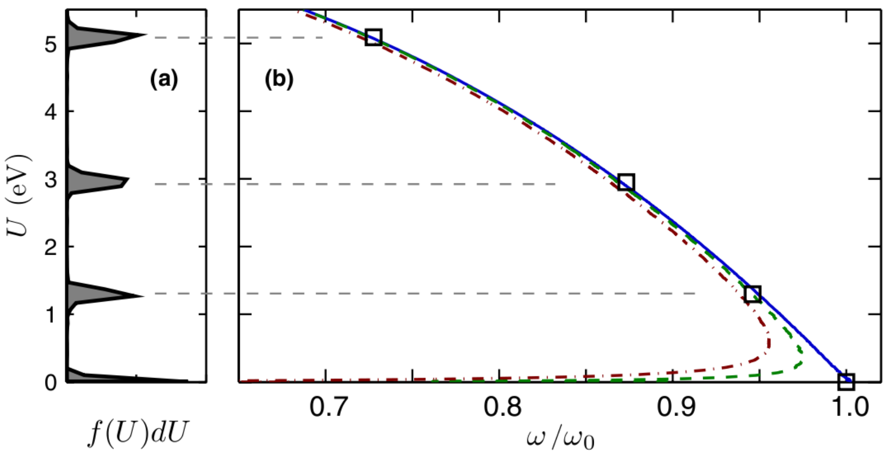

Figure 5.5: (a) Longitudinal energy distribution of ∼15000 antiprotons after autoresonant excitation with various stopping frequencies. (b) A plot of the measured mean longitudinal energy (open squares) as a function of final drive frequency. The calculated longitudinal energy as a function of drive frequency is shown for the vacuum potential (solid blue), 15000 antiprotons (dashed green), and 50000 antiprotons (dot–dashed red). All frequencies are normalized to $\omega_0 = 2\pi \times 410$ kHz. (Reproduced with permission from [51])

and sweeping to various final frequencies was applied to plasmas of 15000 and 50000 antiprotons. The final energy distributions were measured by releasing the plasmas onto the degrader and counting the resulting annihilations with the scintillators. The result of these experiments is illustrated in Fig. 5.5. Good agreement between the mean energy of each distribution and the calculated COM frequency was observed, demonstrating the autoresonant control of the longitudinal energy. More details can be found in reference [51].

With autoresonance, it is possible to controllably excite the antiprotons from a side-well in the nested configuration into the positron plasma. This method raises the mean longitudinal energy without increasing the longitudinal and transverse temperatures. Compared to incremental mixing, much narrower longitudinal energy distributions are produced. A beneficial feature of autoresonance in the nested well is that the COM frequency undergoes a sharp discontinuity when the antiprotons have enough energy to escape the side well. When they escape, the antiproton's bounce length is suddenly much longer, dropping the oscillation frequency correspondingly. At this point, the antiprotons will suddenly be far out of resonance with the drive and stop gaining energy coherently. Even if the autoresonant drive continues briefly after injection, significant heating of the antiprotons will not occur.

5.1.4 Detection of untrapped antihydrogen

The majority of antihydrogen produced will escape the neutral atom trap and annihilate on the electrode walls due to their spin states and/or high thermal energy. In ATHENA, these annihilations were identified by looking for coincident antiproton and positron annihilations. However, this detection method suffered from the low detection efficiency (20%) of the 511 keV photons from the positron-electron annihilations [4]. As a result, only 0.2% of the antihydrogen annihilations were identified by the detector. Further characterization of the antiproton annihilations, however, revealed that nearly all could be attributed to antihydrogen [116]. It was observed that antiprotons from antihydrogen annihilations tend to annihilate on the electrode walls with no angular dependence. Bare antiprotons, on the other hand, are strongly influenced by the Penning trap electric and magnetic fields and tend to annihilate in localized 'hot spots'.

Based on the results of these studies, the ALPHA experiment was designed to distinguish antihydrogen using the spatial distributions of the annihilations measured with a three-layer silicon detector described in Sec. 2.6.5. Figure 5.6(a) shows an example of the x-y position distribution of reconstructed antihydrogen annihilation vertices. The majority of the annihilations occur in a uniform ring corresponding to the inner electrode surface. A pure antiproton distribution can be generated by intentionally destabilizing an antiproton plasma, causing the the antiprotons to annihilate on the electrodes. Figure 5.6(b) shows the resulting hot spots that are observed.

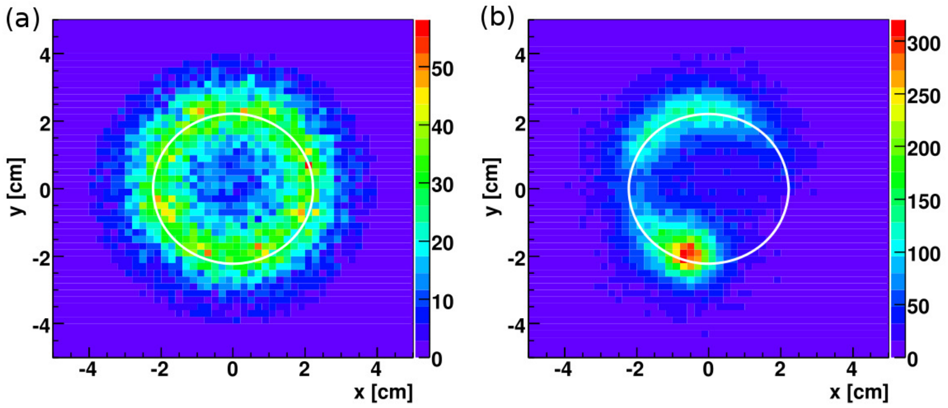

Figure 5.6: (a) A contour plot showing an example distribution of antihydrogen annihilations projected along the Penning trap axis. The vertices are concentrated around the electrode walls as indicated by the white circle. In contrast, (b) bare antiprotons tend annihilate in highly localized hot spots. (Adapted with permission from [78])

The locations of these spots are likely set by deviations from the ideal cylindrical symmetry of the Penning trap due to manufacturing and construction imperfections. The spatial distribution of the annihilations is used to identify that antihydrogen was produced as well as providing information about the antihydrogen binding energy and temperature distributions [76].

5.2 Trapping Antihydrogen

With all the tools in place to bring cold antiproton and positron plasmas together with as little energy as possible and to analyse the results, an attempt to trap antihydrogen can be made. Even under optimal conditions, the fraction of trappable antihydrogen atoms will be small. ALPHA's strategy is to maximize the detection of rare trapped antihydrogen events and to perform many trapping 'attempts' interspersed with control measurements. In this context a trapping attempt is a cycle of plasma preparation, mixing, and search for the signal of trapped antihydrogen.

For example, each trapping attempt in the 2010 trapping experiment (see Sec. 5.2.4) consisted of the following steps:

1. Positrons are accumulated in the positron accumulator for ∼200 s.
2. The inner solenoid is energized and antiprotons are caught in the 3 T field. Roughly 3×10^4 antiprotons are caught and electron-cooled for 80 s (Sec. 4.1).
3. Roughly 1×10^7 positrons are transferred to the positron trap region (see Sec. 2.3.2) of the ALPHA Penning trap.
4. The positron and antiproton-electron plasmas are compressed using the rotating wall technique (Sec. 4.2).
5. The inner solenoid is de-energized and the plasmas are moved to the mixing region of the trap where the electrons are removed (Sec. 4.4) and the nested well is formed. The antiproton cloud is 200 K at this stage and has a radius of 0.8 mm and a density of 6.5×10^{12} m^{-3}.
6. The neutral atom trap magnets (Sec. 2.4.2) are energized over 25 s.
7. The positron plasma is evaporatively cooled to ∼40 K (Sec. 4.4). The final plasma consists of 2×10^6 positrons and has a radius of 0.9 mm and a density of 5.5×10^{13} m^{-3}.
8. The antiprotons are autoresonantly injected into the positron plasma (Sec. 5.1.3) and left to mix for 1 s.
9. Any remaining charged particles are cleared from the trap by a series of applied electric fields of up to 500 V/m.

10. The trap magnets are rapidly turned off, releasing any trapped antihydrogen atoms. The signal window for detecting the annihilation of previously trapped atoms is 30 ms (Sec. 5.2.1).

5.2.1 Identification of Trapped Antihydrogen

Trapped antihydrogen is detected by turning off the neutral atom trap magnets and looking for annihilations of previously trapped antihydrogen atoms with the silicon vertex detector (Sec. 2.6.5). Readout of the detector is triggered when at least two hits are registered on the inner layer. Each readout is known as an 'event'. This trigger is designed to accept as many annihilations as possible but is also sensitive to electronic noise and the passage of cosmic ray particles. These 'background' events can be mistaken for annihilations and reduce the ability to identify antihydrogen annihilations after the trap shutdown.

For the purposes of this discussion, 'signal' refers to events that result from annihilations and 'background' refers to any other type of event that is misidentified as an annihilation. For each of the triggered events, the reconstruction algorithm attempts to find an annihilation vertex. Loosely, this requires at least two sets of three hits that form at least two tracks, which are then used to find the annihilation vertex. A full discussion of this algorithm is beyond the scope of this thesis and can be found in references [79] and [80, 81]. The requirement that an event produce a vertex to be considered an annihilation largely eliminates events due to electronic noise. The remaining background events are primarily due to cosmic ray particles passing through the detector. Cosmic rays are high energy particles that originate from sources outside the Earth's atmosphere. Through collisions with particles in the atmosphere, they can produce showers of secondary particles that reach the surface of the Earth. The majority of the particles that reach the surface are muons with a mean energy of roughly 4 GeV [17]. Based on the horizontal area of the ALPHA detector, a cosmic trigger rate of 11 s^{-1} is expected [17], consistent with the observed rate of 9.65 ± 0.02 s^{-1}. Fortunately, the vast majority of these cosmic events can be distinguished from annihilations based on the topology of the event.

Cosmic events are distinguished from annihilations by examining the following event characteristics: number of tracks, vertex position, and the sum of squared residuals. The distribution of these variables can be used to determine a set of selection criteria or 'cuts' that must be passed in order for an event to be characterized as an annihilation. Representative datasets are used to determine the optimal cuts independent of the trapping experiment to avoid experimenter bias. The data from the trapping experiment was only analyzed after the optimal set of cuts was finalized. A set of annihilation events is constructed from 335 cycles of positron and antiproton mixing in the neutral atom trap field. Of the 165520 total recorded events, the majority are due to antihydrogen annihilations with only about 3350 contaminating cosmic events expected. The background sample was collected with the neutral atom trap energized, but no antiparticles present. A total of 109824 events were collected which should all be due to background sources such as electronic noise and cosmic ray particles.

5.2.1.1 Number of tracks

The majority of cosmic ray events that produce a vertex look like the example event in Fig. 5.7a, where a muon passed through the detector in a straight line resulting in two reconstructed tracks. Antiproton annihilation events, on the other hand, often contain more than two tracks as in Fig. 5.7b. Figure 5.8a shows a histogram of the number of tracks in the background and signal sample sets.

5.2.1.2 Vertex position

Another distinguishing feature is the radial position of the reconstructed vertex. Annihilations will occur primarily on the electrode wall, so the reconstructed vertex

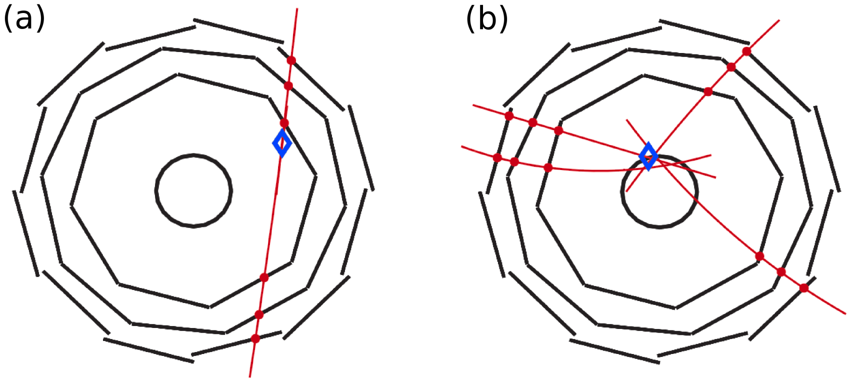

Figure 5.7: (a) Cross-section of a typical cosmic event. A muon passing straight through the detector results in two sets of three heats, which each produce a track. The reconstructed vertex can effectively lie anywhere within the detector volume. (b) Cross-section of an antiproton annihilation event. In contrast to cosmic events, antiproton annihilations often produce more than two tracks and the vertices are concentrated around the radial position of the electrodes.

position is expected to be within the detector resolution (0.87 cm) of the wall. The vertices produced by cosmic ray events, however, are not constrained to the trap wall. The distribution of the vertex radius for signal and background samples is plotted in Fig. 5.8b.

5.2.1.3 Sum of squared residuals

Finally, the 'straightness' of the events can be used to distinguish cosmics from annihilations. The majority of cosmic rays are expected to pass straight through the detector. A straight line is fit to the six hits that form a pair of tracks. The 'straightness' is quantified by the sum of the square residuals (distances from the hit positions to the straight line fit). For events with more than two tracks, a fit is performed on each pair of tracks and the minimum sum of square residuals is taken. Straight cosmic trajectories through the detector will result in a very small sum of square residuals. Annihilations, however, are not expected to produce many co-linear tracks. The treatment of the residuals is split into two cases: events with exactly two tracks and those with greater than two tracks. A significant fraction of the two track events are

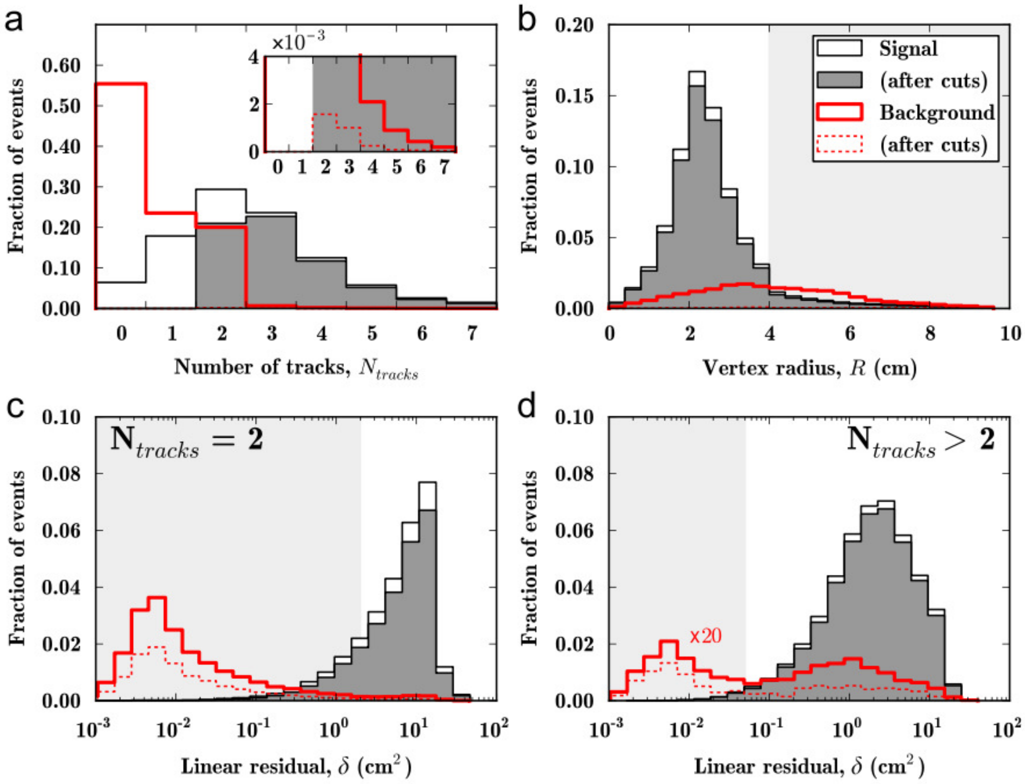

Figure 5.8: Measured distributions of the distinguishing variables from the sample datasets. Plotted are (a) the fraction of events with a given number of tracks, (b) the distribution of vertex radial positions and the sum of residuals squared (linear residual) for (c) $N_{Tracks} = 2$ and (d) $N_{Tracks} > 2$. The distributions are normalized to the number of events in each data set. The solid black trace indicates the signal sample and the thick red trace indicates the cosmic background sample. The shaded regions of the plots represent the values rejected by the cuts. After cuts the fraction of remaining signal events is represented by the filled grey trace and the remaining background events by the dashed red trace. The inset in (a) shows the effect of the cuts on the background sample distribution. In (d), the background traces have been magnified by a factor of 20 to compare the distribution of events to the signal sample. (Reproduced with permission from [79])

N_{Tracks}	Vertex Radius (cm)	Sum of square residuals (cm^2)
$= 2$	< 4	> 2
> 2	< 4	> 0.05

Table 5.1: Final set of parameter cuts. Events that satisfy these criteria are classified as annihilations.

expected to be cosmics while those with greater than two tracks will be dominated by annihilations. Figures 5.8c and 5.8d show the distributions of linear residuals for two track and greater than two track events, respectively.

5.2.1.4 Cut optimization

The placement of the cuts must balance the rejection of cosmic events with the desire to accept as many valid annihilation events as possible. This was done by optimizing the expected signal significance during attempts to trap antihydrogen. A figure of merit for the optimization is the probability of observing N or more events solely due to a Poisson-distributed background with mean b, known as the p-value. A full description of the cut placement procedure is described in [79] and the resulting final set of cuts are shown in Table 5.1. With these cuts, 99.6% of background events are rejected while retaining an overall detection efficiency of 47% for annihilations. The rate that a background event is accepted as an annihilation is measured to be only $4.6 \pm 0.1 \times 10^{-2}$ s^{-1}. Because the neutral atom trap magnets are capable of shutting off quickly (see Sec. 2.4.2), a window of only 30 ms after shutdown is monitored for antihydrogen annihilations. This means that only 1 background event would be expected to pass the cuts in roughly 700 trapping attempts.

5.2.2 Mirror Trapped Antiprotons

The ability to distinguish annihilations has been established but there remains a possibility that the annihilations are due to trapped bare antiprotons rather than trapped antihydrogen. While a series of clearing electric fields are applied to clear out all of the charged particles remaining after mixing, there is a possibility that some antiprotons can remain trapped by a mechanism known as 'mirror trapping'. This trapping is a consequence of the adiabatic conservation of the magnetic moment of a gyrating particle [117], $\mu = E_\perp/B$, where $E_\perp$ is the kinetic energy transverse to the magnetic field of magnitude B. An antiproton moving parallel to the magnetic field of the neutral atom trap will see an axially increasing field due to the mirror coils. From the conservation of μ the parallel speed,$v_{||}$, of the antiproton in this field can be written as

$$v_{||}^2 = v_0^2 \left(1 - \frac{v_{\perp,0}^2}{v_0^2}\frac{B}{B_0}\right), \tag{5.8}$$

where $v_0 = \sqrt{v_{||,0}^2 + v_{\perp,0}^2}$ and $v_{\perp,0}$ are the speed and perpendicular component of the speed, respectively, at the minimum magnetic field B_0. For sufficiently high B/B_0 or $v_{\perp,0}/v_0$, the antiproton reaches a turning point ($v_{||} = 0$) and is reflected. Mirror trapped antiprotons are a particularly tricky background source and must be considered carefully.

A series of four 'clearing' pulses are applied after mixing to remove all remaining positrons and antiprotons from the trap. The pulses alternate in polarity and each has an average electric field strength of 2.5 V/cm. In order to survive these pulses, an antiproton requires a large amount of perpendicular energy such that the electric potential doesn't overcome the effective magnetic mirror trapping potential. This can be examined by writing a combined pseudopotential

$$U = E_{\perp,0}\left(\frac{B - B_0}{B_0}\right) - e\Phi, \tag{5.9}$$

where $E_{\perp,0}$ is the minimum transverse kinetic energy, e is the fundamental charge, and Φ is the electric potential. The on-axis magnetic field and electric potential during a clearing pulse are shown in Fig. 5.9a and the resulting psuedopotentials for different $E_{\perp,0}$ are shown in Fig. 5.9b. For the fields used in ALPHA, a psuedopotential well will exist for particles with $E_{\perp,0} > 24.4$ eV [118]. Even those particles may not

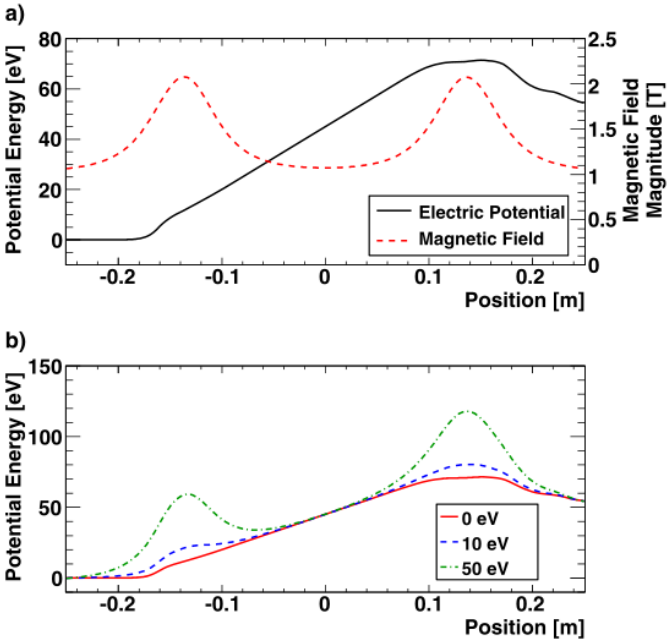

Figure 5.9: (a) The electric potential energy and magnetic field strength as a function of axial position. (b) The total potential energy as a function of position for antiprotons with various $E_{\perp,0}$. (Reproduced with permission from [78])

remain trapped, however, as the clearing potentials alternate in polarity multiple times. Extensive simulations show that all antiprotons with $E_{\perp} < 50$ eV will be expelled after the full set of clearing pulses [118]. Potential sources of antiprotons with such high transverse kinetic energies are considered in [118]. Creation of high $E_{\perp}$ antiprotons by mechanisms involved in antiproton catching, antiproton and positron mixing, and ionization of antihydrogen were considered. None of these mechanisms were deemed plausible sources of antiprotons with $E_{\perp,0} > 50$ eV.

However unlikely mirror trapped antiprotons may be, they must still be experimentally distinguishable from antihydrogen in order to demonstrate antihydrogen trapping. While the structure of the annihilation events will be the same, the annihilation positions can be used as a distinguishing parameter. This is achieved by studying the dynamics of neutral antihydrogen atoms as compared to charged antiprotons as the magnetic trap is shutdown. One of the major difference between the species are their kinetic energies. Trapped antihydrogen atoms must have energies below 5×10^{-5} eV while mirror trapped antiprotons necessarily have energies above 50 eV. The high speeds of the antiprotons mean they will quickly find the point where the trap depth is at a minimum as the magnetic trap turns off. In the ALPHA magnetic trap, this tends to concentrate their annihilations around the axial centre of the trap. Antihydrogen atoms, on the other hand, are slow relative to the decay of the magnetic field and tend to escape in a wide spatial distribution. The trajectories of antihydrogen atoms and antiprotons are simulated in detail through the clearing pulses and magnet shutdown. Classical force equations propagate the particles through the apparatus subject to accurately modelled electric and magnetic fields. From these simulations, the distribution of annihilation positions and times can be calculated for each species and, with the right control measurements, used to distinguish antihydrogen from mirror-trapped antiprotons. A full treatment of the simulations and the discrimination of antihydrogen from mirror trapped antiprotons can be found in Ref. [118].

5.2.3 Control Measurements

Antihydrogen trapping is demonstrated by performing many trapping attempts and comparing the results against control measurements. These controls are designed to demonstrate that any detected events are antihydrogen annihilations and not the result of background sources.

5.2.3.1 Heated Positrons

As a primary control experiment, the positron plasma is heated to 1100 K before mixing. This is accomplished using a radio-frequency drive to excite the axial motion of the positrons. Heating the positrons has two effects: antihydrogen formation is strongly suppressed because of the temperature dependence of the formation mechanisms (see Sec. 5.1.1), and any antihydrogen that is formed will be done so near the positron temperature, making it very unlikely to be trapped. Aside from the positron heating, this control experiment is identical to the trapping experiment. Any annihilation events (those passing the cuts in Sec. 5.2.1) detected during the trap shutdown are taken to be the experimental background.

5.2.3.2 Electric Fields During Trap Shutdown

As discussed in Sec. 5.2.2, mirror trapped antiprotons and antihydrogen atoms will follow different trajectories, and annihilate in different positions, during trap shutdown. The trajectories of any potential mirror trapped antiprotons can also be influenced by applying 'bias' electric fields during the shutdown. The bias field will shift the annihilation positions of the charged antiprotons to the left or right (depending on the field applied) while neutral antihydrogen annihilations will be unaffected.

To this end, three variations of the trapping experiment were carried out: The first had no bias field applied during shutdown, in the second a 'left bias' field is applied to deflect the antiprotons to the left (negative z), and in the third variation a 'right bias' field is applied. The bias electric fields generated by the Penning trap electrodes are roughly 500 V/m in magnitude. The effects of these fields were tested in a series of experiments that intentionally generated mirror trapped antiprotons through extreme potential manipulations [118]. The results of these tests are shown in Fig. 5.10a. The annihilation positions of the mirror trapped antiprotons are shifted as expected. These experiments also serve as validation of the simulations. The simulations were further validated by delaying the start of the octupole magnet shutdown by 7 ms with respect to the mirror coil shutdown. As seen in Fig. 5.10b, there is again good agreement between simulation and experiment.

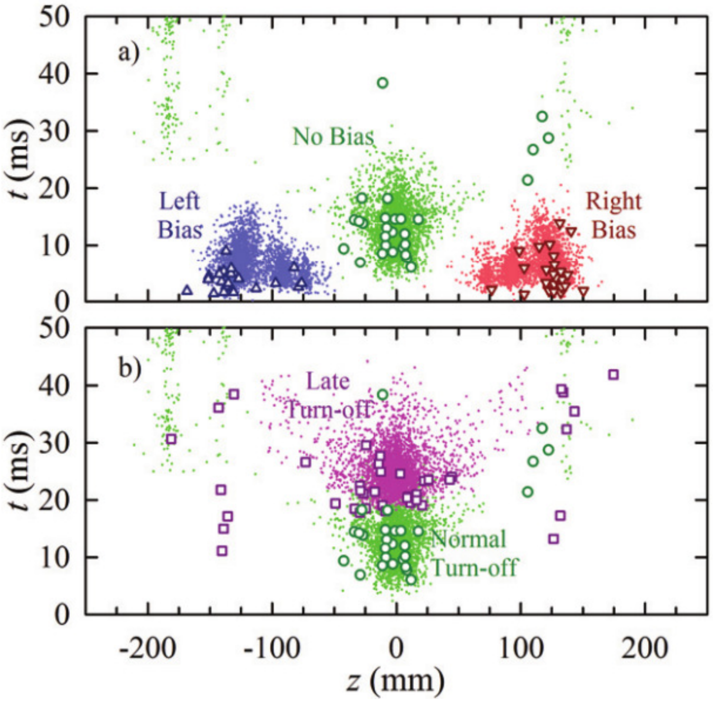

Figure 5.10: The time and axial position distribution of mirror-trapped antiproton annihilations (symbols) compared to simulated mirror trapped antiprotons (dots). (a) Comparison of the distributions under the influence of the left (blue), right (red) and no bias (green) fields. (b) Comparison of the distribution without a bias field when the octupole magnet shutdown is delayed by 7 ms relative to the mirror coils (purple) with the normal shutdown (green). (Reproduced with permission from [118])

5.2.4 Results

In 2009, the first systematic attempt to trap antihydrogen was conducted [78]. A total of 212 trapping attempts (similar to the 2010 trapping sequence outlined above) were performed with 4.5×10^4 antiprotons at ~350 K and 2.2×10^6 e^+ at ~70 K. In total, six events were observed during the magnet shutdown window that satisfied the annihilation selection criteria (Sec. 5.2.1). The probability that these six events were due to cosmic background is 9.2×10^{-9}, corresponding to a significance of 5.6 standard deviations. This experiment, however, did not include the bias electric field or positron heating control measurements necessary to definitively rule out the possibility these events were due to mirror trapped antiprotons.

The following year (2010), an improved attempt to trap antihydrogen was made with colder plasmas and extensive control measurements [5]. Evaporative cooling of positrons brought their temperature down to 40 K and the antiproton manipulations were tuned to bring their temperature down to 200 K (evaporative cooling of antiprotons was not used). After antiprotons and positrons were mixed for 1 s, potentially trapped antihydrogen atoms were held for 172 ms before the magnetic trap was shutdown. A total of 335 trapping attempts were made, consisting of: 137 cycles with no bias field applied during shutdown, 101 with a left bias field, and 97 with a right bias field. In addition, a series of 246 experiments were performed with positrons heated to 1100 K. These 246 experiments were also split between the left bias (60), right bias (54), and no bias (132) variations. The total number of observed annihilation events for each type of experiment are compiled in Table 5.2. A total of 38 annihilations were observed in the trapping experiments, compared to a single annihilation in the control experiments. Scaling this one annihilation in 246 attempts to 335 attempts gives a measured background of 1.4 ± 1.4 events.

The time and position of the 38 annihilations were compared with the simulated

Attempt type	Number of attempts	Annihilation events
No bias	137	15
Left bias	101	11
Right bias	97	12
No bias, heated positrons	132	1
Left bias, heated positrons	60	0
Right bias, heated positrons	54	0

Table 5.2: A summary of 2010 trapping experiment results.

annihilation distribution of antihydrogen (Fig 5.11a) and mirror-trapped antiprotons (Fig. 5.11b). It is clear that the measured annihilation distributions are not consistent with the predictions for mirror-trapped antiprotons. On the other hand, there is a good agreement between the measured distribution with the predictions for neutral antihydrogen. Because the 38 annihilations are inconsistent with both mirror-trapped antiprotons and a fluctuation of the measured background, it was concluded that ALPHA observed the release of antihydrogen atoms that were magnetically trapped for at least 172 ms.[1]

5.2.5 Lifetime

This initial demonstration of antihydrogen trapping only held the atoms for 172 ms, the minimum length of time to complete all necessary operations before trap shutdown. This maximized the probability of detecting trapped antihydrogen atoms before they could be lost. Following this work, the next obvious question was: what is the lifetime of trapped antihydrogen? Magnetic traps for hydrogen atoms have been able to achieve trapping times over 20 minutes [119], however antihydrogen can also be lost by annihilating on background gas molecules. Furthermore, there are mechanisms that may result in ‘quasi-stable’ orbits of the antihydrogen atoms that may only remain trapped for a few hundred milliseconds [120].

---

[1] As the antiprotons and positrons were mixed for 1 s before the 172 ms window, antihydrogen atoms were trapped for between 0.172 s and 1.172 s.

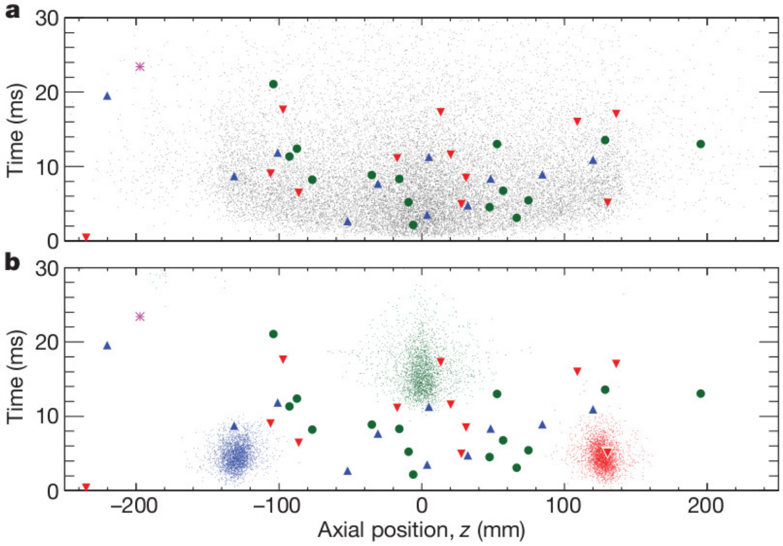

Figure 5.11: The measured z-t distribution of annihilation events with no bias field (green circles), left bias (blue triangles), and right bias (red triangles). The single annihilation observed during the attempts with heated positrons is shown as a violet star. In (a), the grey dots are simulated annihilations of neutral antihydrogen atoms released from the trap. In (b), the simulated annihilation positions for mirror-trapped antiprotons subject to a left bias field (blue dots), right bias field (red dots), and no bias field (green dots) are shown.

Before undertaking a systematic study of the lifetime of trapped antihydrogen, each step of the trapping experiment was optimized to improve the number of trapped atoms per attempt. The most significant of these optimizations were the use of evaporative cooling of antiprotons to reduce the antiproton temperature to ∼100 K and the further optimization of autoresonant mixing. In addition, the vertex reconstruction algorithms were improved to give an overall annihilation detection efficiency of $57 \pm 6\%$. These optimizations brought the number of trapped antihydrogen atoms detected per attempt from 0.11 up to 0.64.

Just before autoresonant mixing, the antiproton plasma had a radius of 0.4 mm, a density of 7×10^{13} m^{-3}, and consisted of 1.5×10^{4} antiprotons. The positron plasma had a radius of 0.8 mm, a density of 5×10^{13} m^{-3}, and a temperature of ∼40 K. Antiprotons were autoresonantly injected into the positron plasma and allowed to mix for 1 s before the standard clearing fields were applied. A variable confinement time was then imposed before the trap shutdown was initiated. A static electric bias field was applied during confinement and trap shutdown to deflect any mirror-trapped antiprotons that may have been present. A total of 201 trapping attempts were performed with confinement times (between the end of mixing and trap shutdown) between 0.4 s and 2000 s. The results are summarized in Table 5.3. The time and position distribution of the 112 observed annihilations agrees well the simulated neutral antihydrogen distribution and are inconsistent with mirror trapped antiprotons (Fig. 5.12). The probability that a statistical fluctuation of the cosmic ray background ($1.4 \pm 0.1 \times 10^{-3}$ counts/attempt [52]) could produce the observed number of events was evaluated for each confinement time. At 1000 s this probability is less than 10^{-15}; a statistical significance of 8 standard deviations. Thus it was concluded that antihydrogen atoms had been trapped for at least 1000 s (over 15 minutes).

Confinement time (s)	# of attempts	Annihilations detected	Significance (σ)
0.4	119	76	28
10.4	6	6	8.0
50.4	13	4	5.7
180	32	14	11
600	12	4	5.8
1000	16	7	8.0
2000	3	1	2.6

Table 5.3: Summary of antihydrogen lifetime measurements.

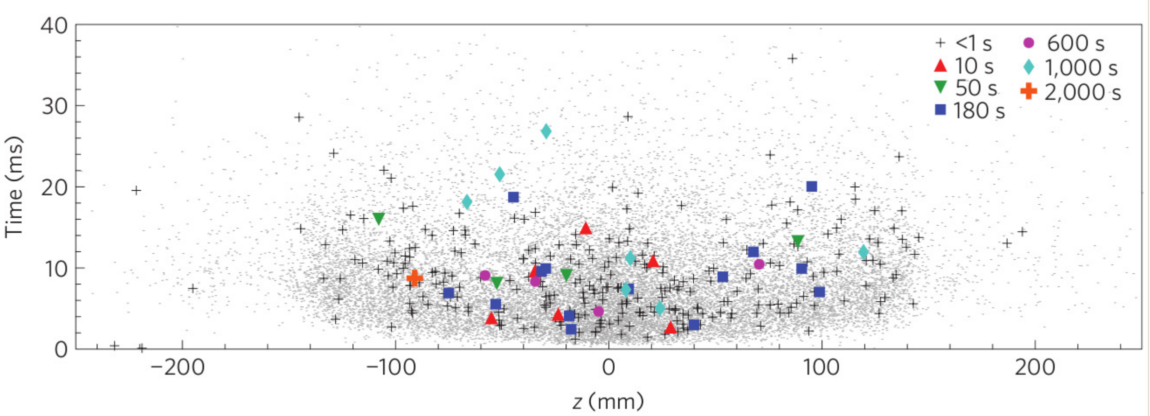

Figure 5.12: The time and axial position distribution of the antihydrogen annihilations after magnetic trap shutdown for different confinement times. The grey dots are simulated antihydrogen annihilation positions for comparison. (Adapted with permission from [52])

5.2.6 Conclusions

The work described in this chapter represents the first demonstration of the trapping of antihydrogen (or any pure antimatter atomic system). In 2012 the ATRAP collaboration similarly reported the trapping of a total of 105 ± 21 antihydrogen atoms [121]. An average of 5 ± 1 antihydrogen atoms were trapped in each attempt, roughly a factor of 5 higher than achieved by ALPHA[2] It is important to note, however, that compared to the ALPHA experiment each trapping attempt used of a factor of 30 times more antiprotons and took a factor of 13 times longer.

---

[2] Correcting for the annihilation detection efficiency, ALPHA traps roughly 1.1 antihydrogen atom per attempt.

Chapter 6

Non-destructive Measurements of Plasma Heating

The ability to trap antihydrogen atoms for long periods of time opens up the possibility of spectroscopic studies of those atoms. The most attractive atomic transitions for study are the 1S - 2S laser transition and the ground state hyperfine transitions at microwave frequencies. Unfortunately, the ALPHA-1 apparatus does not include optical access for laser spectroscopy of antihydrogen. There are, however, two ground state hyperfine transitions that can be induced by microwave fields, which can be injected and propagate within the ALPHA Penning trap. In a strong magnetic field these two transitions correspond to a flip of the positron spin and occur at roughly 28 GHz (see Chapter 8 for more detail). Addressing these transitions is still a challenge, however, as the ALPHA-1 apparatus was not designed for microwave experiments.

One of the biggest issues is that the Penning trap electrode stack supports a complex set of microwave standing and travelling wave modes. This is due to the gaps between electrodes and various internal surfaces that can reflect microwaves, including multiple changes in electrode radius. This environment results in microwave fields that vary drastically as a function of both position within the Penning trap and the frequency of the field. Without a method to measure the microwave field it is unknown whether any microwave power at the relevant frequencies will reach the trapped antihydrogen atoms.

Another issue when considering hyperfine spectroscopy of antihydrogen is that the positron spin resonance transition frequency strongly depends on the magnetic field strength. In order to set the microwave frequency correctly, and maximize the transition probability, accurate measurements of the magnetic field are required. This is complicated by the fact that the magnetic field of the neutral atom trap is highly inhomogeneous in nature. To hit the positron spin resonance transition frequency, one therefore requires the ability to measure the magnetic field at the position of the trapped antihydrogen atoms. Physically inserting a Hall probe type device is not a possibility in the ALPHA apparatus and in general is a challenge to make compatible with ultra-high vacuum antimatter traps.

ALPHA solves these two problems by using an electron plasma as an *in situ* diagnostic tool of both the microwave field and the static magnetic field in the trap. In short, microwave radiation at the cyclotron frequency ($f_c = qB/2\pi m$) is used to heat the electron plasma. By maximizing this heating the cyclotron resonance frequency and thus the local magnetic field can be determined. From the magnitude of the heating at the resonance, the strength of the component of the microwave electric field that co-rotates with the cyclotron motion can be determined. This method to measure the electromagnetic fields will be described in greater detail in Chapter 7.

The current chapter covers the underlying method by which the plasma temperature changes are measured using the quadrupole mode oscillation (introduced in Sec. 3.4) of the plasma. The quadrupole mode frequency provides a non-destructive and real-time way to measure the plasma heating due to microwave pulses. This chapter begins with a description of how the dipole and quadrupole mode frequencies of an electron plasma are measured (Sec. 6.1) and examines the baseline evolution of the quadrupole mode frequency over time (Sec. 6.2). In Sec. 6.3, the temperature dependence of the quadrupole mode frequency is established experimentally and shown to be a good measure of temperature changes. Finally, the quadrupole mode frequency measurements are applied to search for enhanced cyclotron cooling rates due to cavity effects (Sec. 6.4). The methods presented here have been implemented in both the ALPHA-1 trap and the ALPHA-2 catching trap. Unless specifically noted otherwise, all measurements presented in this chapter were made using the ALPHA-1 apparatus.

6.1 Plasma Mode Detection

Electron plasmas are used for all of the plasma mode measurements presented here. To clearly distinguish the quadrupole mode oscillation from background noise, relatively large plasmas of 3×10^6 to 7×10^7 electrons are used. Typical plasmas have a radius of 1 mm, densities from 5×10^{13} m^{-3} to 7×10^{14} m^{-3}, and lengths of 20 to 40 mm. These plasmas are confined in a roughly harmonic well formed by applying voltages to 5 electrodes. Below 3×10^6 electrons it becomes difficult to distinguish the quadrupole mode signal from background without driving it at high amplitudes and therefore significantly heating the plasma. The plasmas are characterized using the Faraday cup (Sec. 2.6.1) to measure the number of electrons and the MCP/phosphor screen detector to measure the radial distribution (Sec. 2.6.2) and temperature (Sec. 3.5).

The dipole and quadrupole modes of these plasmas are detected by first exciting them and then picking up the subsequent ringing of the plasma. An arbitrary waveform generator (National-Instruments PXI-5421) outputs Gaussian modulated drive pulses, typically 0.3 V in amplitude for 1 μs, that are applied to an electrode at one end of a trapped electron plasma (see Fig. 6.1). The subsequent ring-down of the plasma mode induces current on nearby electrodes that is picked up, amplified, filtered, and finally digitized (National-Instruments PXI-5122 100 mega-sample/s digitizer). The characteristic ringdown time of the quadrupole mode is typically about 30 μs. The digitized signals from a set of five pulse-and-detect cycles, typically with 100 ms between each cycle, are averaged and the frequency of the mode is determined using a Fast-Fourier Transform (FFT) and a peak-finding routine. In this configuration, the mode frequencies are typically determined at a rate of 1 - 2 s^{-1}. The ringing of the modes can be picked up on either an electrode surrounding the centre of the plasma or on the opposite end to the drive signal. The best signal to noise ratio is obtained when picking up the quadrupole mode on the central electrode and the dipole mode on the end electrode. The quadrupole mode frequency can typically be resolved to within 5 kHz or better. This system can detect both the dipole and quadrupole modes simultaneously but for the majority of the work presented here only the quadrupole mode is driven and detected. This detection system is used with both the ALPHA-1 trap and the ALPHA-2 catching trap with similar electron plasmas in both traps.

As an example, consider a plasma of 7×10^7 electrons with an aspect ratio of 27 and a density of 6.5×10^{14} m^{-3}. The dipole mode of this plasma is detected at a frequency of roughly 16.1 MHz and the quadrupole mode at roughly 26.7 MHz. The analytic theory (see Sec. 3.4), which assumes a cold ($T \to 0$) plasma and a perfect harmonic potential, predicts dipole and quadrupole mode frequencies of 14.8 MHz and 24.2 MHz, respectively. Numerical simulations that take the true potentials and temperature effects into account can be used to calculate mode frequencies that produce better agreement with the measured frequencies and have been used to attempt a full characterization of the plasma using the mode frequencies [44]. Here, however, the quadrupole mode will be used only to measure relative changes in plasma temperature and neither the analytic theory of plasma modes nor the approximate temperature correction of the quadrupole mode frequency will be explicitly used.

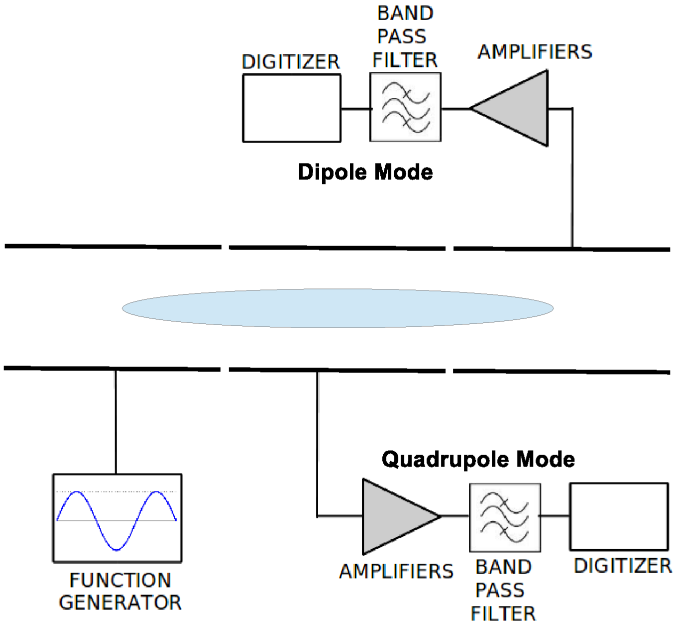

Figure 6.1: A sketch of the plasma mode detection circuit. The pictured configuration is optimal for detecting the quadrupole mode oscillation. A second pickup can be connected to the right most electrode to simultaneously detect the dipole mode oscillation.

6.2 Quadrupole Mode Evolution

One of the benefits of using the plasma mode frequencies as diagnostics is that changes in the plasma properties can be observed in real-time with relatively little disturbance to the plasma. In contrast, to follow the evolution of a plasma using destructive measurements, a series of nominally identical plasmas must be prepared and measured at different times. ALPHA is able to achieve a great degree of reproducibility but small differences from plasma to plasma will always exist.

In order to measure temperature changes due to some process (eg. cyclotron heating) it is important to understand the baseline evolution of the quadrupole mode. Figure 6.2 shows a typical evolution of both the quadrupole and dipole modes (measured simultaneously). The quadrupole mode frequency slowly decreases over time (on the order of 1 ppm/s) while the dipole mode frequency is constant (to within

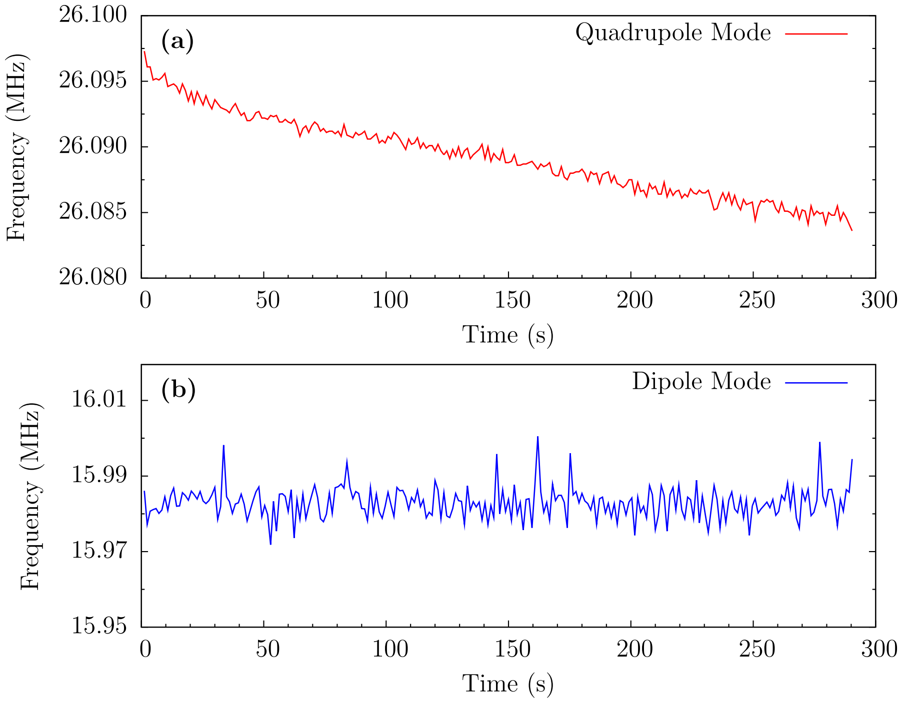

Figure 6.2: Typical evolution of the (a) quadrupole and (b) dipole mode frequencies of an electron plasma. The signal to noise of the dipole mode is larger than the quadrupole mode because it is being driven with a reduced amplitude to avoid plasma heating.

roughly 600 ppm) for the small amount of plasma expansion in Fig 6.2. The decreasing quadrupole mode frequency could be explained by either a slow cooling of the plasma or a slow expansion. Based on destructive temperature measurements, however, the plasma reaches thermal equilibrium after approximately 30 s and remains at a constant temperature. MCP/phosphor screen images of the plasma show that the plasma is slowly expanding which results in a decreasing α and quadrupole mode frequency. The expansion of the plasma is a very small effect and can be neglected in the majority of cases.

If the octupole magnet is turned on, however, this plasma expansion is significantly worsened. As discussed in Sec. 3.1 the octupole breaks the cylindrical symmetry of the Penning trap necessary for stable confinement of non-neutral plasmas. This results in expansion and heating of the plasma by amounts that are observed to be functions

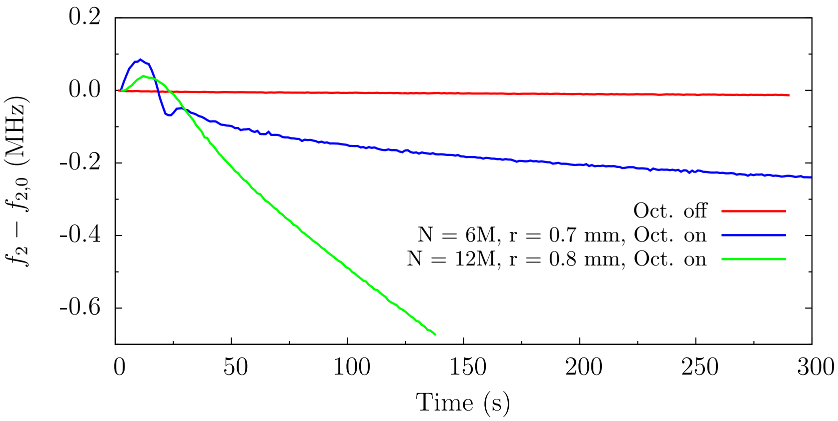

Figure 6.3: Evolution of the quadrupole mode frequency with the octupole magnet at its nominal trapping current. The blue and green traces show the evolution of two different plasmas when the octupole magnet is on. For comparison, the red trace is a typical evolution when the octupole magnet is off.

of the initial plasma size and density. Plasmas with smaller radii and lower densities are affected less by the octupole. The observed effects are in qualitative agreement with a model of diffusive heating in a multipole field [122] but further study is needed to fully understand the observed behaviour. These effects can be seen in real-time by following the quadrupole mode frequency of the plasmas. Figure 6.3 shows the evolution of the quadrupole mode frequency for two different plasma loads at the axial centre of the octupole field compared to the standard evolution with no octupole field. The green and blue curves show an initial increase in the quadrupole mode frequency, corresponding to plasma heating after the octupole magnet has been turned on. The quadrupole mode frequency peaks after roughly 10 s, corresponding to the octupole magnet reaching its full current, and then begins to drop. After 570 seconds, the smaller plasma (blue) expanded from a radius of 0.7 mm to 1 mm while the larger plasma (green) expanded from 0.8 mm to roughly 1.7 mm. Rapid expansion makes it difficult to resolve temperature changes with the quadrupole mode frequency.

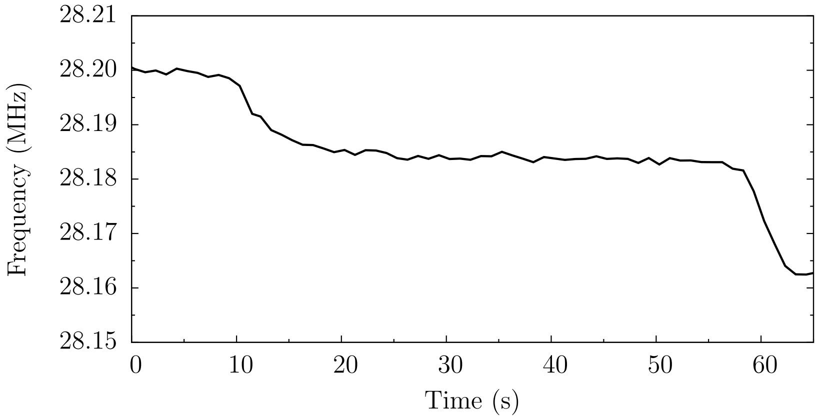

Figure 6.4: Evolution of the quadrupole mode frequency of an electron plasma (N = 5.5×10^7 electrons, r = 0.5 mm) in the ALPHA-2 catching trap showing two sudden drops. The temperature of this plasma was in excess of 1000 K.

6.2.1 Quadrupole mode frequency jumps

In rare instances sudden shifts in the quadrupole mode frequency were observed both in the ALPHA-1 measurements and in the ALPHA-2 catching trap measurements. For example, figure 6.4 shows an example quadrupole frequency evolution with sudden drops in frequency that was observed in the ALPHA-2 catching trap. These changes in frequency correspond to drops in plasma temperature that are observed even when not probing the quadrupole mode frequency. Such shifts were occasionally observed in ALPHA-1 (roughly 1 out of every 20 electron plasmas) but appeared regularly in the initial quadrupole mode measurements in the ALPHA-2 catching trap (every electron load). The initial plasmas used in the ALPHA-2 catching trap were very hot ($>$ 1000 K) and it was observed that by moving the electron plasma to a different set of electrodes the plasma temperature was much lower ($\sim$ 300 K) and the sudden drops occurred very rarely. The sudden changes in quadrupole mode frequency may therefore have been due to noise present on particular electrodes that cause instabilities in the plasma.

In addition, potentially related upward jumps in frequency were also observed in

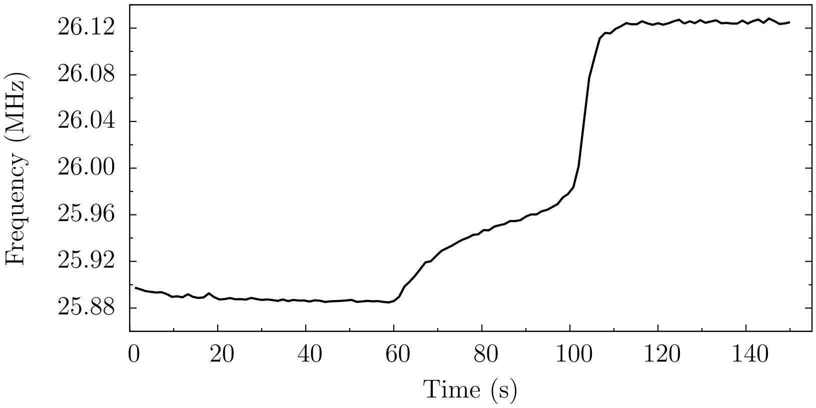

Figure 6.5: Evolution of the quadrupole mode frequency of an electron plasma (N = 2.3×10^7 electrons, r = 1.1 mm) in the ALPHA-1 Penning trap showing a sudden upward jump in frequency at 100 s. At 60 s a radio-frequency heating drive is turned on resulting in an increase in the quadrupole mode frequency.

both Penning traps. These jumps came when the plasma was heated using a radio-frequency drive above an apparent threshold temperature (see Fig. 6.5). Above this threshold the sudden increase in quadrupole mode frequency was always observed. These upward shifts correspond to a sudden rapid increase in plasma temperature and also occur in the absence of the quadrupole mode probe. At this time these sudden changes in temperature are not well understood. Fortunately, these shifts in the baseline quadrupole mode frequency are not a major concern in the microwave measurements presented in Chapter 7 as we are only interested in the change in quadrupole frequency due to short microwave heating pulses.

6.3 Temperature Diagnostic

With an understanding of how the quadrupole mode frequency evolves at a fixed temperature, the frequency change due to heating can be examined. As discussed in Sec. 3.4, the quadrupole mode frequency of a plasma with aspect ratio α is expected to have a temperature dependence given by

$$(f_2)^2 = (f_2^c)^2 + 5\left(3 - \frac{\alpha^2}{2}\frac{\omega_p^2}{(\omega_2^c)^2}\frac{\partial^2 g(\alpha)}{\partial\alpha^2}\right)\frac{k_\mathrm{B}T}{m\pi^2 L_\mathrm{p}^2}, \tag{6.1}$$

where f_2^c is the $T \to 0$ result, m is the electron mass, and L is the plasma length. The function $g(\alpha)$ is given by $g(\alpha) = 2Q_1[\alpha(\alpha^2-1)^{-1/2}]/(\alpha^2-1)$, where Q_1 is the first order Legendre polynomial of the second kind. If the plasma temperature increases by an amount ΔT, the quadrupole mode frequency should therefore be shifted by an amount given by

$$(f_2^{'})^2 - (f_2)^2 = 5\left(3 - \frac{\alpha^2}{2}\frac{f_p^2}{(f_2^c)^2}\frac{\partial^2 g(\alpha)}{\partial\alpha^2}\right)\frac{k_\mathrm{B}\Delta T}{m\pi^2 L_\mathrm{p}^2}, \tag{6.2}$$

where $f_2^{'}$ is the quadrupole mode frequency after the temperature increase. For small temperature changes ($\Delta T < 1000$), the shift in quadrupole mode frequency, $\Delta f_2 = f_2^{'} - f_2$, is small relative to f_2. In this regime, $(f_2^{'})^2 - (f_2)^2 = (f_2^{'} + f_2)\Delta f_2 \approx 2 f_2 \Delta f_2$ and Eq. 6.2 can be expressed as

$$\Delta f_2 = \beta\Delta T, \tag{6.3}$$

where

$$\beta = \frac{5}{2f_2}\left(3 - \frac{\alpha^2}{2}\frac{f_p^2}{(f_2^c)^2}\frac{\partial^2 g(\alpha)}{\partial\alpha^2}\right)\frac{k_\mathrm{B}}{m\pi^2 L_\mathrm{p}^2}. \tag{6.4}$$

It is therefore expected that the increase in the quadrupole mode frequency will be linear with respect to a small change in plasma temperature.

To confirm the linear dependence and determine the parameter β, an experimental calibration of T_final versus Δf_2 can be made using the destructive MCP/phosphor screen temperature diagnostic (Sec 3.5). By experimentally determining β with an independent temperature diagnostic, the quadrupole mode can be used as a temperature probe without relying on theoretical or numerical calculations. This calibration is accomplished by heating the plasma with a radio-frequency drive to a new equilibrium temperature and continuously monitoring the quadrupole mode frequency in the process. Once the plasma has reached equilibrium it is released onto the MCP/phosphor

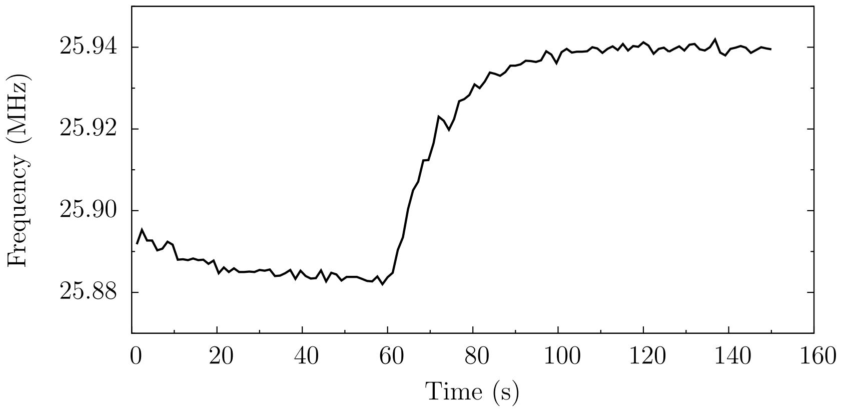

Figure 6.6: An example of the quadrupole mode frequency evolution for an electron plasma (N = 2.3×10^7 electrons, r = 1.1 mm) during a Δf_2 calibration experiment. The quadrupole mode frequency is monitored without heating for 60 s to ensure thermal equilibrium is reached and establish the baseline frequency. At this point the radio-frequency heating drive is applied resulting in an increase in the quadrupole mode frequency.

screen detector to measure its temperature. In this manner, the change in quadrupole mode frequency due to the heating drive can be plotted versus the final plasma temperature. Figure 6.6 shows the quadrupole mode frequency evolution during one of these measurements.

Figure 6.7a shows the resulting ΔT versus Δf_2 calibration plots for plasmas of 2×10^7 electrons and three different aspect ratios. All three datasets show the expected linear behaviour with a slope that depends on the aspect ratio. Similarly, figure 6.7(b) shows the calibration curves for plasmas with similar aspect ratios but different numbers of electrons. Again a linear relationship is observed for all datasets. The different slopes may be due to the length dependence of β (see Eq. 6.4) with greater number of electrons resulting in longer plasmas. The linearity of ΔT against Δf_2 means it can be used as a real-time and non-destructive measurement of temperature change. The experimental slopes are roughly 20 percent larger than would be expected if the approximate temperature correction (Eq. 6.4) was assumed to apply.

In the measurements presented in Chapter 7 a plasma consisting of 1.2×10^7

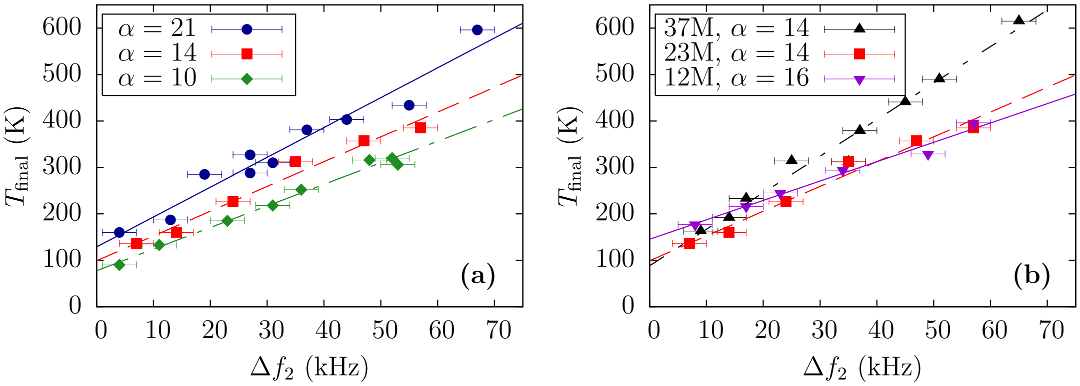

Figure 6.7: Experimental calibrations of $T_{\rm final}$ versus Δf_2. (a) The calibrations for three plasmas consisting of 2.3×10^7 electrons but different aspect ratios is shown. (b) The calibrations for three plasmas with similar aspect ratios but different numbers of electrons. The notation 'nM' denotes a plasma of $n \times 10^6$ electrons.

electrons, $\alpha = 16$, $L_{\rm p} = 26$ mm, and a measured ΔT vs Δf_2 calibration of $1/\beta = 3.7 \pm 0.3$ K/kHz is typically (but not exclusively) used. With a noise level of roughly 5 kHz, temperature changes as small as 5 KHz × 3.7 K/kHz = 20 K can be resolved using these plasma parameters.

6.4 Cavity Mode Search

While not the primary motivation, the quadrupole mode diagnostics proved extremely useful in experiments searching for cavity effects on the cyclotron cooling rate in the ALPHA trap. In free space, charged particles undergoing cyclotron motion around magnetic field lines will spontaneously decay at a rate (Eq. 4.3)

$$\frac{1}{\tau_c} = \frac{q^2\omega_c^2}{3\pi\epsilon_0 c^3 m}. \tag{6.5}$$

In a plasma, the cyclotron degree of freedom will come into equilibrium with the axial degree of freedom so the cooling rate of the plasma must be multiplied by 2/3 to obtain the net cooling rate

$$\frac{1}{\tau_{\rm net}} = \frac{2q^2\omega_c^2}{9\pi\epsilon_0 c^3 m}. \tag{6.6}$$

For electrons and positrons in a 1 T field ($\omega_c = 2\pi \cdot 28 \times 10^9$ Hz) this corresponds to a characteristic cooling time of roughly 4 s.

In a cavity, however, spontaneous decay can be significantly perturbed. When the cavity dimensions are on the same order as the wavelength of the cyclotron radiation, the decay rate can be greatly enhanced or even inhibited entirely. If the cyclotron frequency of the particles matches a mode of the cavity, the spontaneous emission rate is enhanced by a factor of [123, 124] $F_P = 3Q\lambda_c^3/4\pi^2 V$, where Q is the quality factor of the mode and V is the volume of the cavity. This enhancement, known as the Purcell Effect, is the result of an increased density of photon states when the cyclotron frequency matches a resonant mode of the surrounding cavity. In contrast, if the cyclotron frequency is off resonance with the cavity the spontaneous emission can be suppressed [125] and in the extreme case that it is below the cutoff frequency of the cavity, inhibited entirely [126]. Enhanced cyclotron cooling rates of both electron and positron plasmas during antihydrogen trapping experiments would be extremely beneficial for increasing the numbers of trappable antihydrogen atoms.

The ALPHA Penning trap electrodes have a radius that is roughly twice the cyclotron wavelength at 1 T so cavity effects must be considered. Roughly approximated, the ALPHA Penning trap electrode assembly can be treated as an infinitely long cylindrical cavity that supports transverse electric (TE) waves and transverse magnetic (TM) waves. In addition, there is an abrupt change in the electrode radius (from 2.25 cm to 1.68 cm) between the mixing region and the rest of the trap (see Sec. 2.3.2) that can result in reflections. The field in the mixing region of the trap can therefore have an axial dependence similar to $\sin(m\pi z/L_{\text{mix}})$, where m is the integer mode number and L_{mix} is the effective length of the cylinder. The Penning trap is therefore expected to support a set of TE and TM modes characterized by integer mode numbers n, l, and m. Since the dimensions of the trap are comparable to the cyclotron wavelength, tuning the cyclotron frequency to a cavity mode resonance may result in a greatly enhanced cyclotron cooling rate. The frequency and Q-factor of these modes, and the resulting decay rate, were studied experimentally using a set of replica electrodes as well as using simulations. Based on these studies the most promising candidates for detecting such an effect in the ALPHA trap were identified to be the TE_{141} and TE_{143} modes at 25.07 GHz and 25.15 GHz, respectively [127]. These two modes are predicted to have cyclotron cooling times as low as 0.1 s, a factor of 40 enhancement over the free space decay rate.

The replica electrode stack measurements and simulations cannot perfectly predict the frequencies of the modes that the ALPHA trap might support so a search over a wide range of frequencies was performed. One potential way to search for cavity effects is to load a test electron plasma and measure its temperature destructively with the MCP/phosphor screen. By changing the current in the Penning trap solenoid, the cyclotron frequency of the plasma can be changed and if matched to a cavity mode the characteristic cooling time and thermal equilibrium temperature should be modified. Searching in this manner requires one to set the Penning trap field to a desired frequency, load an electron plasma, allow it thermalize, and then destructively measure its temperature. With a potentially large range of cyclotron frequencies that must be searched this method would be extremely time consuming.

Alternatively, the quadrupole mode frequency of the electron plasma can be used as a measure of temperature changes. Because this is a non-destructive measurement, a single electron plasma can be loaded in the trap and the solenoid can be slowly but continuously swept to search the cyclotron frequency range of interest. If the cyclotron frequency passes through a cavity mode, the quadrupole mode frequency will reflect the resulting drop in plasma temperature.

Figure 6.8 shows the quadrupole mode frequency evolution of an electron plasma as

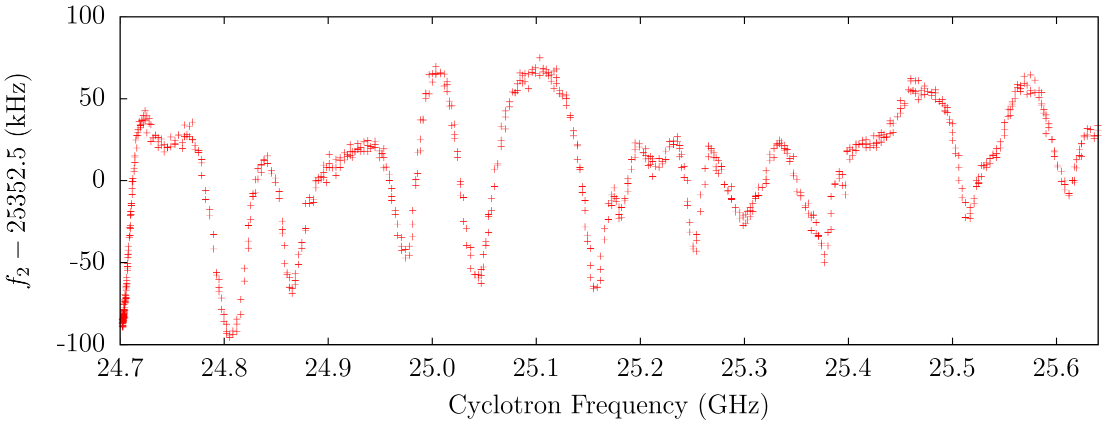

Figure 6.8: The quadrupole mode frequency versus the cyclotron frequency of an electron plasma ($N = 6 \times 10^6$ electrons, $r = 1.1$ mm) as the Penning trap solenoid is swept. The cyclotron frequency is inferred from the field measured by a Hall probe sensor and calibrated by cyclotron frequency measurements presented in Chapter 7. In this plot time moves from right to left because the Penning trap solenoid was swept from high to low current.

the cyclotron frequency was scanned over the range of interest. The plasma consisted of 6×10^6 electrons and the quadrupole mode drive is observed to heat the plasma from 150 K to roughly 500 K. Changes in the quadrupole mode frequency are interpreted as changes in the equilibrium temperature due to changes in the cyclotron cooling rate. Significantly more structure is observed over the entire range that is not consistent with the predicted mode frequencies and spacing. Furthermore, none of the dips in quadrupole mode frequency stand out as a potential cavity mode candidate. The observed structure was reproducible from electron load to electron load and from day to day.

To confirm that fluctuations in the quadrupole mode frequency correspond to temperature changes, a small set of cyclotron frequencies were tested by measuring the plasma temperature with the MCP/phosphor screen detector. Here a plasma of only around 5×10^5 electrons was used to reduce any potential effect that a large number of electrons may have on the cooling time or on the resonant cavity frequency itself. At each cyclotron frequency, a radio-frequency heating drive was applied to a nearby

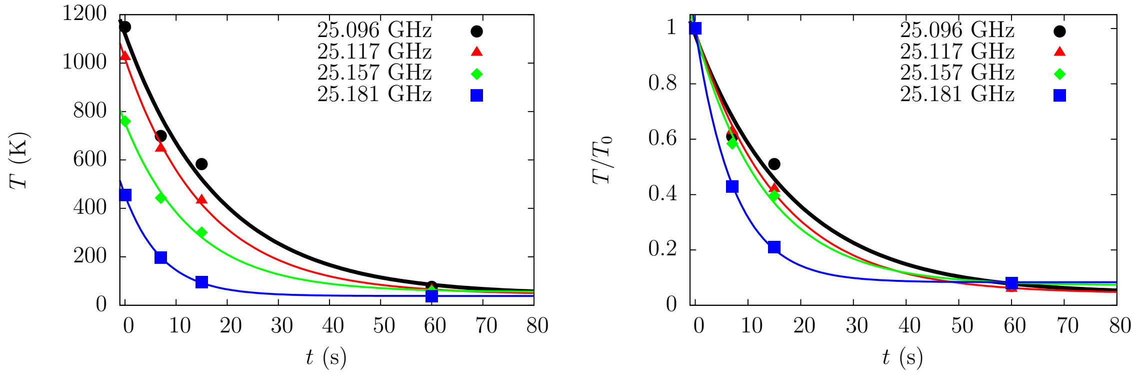

Figure 6.9: (a) Temperature as a function of time as the plasma cools at select cyclotron frequencies. (b) The same curves normalized to their initial temperature in order to better distinguish the difference in cooling times.

electrode and the plasma was allowed to reach a new equilibrium temperature. The heating drive was then turned off and the plasma temperature was measured after cooling for 0 s, 7 s, 15 s and 60 s. Figure 6.9 shows the temperature at these times for a few select cyclotron frequencies showing the range of observed equilibrium temperatures (at $t = 0$ s) and cooling rates. The plasma temperatures 7 s after the end of the heating drive are overlaid with the quadrupole mode frequency scan in Fig. 6.10, showing good agreement. A wait time of 7 s is plotted here because electronic noise adds a large degree of uncertainty to the MCP/phosphor screen temperature measurements above 1000 K. These temperature measurements are consistent with the observed changes in the quadrupole mode frequency. Changes in the plasmas aspect ratio could also be causing the observed fluctuations in the quadrupole frequency. However, there is no known mechanism that would result in the expansion and compression of the plasma due to small changes in magnetic field.

The fluctuations in cyclotron cooling time are not fully understood but do not appear to be consistent with the prediction of trapped modes based on the replica measurements and simulations. This may be due to much lower Q-factors of the cavity modes than predicted or an overloading of the modes due to too many electrons. The fluctuations themselves are extremely interesting, however, and are observed even in

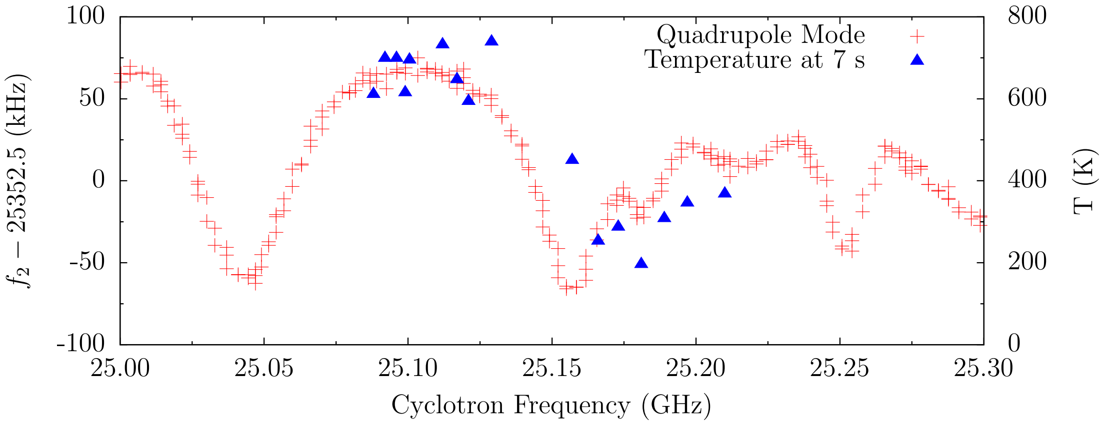

Figure 6.10: The plasma temperatures plotted as a function of cyclotron frequency overlaid with the scan of the quadrupole mode frequency. Note that the cyclotron frequencies of the quadrupole mode scan may be offset by ±0.015 GHz due to a systematic uncertainty in the calibration of the Hall probe.

the normal operating range of the Penning trap solenoid. Over a range of 50 MHz, equivalent to only ∼0.08 A in the solenoid, the cyclotron cooling time can change by roughly a factor of 2. Such fluctuations are highly undesirable for antihydrogen trapping experiments that must ensure stable conditions from day to day to collect statistics.

6.5 Conclusions

Plasma mode based diagnostics are very attractive because of their non-destructive nature but it can be difficult to extract quantitative results from the mode frequencies. The use of mode diagnostics presented here is successful because only relative changes in the plasma are probed and the results are experimentally confirmed using a separate, well established, measurement technique. The results are therefore independent of theory and do not require detailed numerical simulations. A full non-destructive characterization of plasmas would be highly desirable for trapping experiments where, in an ideal world, they would provide a method of characterizing the plasmas in real-time as they are prepared for antihydrogen formation. Unfortunately, there are a number of issues preventing such an implementation in ALPHA. One of the primary issues is that great efforts are made to reduce the plasma temperatures and repeatedly exciting and detecting the dipole and quadrupole motions would heat the plasmas. In addition, the current implementation uses electron plasmas and electric potentials that are optimized for the detection of the quadrupole mode. Trapping experiments, on the other hand, involve many different potential wells (in many positions within the Penning trap) and a range of plasma parameters. It would be difficult to design a compatible mode detection system for this purpose.

The plasma mode diagnostics could be integrated into the trapping experiments on a small scale, however. For example, the positron loads that are transferred from the positron accumulator to the main trap are susceptible to intermittent problems during preparation and transfer. These problems can go undetected until the end of the trapping experiment when a failure becomes apparent, wasting valuable time. If the dipole and quadrupole mode of the plasmas (consisting of $\sim 2 \times 10^7$ positrons) were measured in a temporary mode diagnostic well immediately after transfer, the frequencies could serve as a relative check of plasma parameters. If the mode frequencies deviate significantly from the norm, the full trapping experiment could be aborted in the early stages and restarted.

Chapter 7

Electron Cyclotron Resonance Diagnostics

As discussed in Chapter 6, one of the critical tools needed to perform resonant microwave experiments with trapped antihydrogen is the ability to measure the magnetic field seen by the atoms. This is accomplished by measuring the cyclotron resonance frequency ($f_c = qB/2\pi m$) of an electron plasma. Cyclotron frequency measurements of single particles and sparse clouds in Penning traps are commonly used in high precision mass spectrometry of ions [128–130] and in measurements of the magnetic moment of the electron [131] and proton [67]. In the plasma regime, the cyclotron resonances of electron [82] and ion plasmas [132] have also been studied extensively. Cyclotron resonances in the radio-frequency range (typical for ions, or electrons in a low magnetic field) are relatively easy to detect from the image current induced on nearby electrodes. Electron cyclotron frequencies in ALPHA's high magnetic fields, however, are at high microwave frequencies and must be detected using alternative methods. Single particle cyclotron resonances that lie in the microwave range have been measured using methods that couple the cyclotron motion to the axial motion [64, 131] resulting in detectable shifts in the axial bounce frequency. This chapter will outline and demonstrate a novel method to measure the cyclotron resonance of an electron plasma at microwave frequencies. The key to this method is the use of the quadrupole mode temperature diagnostic that was presented in Chapter 6.

The method is demonstrated for cyclotron frequencies in the microwave range but in principle can also be applied to cyclotron resonances at radio frequencies. The work described in this chapter, as well as the key results from Chapter 6, form a manuscript accepted for publication in the New Journal of Physics [53].

This chapter will also outline how the electron plasmas can be utilized in a microwave electrometry mode. In this mode, the magnitude of the plasma heating due to a pulse of microwaves serves as a measure of the microwave electric field amplitude. Because the Penning trap structure supports a complex set of standing and travelling wave modes, the strength of the microwave electric and magnetic fields can vary drastically as a function of position and frequency. This is illustrated in Fig. 7.1, where the ratio of the power reflected back into the microwave horn to the power output is measured as a function of frequency. Using an electron plasma, the strength of the microwave electric field component that co-rotates with the cyclotron motion can be determined as a function of frequency at the position of the trapped antihydrogen atoms. While this only gives a measure of one component of the electric field, and does not probe the oscillating magnetic field, without these measurements the microwave field seen by antihydrogen atoms would be entirely unknown.

The measurements presented throughout this chapter utilize the same electron plasmas described in Ch. 6. Figure 7.2 sketches the mixing region of the ALPHA Penning trap and the surrounding magnets. The electron plasma is typically centred in the mixing region, which is centred with respect to the neutral atom trap magnets, but can be moved throughout the mixing region to probe the local fields. These techniques were developed and demonstrated in the ALPHA-1 apparatus and repeated in the ALPHA-2 catching trap (see Sec. 2.10). Unless specifically noted otherwise, all presented measurements were performed in the ALPHA-1 apparatus.

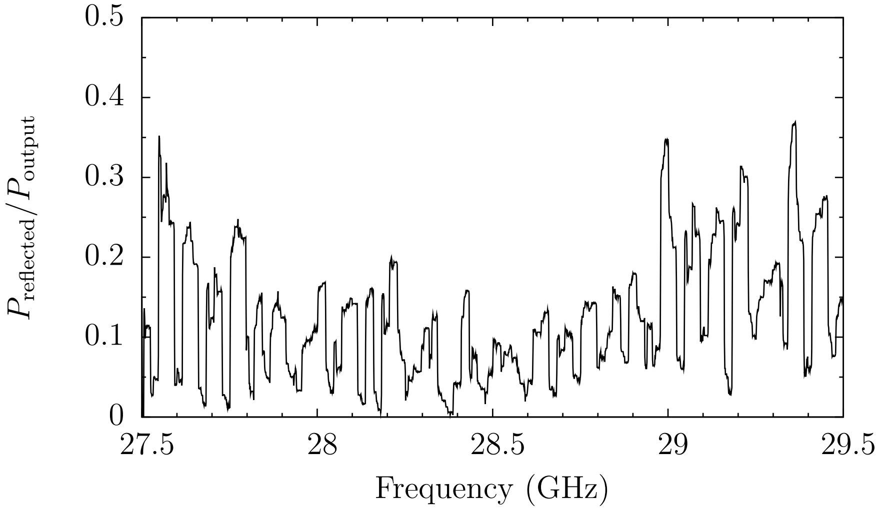

Figure 7.1: A plot of the ratio of the measured power reflected back into the microwave horn and up the internal microwave waveguide (see Sec. 2.8) to the output power of the synthesizer as a function of frequency.

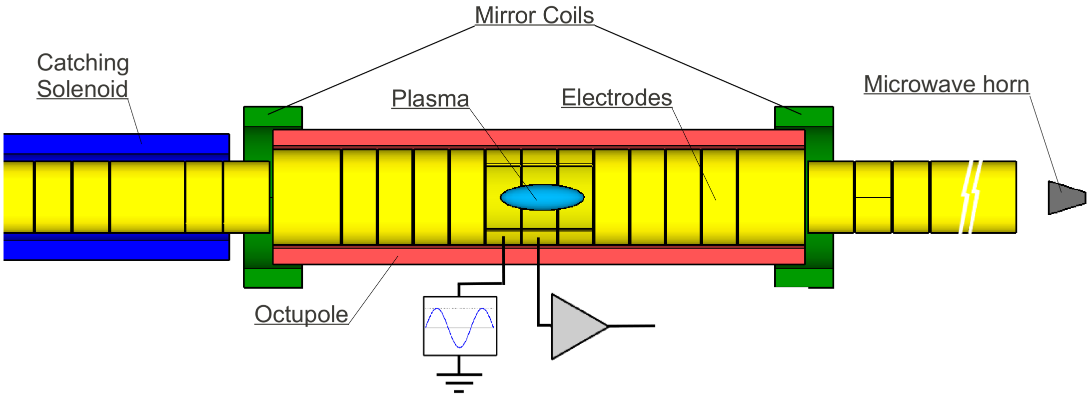

Figure 7.2: Sketch of mixing region of the ALPHA apparatus where the cyclotron resonance measurements were performed. A 1 T solenoid (not pictured) surrounds the components shown here with the exception of the microwave horn located 1.3 m from the centre of the trap. The radial extent of the plasma has been exaggerated for illustration purposes.

7.1 Cyclotron Resonance of an Electron Plasma

Single charged particles in a Penning trap will undergo cyclotron motion at a frequency $f_c = qB/2\pi m$. This simple form makes extracting the magnetic field from the measured cyclotron frequency trivial when the particle mass is known. In non-neutral plasmas, however, the collective behaviour of the particles gives rise to a set of cyclotron modes that occur near the single particle frequency. These modes have been studied experimentally in electron [82] and magnesium ion plasmas in a uniform magnetic field [132, 133]. These cyclotron modes have an angular dependence $\exp(i\ell\theta)$, where ℓ is a positive integer. Assuming the plasma has a uniform density out to a radius r_{p}, the modes are shifted away from the cyclotron frequency by an amount [134]

$$\Delta f_{\mathrm{c},\ell} = \left[\ell - 1 - \left(\frac{r_{\mathrm{p}}}{r_{\mathrm{w}}}\right)^{2\ell}\right] f_{\mathrm{r}}, \tag{7.1}$$

where f_r is the plasma rotation frequency (see Ch. 3) and r_{w} is the inner radius of the electrodes. The $\ell = 1$ mode is downshifted from the single particle cyclotron frequency by an amount $\Delta f_{\mathrm{c},1} = -(r_{\mathrm{p}}/r_{\mathrm{w}})^2 f_{\mathrm{r}}$. This downshift is due to an $\vec{E} \times \vec{B}$ rotation of the plasma around the trap axis resulting from the radial electric fields generated by image charges induced on the electrode walls. This rotation is also known as the diocotron mode of the plasma, which has a frequency $f_d = (r_{\mathrm{p}}/r_{\mathrm{w}})^2 f_{\mathrm{r}}$. The diocotron frequency of plasmas in ALPHA is typically negligible as the plasma radii are on the order of 1 mm compared to the electrode wall radius (in the mixing region) of 22.5 mm. The $\ell > 1$ modes are therefore up-shifted by roughly integer multiples of the plasma rotation frequency. In order to properly infer the magnetic field from the resonance frequency, these modes must be well understood.

7.2 Measuring the Cyclotron Resonance

The cyclotron resonance of an electron plasma is determined by monitoring the quadrupole mode frequency of the plasma while a series of microwave pulses are applied at frequencies that scan through the cyclotron resonance. The cyclotron motion of the electrons will be excited by the co-rotating component of the microwave electric field. Following each pulse, the energy absorbed by the cyclotron motion will be redistributed by collisions to the remaining degrees of freedom. This will result in an increase in the plasma's temperature and therefore an increase in the quadrupole mode frequency of the plasma. When the microwave frequency matches the cyclotron resonance frequency, the quadrupole frequency increase will be maximized. Between each excitation pulse the plasma will cool back to its equilibrium temperature via emission of cyclotron radiation.

The microwave pulses are chosen to be 4 μs in duration such that they are much shorter than the cyclotron cooling time but still have a spectral width that is narrow compared to the cyclotron resonance linewidth. The microwave synthesizer outputs a stable frequency and phase over the duration of the pulse so the full spectral width of each pulse is 500 kHz. An interval of 15 - 30 s is imposed between each microwave pulse to allow the plasma time to cool back to equilibrium. Details of the microwave injection apparatus can be found in Sec. 2.8 (or Sec. 2.10 for details of microwave injection in the ALPHA-2 catching trap).

7.2.1 Uniform Magnetic Field

The cyclotron resonance of an electron plasma in a nominally uniform solenoidal field of 1 T is examined first. Figure 7.3(a) shows the real-time readout of the quadrupole frequency during a cyclotron resonance scan. The cyclotron lineshape is constructed by plotting the quadrupole frequency shift (Δf_2) due to each microwave pulse against

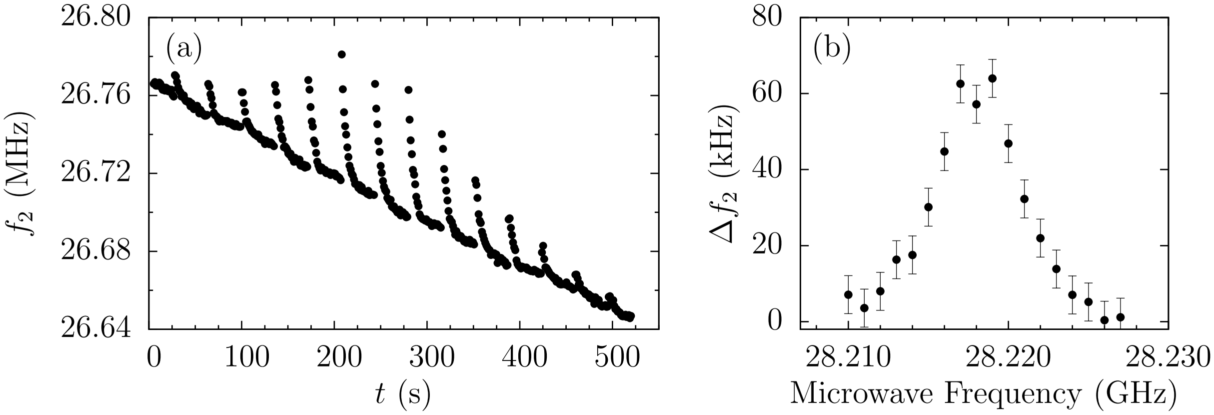

Figure 7.3: (a) The evolution of the quadrupole mode frequency of an electron plasma ($N = 6.6 \times 10^7$ electrons, $r = 0.9$ mm) during a cyclotron resonance scan in a uniform magnetic field. The jumps in frequency are due to 4 μs microwave pulses near the cyclotron resonance frequency. The decreasing baseline quadrupole frequency is consistent with the slow expansion of the plasma. (b) The resulting cyclotron lineshape generated by plotting the quadrupole frequency increases as a function of microwave frequency.

the frequency of the pulse. The resulting lineshape is plotted in Fig. 7.3(b). The temperature dependence of the cyclotron lineshape is studied by applying a radio-frequency drive, consisting of Gaussian noise, to a nearby electrode throughout the cyclotron resonance measurement. Fine scans of the cyclotron resonance for different plasma temperatures are shown in Fig. 7.4. In the 'cold' lineshape (140 K), a roughly Gaussian shape is observed with a dip in the response near the centre. As the temperature is increased a prominent narrow peak emerges and broad side lobe-like features become apparent. Cyclotron resonance measurements in the ALPHA-2 catching trap show these same general features: a large, roughly central, peak with broad side lobe-like features. The relative height of the central peak and the shape of the side lobes change significantly at different cyclotron frequencies (see Fig. 7.5).

The interpretation of these lineshapes is complicated by the strong frequency and position dependence of the microwave field. The narrow width of the central peak is particularly surprising. For comparison, if the microwaves are treated as a plane-wave propagating down the trap axis, Doppler broadening of the cyclotron resonance

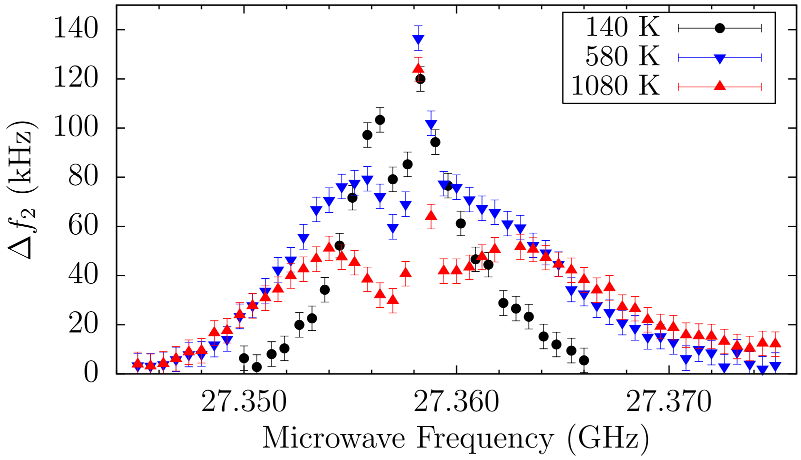

Figure 7.4: Fine scan of cyclotron resonance lineshapes as a function of plasma temperature ($N = 1.2 \times 10^7$ electrons, $r = 0.8$ mm). The plasma temperatures shown are determined using the destructive temperature diagnostic (Sec. 3.5) at the end of each cyclotron resonance measurement.

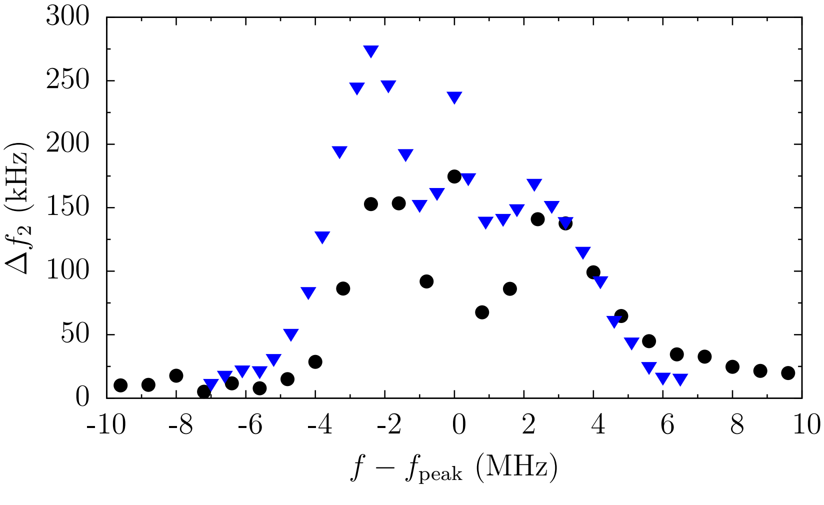

Figure 7.5: Two cyclotron resonance lineshapes measured in the ALPHA-2 catching trap. The central peak frequencies (f_{peak}) of these datasets are 28.027 GHz and 28.066 GHz for the black circles and inverted blue triangles respectively. In both cases the electron plasma consisted of $N = 7 \times 10^6$ electrons with a radius of 0.4 mm and a temperature of approximately 580 K.

would be expected to result in a full-width-at-half-maximum (FWHM) of

$$\Delta f_{\mathrm{FWHM}} = \sqrt{\frac{8k_{\mathrm{B}}T\ln 2}{mc^2}}f_{\mathrm{c}}. \tag{7.2}$$

This corresponds to an expected width of roughly 10 MHz with a 150 K electron plasma. This is an order of magnitude larger than widths of the observed central peak.

Eliminating the Doppler shift is often an important aspect in spectroscopic experiments and can be (intentionally) achieved by a variety of techniques depending on the system. In the hydrogen maser, for example, first order Doppler broadening is removed by confining the hydrogen atoms in a volume that is small compared to the wavelength of the driving field within a microwave cavity. This restricts the particle motions to a region of constant phase resulting in an unbroadened central peak on top of a broad pedestal with the full Doppler width [135]. The electron plasma system under consideration here is similar in that the wavelength is large ($\sim$1 cm) relative to the radius ($r \sim 0.1$ cm) and comparable to the length of the plasma ($L_{\mathrm{p}} = 2$ cm to $L_{\mathrm{p}} = 4$ cm). The observed narrow, seemingly Doppler free, peak may be due to a portion of the electron plasma that is confined within the nodes of a standing wave structure in the Penning trap.

The physics underlying the structure of the observed cyclotron lineshapes remains an open question. Despite this, the position of the central peak can still be used as a measure of the magnetic field strength. Figure 7.6 plots the peak frequency, the microwave frequency that results in the largest Δf_2, as the current in the solenoid is increased. This is plotted against the magnetic field measured by an uncalibrated Hall probe that is placed off axis within the solenoid bore. A linear fit to the data produces a root-mean-square deviation of only 1 MHz. It is concluded that the position of the central peak corresponds to the cyclotron resonance frequency of the electron plasma. This frequency can be determined to within 1 MHz.

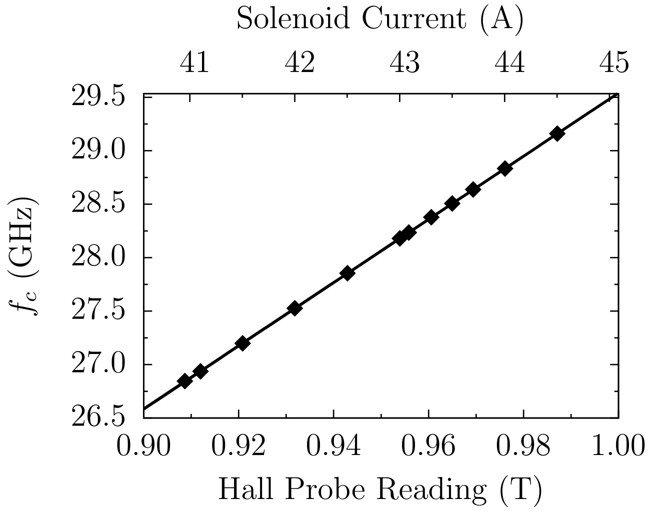

Figure 7.6: The central peak frequency as a function of the solenoid current and an uncalibrated Hall probe.

The expected shifts of the plasma cyclotron modes away from the single particle frequency can be estimated by assuming the plasma density is uniform out to the plasma radius ($r = 1$ mm). With this approximation, the rotation frequency of a plasma with a typical density of $n = 9 \times 10^{13}$ m^{-3} is $f_\mathrm{r} = nq/(4\pi\epsilon_0 B) = 130$ kHz. From Eq .7.1, the cyclotron mode frequencies are therefore expected to be shifted by integer multiples of 130 kHz away from the single particle frequency. These shifts approach the same order as both the full spectral width of the 4 μs pulses and the widths of the observed central peaks. For plasma densities between 8×10^{13} m^{-3} and 2×10^{14} m^{-3} no systematic shifts of the cyclotron lineshapes are observed. It is concluded that, within the current resolution, the measured cyclotron resonance corresponds to the single particle cyclotron frequency. The 1 MHz uncertainty in the cyclotron frequency therefore corresponds to a measurement of the magnetic field to within 3.6 parts in 10^5.

7.2.2 Neutral Atom Trap Magnetic Field

The primary goal of ALPHA's use of the cyclotron resonance of an electron plasma is to measure the magnetic field strength at the position of the trapped antihydrogen atoms. As a first step towards spectroscopy of antihydrogen, Chapter 8 describes the demonstration of resonant interaction with antihydrogen by flipping the spin of the positron through absorption of a microwave photon. This is demonstrated by comparing the results of an 'On resonance' experiment with an 'Off resonance' experiment. In the magnetic neutral atom trap, the positron spin resonance frequency will depend on the position of the antihydrogen atom within the trap. In order to maximize the probability of inducing a spin flip in the 'On resonance' experiments, microwaves are injected at a narrow range of frequencies around the spin flip resonance at the minimum of the neutral atom trap, where the magnetic field is most uniform. It is therefore critical to be able to measure the strength of the minimum magnetic field accurately. Furthermore, to compare a measured positron spin flip transition frequency in antihydrogen to its hydrogen counterpart the magnetic field must be very well characterized.

By measuring the cyclotron resonance lineshape of an electron plasma in the neutral atom trapping fields, the minimum magnetic field can be determined from the minimum cyclotron frequency. Over the extent of the plasma, the octupole field varies by less than 0.1 mT so the field from the mirror coils is treated first. The magnetic field produced by the mirror coils is given by

$$B_z(z,r) = B_0 + a\left(z^2 - \frac{r^2}{2}\right), \tag{7.3}$$

where B_0 is the magnetic field at $z = r = 0$ and $a \approx 0.016\ \mathrm{mT/mm^2}$ when the nominal antihydrogen trapping current is passed through the mirror coils. Over the 1 mm radius of the electron plasma the magnetic field gradient is negligible and the axial gradient will dominate. The mirror field is flattest at its minimum so microwaves

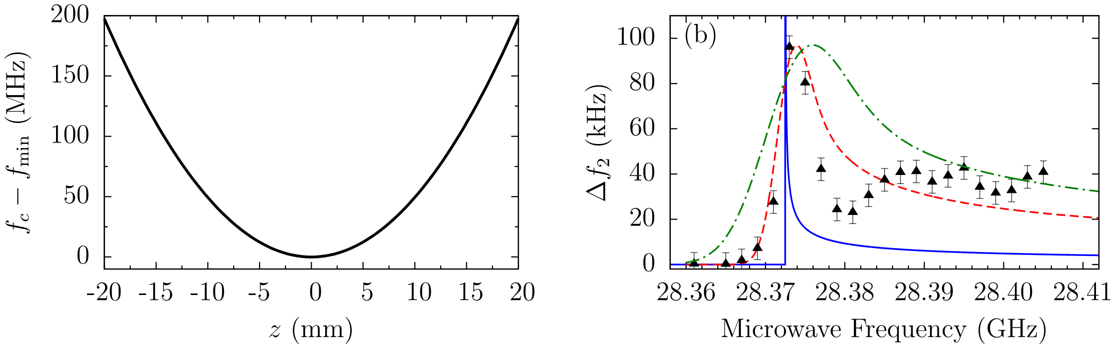

Figure 7.7: (a) The cyclotron resonance frequency as a function of position along the trap axis. (b) Simple models of the expected lineshape in the mirror field and the measured cyclotron lineshape (black triangles) for an electron plasma consisting of $N = 3.7 \times 10^7$ electrons with a radius of 1.4 mm. The solid blue curve is the lineshape expected due to the magnetic field profile alone. The red dashed and green dot-dashed curves show the effect of thermal broadening on this lineshape for plasma temperatures of 25 K and 150 K, respectively. The Doppler width has been calculated assuming the microwave field is a plane-wave propagating down the trap axis.

tuned to the cyclotron resonance at the minimum will be resonant with the largest portion of plasma, maximizing the plasma heating. As the microwave frequency is increased, the field comes into resonance with increasingly narrow slices of plasma. At each frequency, two slices of plasma symmetrically displaced from the minimum will be resonant with the microwave field (see Fig. 7.7(a)).

The expected cyclotron resonance lineshape due to the magnetic field profile is shown in Fig. 7.7(b) (solid blue line). Thermal motion of the electrons parallel to the magnetic field will broaden this lineshape and shift the frequency of the peak cyclotron heating up from the minimum cyclotron frequency. This systematic shift arises from the convolution of a Gaussian with the magnetic field lineshape. In the case where the microwave field is a plane-wave propagating down the trap axis and the plasma temperature is 150 K, the peak heating frequency will be shifted up by 4 MHz. This is illustrated in Fig. 7.7(b) for plasma temperatures of 25 K and 150 K. Without knowing the actual microwave field structure, however, the magnitude of this systematic shift is unknown. In a uniform magnetic field the observed linewidths are smaller than expected in the plane wave case, suggesting that the shift is less than 4 MHz.

This simple model of the expected lineshape is shown against a measured lineshape in Fig. 7.7(b). An onset peak is observed as expected but the measured lineshape deviates significantly from the model at higher frequencies. The deviation from the model is likely due to the spatial and frequency dependence of the co-rotating microwave electric field (CMEF). In Sec. 7.4, an improved model of these lineshapes is produced by taking the spatial dependence of the CMEF into account. The effect of thermal broadening on the magnetic mirror field lineshapes was studied by measuring them with plasmas at temperatures between 150 K and 1000 K. While the onset peak was broadened at higher temperatures, no systematic shift of the peak frequency was observed.

Despite the distortion of the full lineshape, the low frequency onset remains a prominent feature and can be used to measure the magnetic field minimum. The position of the onset peak is taken to be the minimum cyclotron resonance frequency. The onset peak frequency is plotted as a function of the current in the mirror coils in Fig. 7.8(a). Over the range of frequencies plotted, the CMEF amplitude as a function of position will change significantly. These changes will distort the observed lineshapes in different ways, potentially shifting the onset peak frequency. Despite these fluctuations, the onset peak remains a good indicator of the minimum cyclotron frequency and a linear fit to the data results in a root-mean-square deviation of only 10 MHz. Because no systematic shift of the peak frequency was observed due to thermal broadening, it is concluded that the root-mean-square deviation of 10 MHz reflects the uncertainty in determining the minimum cyclotron frequency. This corresponds to a relative magnetic field measurement of $\Delta B/B \approx 3.4 \times 10^{-4}$.

The effect of the octupole magnetic field on the cyclotron resonance was also

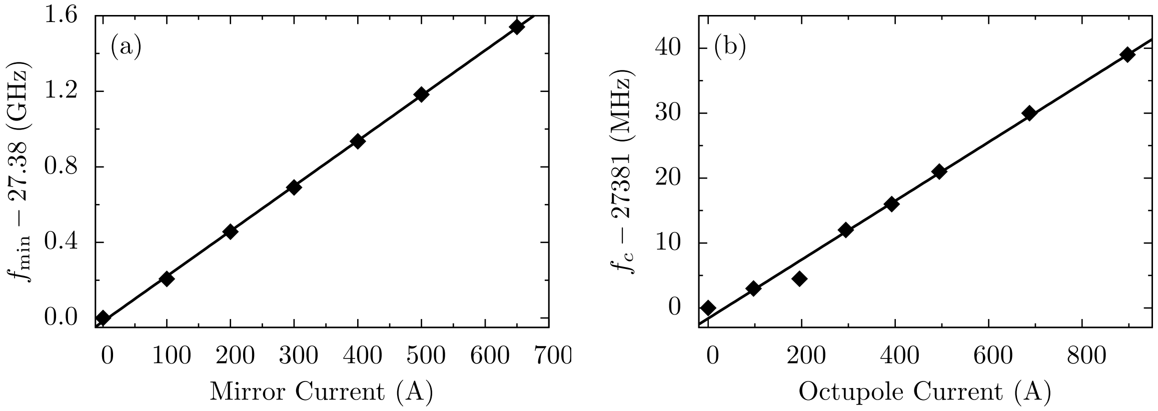

Figure 7.8: (a) Plot of the onset peak frequency against the current in the mirror coil magnets. The octupole magnet is not energized for these measurements. (b) Plot of the cyclotron frequency as a function of the current in the octupole magnet. The mirror coil magnets are not energized for these measurements.

studied. In a perfect octupole field the axial component at the centre of the trap is zero but in reality the end turns in the octupole windings will add a small contribution. The octupole field is approximately uniform over the plasma length and radius so the observed lineshapes are effectively uniform field lineshapes. Figure 7.8(b) plots the measured cyclotron resonance against the current in the octupole. At the nominal antihydrogen trapping current the cyclotron resonance is shifted up by approximately 40 MHz.

When the full neutral trap is energized it is expected that the minimum cyclotron resonance frequency would be a superposition of the measured minimum mirror resonance and the octupole resonance. Surprisingly, however, the minimum cyclotron resonance in the ALPHA neutral trap was found roughly 40 MHz below the expected value. The cause of this deviation is currently unknown but may be due to an interaction between the octupole and mirror magnets (or other superconducting magnets in the ALPHA apparatus) such as a shielding effect or flux pinning effect. While there are no known plasmas effects that could explain this discrepancy, further study is required to completely rule out the possibility of a systematic offset of 40 MHz in the measurement of the minimum field in the full neutral trap arrangement.

7.3 Microwave Electrometry

In addition to providing a probe of the static magnetic field, an electron plasma can also be used to measure a microwave electric field. When the microwave frequency is tuned to the cyclotron resonance of an electron plasma, the magnitude of the plasma heating will be a function of the CMEF amplitude of the driving pulse. From the resulting quadrupole frequency increase, the CMEF amplitude can therefore be estimated and compared at different frequencies (Sec. 7.3.1). The CMEF amplitude can also be used to roughly estimate the expected positron spin flip rate in trapped antihydrogen. In addition, the spatial dependence of the CMEF amplitude can be studied in this manner (Sec. 7.3.2). If a magnetic field gradient is applied across the length of the plasma, the cyclotron resonance will be a function of position. A microwave pulse at a fixed frequency will then only heat a narrow slice of the plasma by an amount proportional to the local CMEF amplitude squared. The Penning trap solenoid field can then be changed (keeping the gradient fixed) to move the resonance position. In this manner the relative CMEF amplitude can be measured as a function of position over the length of the plasma. If the CMEF amplitude were uniform over the plasma length this would be analogous to a one-dimensional magnetic resonance imaging scan of the plasma shape.

7.3.1 Electric field amplitude

To estimate the CMEF amplitude from a measured changed in temperature, the electron plasma is treated as a collection of single particles oscillating at the cyclotron frequency. Using the equations of motion for an electron in an electromagnetic field

$$m\frac{d\vec{v}}{dt} = q\vec{E} + q\vec{v} \times \vec{B}, \tag{7.4}$$

the average change in kinetic energy of a collection of electrons exposed to a near resonant co-rotating electric field can be calculated. Here it is assumed that the microwave pulses are short compared to damping and collisional timescales such that these effects can be neglected. The equations of motion are simplified by letting $\omega_c = qB/m$ and decomposing the electric field into components that co-/counter-rotate with the cyclotron motion. Equation 7.4 then becomes

$$\frac{dv_\pm(t)}{dt} = \mp i\omega_c v_\pm(t) + E_\pm(t), \tag{7.5}$$

where $v_\pm = v_x(t) \pm iv_y(t)$ and $E_\pm(t) = E_x(t) \pm iE_y(t)$. The solution to Eq. 7.5 is

$$v_\pm(t) = \left[v_\pm(t_0)e^{\pm i\omega_c t_0} + \frac{q}{m}\int_{-\infty}^{t} e^{\pm i\omega_c t'} E_\pm(t')dt' \right] e^{\mp i\omega_c t}. \tag{7.6}$$

The change in average transverse kinetic energy, $\langle \mathrm{KE}_\perp \rangle = m\langle v_+ v_- \rangle/2$, due to a pulse of microwaves is therefore

$$\Delta\langle \mathrm{KE}_\perp \rangle = \frac{q^2}{2m}\left| \int_{-\infty}^{\infty} E_+(t')e^{i\omega_c t'}dt' \right|^2, \tag{7.7}$$

where $E_+(t)$ is the co-rotating component of the electric field. Following the microwave pulse, collisions redistribute the kinetic energy among the three degrees of freedom resulting in a temperature change of

$$\Delta T = \frac{2}{3k_\mathrm{B}}\Delta\langle \mathrm{KE}_\perp \rangle. \tag{7.8}$$

The rate at which collisions bring the cyclotron motion of the electrons into equilibrium with the parallel motion is given by Eq. 3.18. For an electron plasma with a density of $n = 2 \times 10^{14}$ m^{-3} at 150 K in a 1 T field the pulses must therefore be shorter than ${\Gamma_\mathrm{col}}^{-1} \sim 2 \times 10^{-5}$ s for Eq. 7.7 to be valid. This criterion is satisfied by using microwave pulses that are 8×10^{-8} s in duration, roughly two orders of magnitude shorter than the rate that collisions bring the electron cyclotron motion into equilibrium with the parallel motion.

The transverse components of the CMEF during a square pulse an be approximated as

$$E_x(t) = E_{x,0}\cos(\omega t)[H(t+\tau/2) - H(t-\tau/2)], \tag{7.9}$$

$$E_y(t) = E_{y,0}\cos(\omega t + \delta_y)[H(t+\tau/2) - H(t-\tau/2)], \tag{7.10}$$

where H is the Heaviside step function and τ is the pulse duration. Taking the Fourier transform of the co-rotating component of the electric field gives

$$\int_{-\infty}^{\infty} E_+(t')e^{i\omega_c t'}dt' = \left(\frac{\sin[(\omega-\omega_c)\tau/2]}{\omega-\omega_c} + \frac{\sin[(\omega+\omega_c)\tau/2]}{\omega+\omega_c}\right)E_0, \tag{7.11}$$

where $E_0 = E_{x,0} + iE_{y,0}e^{i\delta_y}$. Near resonance the second term is small relative to the first and can be neglected to write

$$\int_{-\infty}^{\infty} E_+(t')e^{i\omega_c t'}dt' = \frac{\tau}{2}\mathrm{sinc}\left(\frac{\Delta\omega\tau}{2}\right)E_0, \tag{7.12}$$

where $\Delta\omega = \omega - \omega_c$. Inserting Eq. 7.12 into Eq. 7.7 gives

$$\Delta\langle \mathrm{KE}_\perp\rangle = \frac{q^2\tau^2}{8m}\mathrm{sinc}^2\left(\frac{\Delta\omega\tau}{2}\right)|E_0|^2. \tag{7.13}$$

From Eq. 7.8 and Eq. 7.13 the amplitude of the CMEF ($|E_0|$) is therefore related to the change in quadrupole mode frequency Δf_2 by

$$|E_0| = \frac{2\sqrt{3mk_\mathrm{B}\Delta f_2/\beta}}{q\tau}, \tag{7.14}$$

where $\beta = \Delta f_2/T$ and is determined by the quadrupole mode calibration described in Sec. 6.3.

As an example, a plasma of 1.2×10^7 electrons ($n = 2\times 10^{14}$ m^{-3}) with a measured quadrupole mode frequency calibration of $1/\beta = 3.7$ K/kHz was used. After determining the cyclotron resonance using the procedure described in Sec. 7.2.1, microwaves were injected at a resonant frequency of 27.370 GHz in 80 ns pulses. A microwave power of 9 mW emitted from the microwave horn resulted in a quadrupole mode frequency shift of 100 KHz, corresponding to an co-rotating electric field amplitude of 18.4 V/m. By changing the Penning trap solenoid current, the resonant frequency could be modified to measure the CMEF amplitude at different frequencies. This was used to compare the microwave fields at the frequencies used in the positron spin flip experiment (Sec. 8.2).

7.3.2 Electric field mapping

Using the above technique, the axial dependence of the CMEF amplitude can be measured by repositioning the plasma within the Penning trap. Any changes in the CMEF amplitude on a scale smaller than the length of the plasma (2 - 4 cm), however, will be averaged out. To probe the CMEF amplitude on a finer scale, a magnetic field gradient can be applied across the length of the plasma such that a microwave pulse at a given frequency will only be resonant with a small portion of the plasma. The position of the resonance can then be moved by changing the Penning trap solenoid field (keeping the gradient fixed).

In ALPHA, a magnetic field gradient can be produced by the fringe field of the superconducting catching solenoid that is next to the mixing region of the Penning trap (see Fig. 7.2). The resonance position is scanned across the plasma by slowly changing the current in the Penning trap solenoid and applying a microwave pulse every 35 s. This process is sketched in Fig. 7.9. The resonant position of each pulse is determined using a numerical model of the magnetic field gradient produced with the TOSCA/OPERA3D software package [136]. A microwave pulse duration of 4 μs with a full spectral width of 500 kHz is used such that only a small portion of the plasma is excited with each pulse. These pulses do not fall within the short pulse limit necessary to estimate the CMEF amplitude as in Sec. 7.3.1. However, the plasma heating due to each pulse will still serve as a measure of the relative local CMEF amplitude.

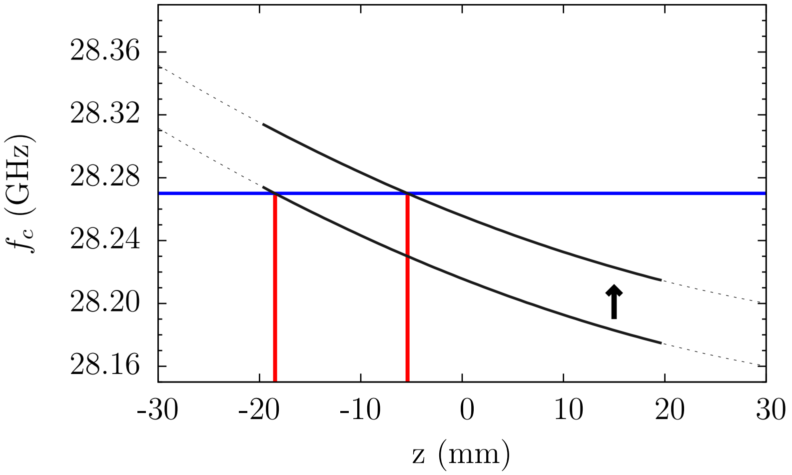

Figure 7.9: A plot that sketches the scanning of the resonance position across the plasma. The solid black lines show the cyclotron resonance as a function of axial position over the length of the plasma at two different times. The horizontal blue line indicates the injected microwave frequency and the resonance positions at the two times are marked by vertical red lines.

If the strength of the CMEF was uniform over the length of the plasma, this technique would be analogous to a magnetic resonance imaging of the plasma. In that case, the relative plasma heating due to each pulse would only be a function of number of electrons that are in resonance with each pulse. Here, however, the CMEF amplitude is highly variable over the length of the plasma, which can be approximated by an elongated ($\alpha \sim 20$) uniform density spheroid. By scanning the resonance across the plasma and measuring the quadrupole frequency shifts due to each microwave pulse, a one-dimensional map of the relative CMEF strength along the z-axis can be generated.

As an example, figure 7.10 plots $(\Delta f)^{1/2}$, which is proportional to the CMEF amplitude, as a function of z for a microwave frequency of 28.375 GHz. In an idealized case, where the plasma is a uniform density cylinder and the magnetic field gradient is perfectly linear, the measured $(\Delta f)^{1/2}$ will depend only on the local CMEF amplitude. In reality, the slope of the magnetic field gradient changes slightly as a function of

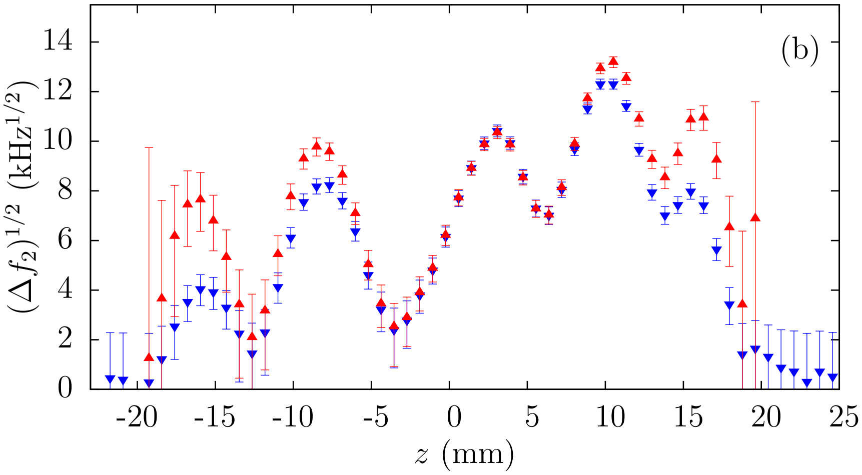

Figure 7.10: The square root of the quadrupole frequency increase as a function of axial position with a microwave frequency of 28.375 GHz (inverted blue triangles). Assuming a perfectly linear magnetic field gradient and a cylindrical plasma the measured response reflects the relative CMEF amplitude. The red triangles are the same measurements corrected for the spheroidal shape of the plasma and the changing slope of the magnetic gradient. The plasmas used here consisted of $N = 3.7 \times 10^7$ electrons and had a radius of 1.4 mm.

position and the plasma is better approximated as a spheroid. These two effects change the number of electrons in resonance with each pulse as a function of position. To adjust for this, two multiplicative correction factors are applied. The radius of the spheroidal plasma changes as a function of z so $(\Delta f)^{1/2}$ is multiplied by a correction factor

$$\frac{r(0)}{r(z)} = \left(1 - \left(\frac{2z}{L}\right)^2\right)^{-1/2}, \tag{7.15}$$

where $L_\text{p} = 40$ mm for the plasma used in Fig. 7.10. To correct for the changing slope of magnetic field gradient, a factor of $(B'(z)/B'(0))^{1/2}$ is also applied, where $B'(z) = dB/dz$. Both of these correction factors have been normalized to the response at the centre of the plasma. The effect of the corrections can be seen in Fig. 7.10. The correction for the spheroidal shape of the plasma breaks down at the ends of the plasma ($|z| = L_\text{p}/2$). Better measurement of the CMEF amplitude at these points can be obtained by repositioning the plasma.

The spatial resolution of this scan is set by the slope of the magnetic field gradient and the width of the resonance. The resonance width is estimated to be 0.2 mT based on the observed linewidth of a plasma at 140 K in the uniform field (see Fig. 7.4). Based on this linewith and a magnetic field gradient slope of approximately 0.09 mT/mm, each microwave pulse will excite a slice of plasma approximately 2 mm long.

7.4 Modelling Neutral Atom Trap Lineshapes

In Sec. 7.2.2 the cyclotron resonance lineshapes were observed to be significantly distorted by the frequency and spatial dependence of the CMEF amplitude. With the ability to measure the relative CMEF amplitude as a function of position, one of these factors can be accounted for and an improved model of the lineshapes can be produced. Starting with the simple lineshape model discussed in Sec. 7.2.2, a frequency dependant factor can be applied based on a measured map of the CMEF amplitude along the axis.

The simple model of the cyclotron resonance lineshapes is based on the expected lineshape due to the mirror magnetic field convolved with a Gaussian to account for thermal broadening. The structure of the microwave field is not known well enough to accurately model the thermal broadening so the width of this Gaussian is left as a fit parameter. In the mirror magnetic field, each microwave frequency is resonant with two slices of plasma that are symmetrically displaced from $z = 0$ (see Fig. 7.7(a)). From the measured CMEF map, the relative CMEF strengths at these two positions can be estimated to determine how the lineshape should be distorted.

Using the CMEF profile measured at 28.375 GHz (Fig. 7.10), an improved model for the lineshape shown in Fig. 7.7(b) is plotted in Fig. 7.11(a). The improved model reproduces the onset peak well and qualitatively reproduces the structure of the

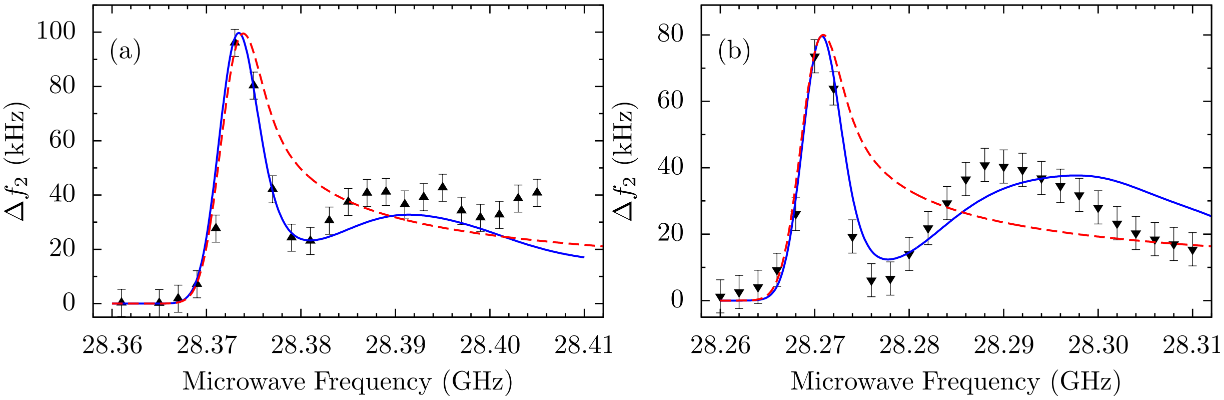

Figure 7.11: (a) The improved model (blue line) of the cyclotron resonance lineshape shown in Fig. 7.7(b) using a CMEF amplitude map at a frequency of 28.375 GHz. The red dashed line shows the simple model (not accounting for the spatially varying CMEF) for comparison. (b) A second example of a modelled lineshape (blue line) at a different range of cyclotron frequencies using a CMEF map at 28.270 GHz compared to the simple model (red dashed line).

lineshape at higher frequencies. The fact that the improved model still deviates at higher frequencies is likely due to the fact that the CMEF profile changes as a function of frequency, which is not accounted for here. A second example of this process is shown in Fig. 7.11(b) for a lineshape in a different frequency range with similar results. While these fits are rough, their improved agreement with the observed cyclotron lineshapes provides a measure of confidence that the lineshapes are due to the magnetic field inhomogeneity, thermal broadening, and the spatial and frequency dependence of the CMEF amplitude.

7.5 Conclusions and Outlook

The methods presented in this chapter were critical to the demonstration of resonant positron spin flips in trapped antihydrogen. Using the cyclotron resonance of an electron plasma the magnetic field in the ALPHA trap was measured to within 3.6 parts in 10^5 for a uniform magnetic field. In the magnetic minimum trap, the minimum was resolvable to within 3.4 parts in in 10^4, with a potential systematic offset of 1.4 parts in 10^3 that cannot be ruled out at this time. This level of precision was more than sufficient for the current demonstration of resonant positron spin flip transitions. Applied to 1S - 2S spectroscopy, a magnetic field uncertainty of 3.4 parts in 10^4 would translate to an inaccuracy of only 64 Hz (2.5 parts in 10^{14}) in the transition frequency (assuming a 1 T minimum field) [137]. With hardware improvements and further study these measurements could reach a resolution limited by collisional scattering (roughly 1 part in 10^6 for a typical plasma used here).

In a nominally uniform magnetic field the cyclotron resonance frequency was measured to within 1 MHz. This is of the same order as the full spectral width of the 4 μs microwave pulses used and may be improved with the use of longer pulses. This is also approaching the order on which the shifted cyclotron modes of the electron plasma become significant. As the resolution of the cyclotron frequency measurement is improved, careful study of the cyclotron mode frequencies will be necessary.

A non-uniform magnetic field over the plasma length results in significant distortion of the cyclotron resonance lineshapes due to the spatial dependence of the microwave electric field. In the neutral atom trap field, the uncertainty in determining the minimum magnetic field is dominated by these effects. The new version of the ALPHA apparatus (Chapter 9) will include three additional mirror coils which can be used to flatten the field minimum while maintaining the neutral trap depth. With a flatter magnetic field, more of the plasma will be in resonance at the minimum cyclotron frequency and variations in the CMEF strength will be averaged over a longer range, approaching the uniform field case.

The spatial uncertainty of the microwave electric field can be removed if the plasma is confined within a microwave cavity with a known mode structure. In addition, if the majority of the plasma is confined between the nodes of a trapped cavity mode the lineshape will be dominated by a Doppler free peak at the cyclotron frequency [135], greatly increasing the achievable resolution. Designing a microwave cavity that is compatible with the storage and manipulation of plasmas presents a challenge but may be included in a future upgrade to the ALPHA apparatus.

The use of the plasma's quadrupole mode frequency to measure the cyclotron resonance is a novel technique that is not limited to cyclotron frequencies in the radio-frequency range. Implementation of these techniques requires an electron or ion plasma with a detectable quadrupole mode frequency and a method for exciting the cyclotron motion. This chapter has focused on the measurement of the electromagnetic fields in a cylindrical Penning trap but the use of the quadrupole mode to measure the cyclotron resonance may be useful for the study of cyclotron resonances of non-neutral plasmas or for field diagnostics in mass spectrometry experiments.

Chapter 8

Positron Spin Flips in Antihydrogen

Precision spectroscopy of antihydrogen is one of the primary goals of the ALPHA collaboration. This chapter presents the first spectroscopic measurement of antihydrogen, and the first such measurement on a pure antimatter atom, by inducing resonant positron spin flip transitions between hyperfine levels of antihydrogen's ground state. The work presented here is a proof of principle demonstration, rather than a precision measurement, but is a first critical step towards spectroscopy of antihydrogen. [1]

8.1 Strategy

In a magnetic field, antihydrogen's ground state is split into two trappable states and two untrappable states (Fig. 8.1). In the high field limit, the trappable states have a positron spin that is anti-aligned with the magnetic field and untrappable states have a positron spin that is aligned with the field (see also Sec. 2.4). The two transitions, $|c\rangle \rightarrow |b\rangle$ and $|d\rangle \rightarrow |a\rangle$, therefore correspond to a flip of the positron spin and are known as positron spin resonance (PSR) transitions. Assuming that CPT symmetry holds to a sufficient accuracy these two transition frequencies are separated by approximately 1420.4 MHz; the zero field hyperfine splitting. A resonant oscil-

---

[1] This experiment benefited greatly from the work of Mohammad Dehghani Ashkezari (PhD candidate). Additional details on the microwave hardware, methods, and results can be found in his soon to be published thesis [138].

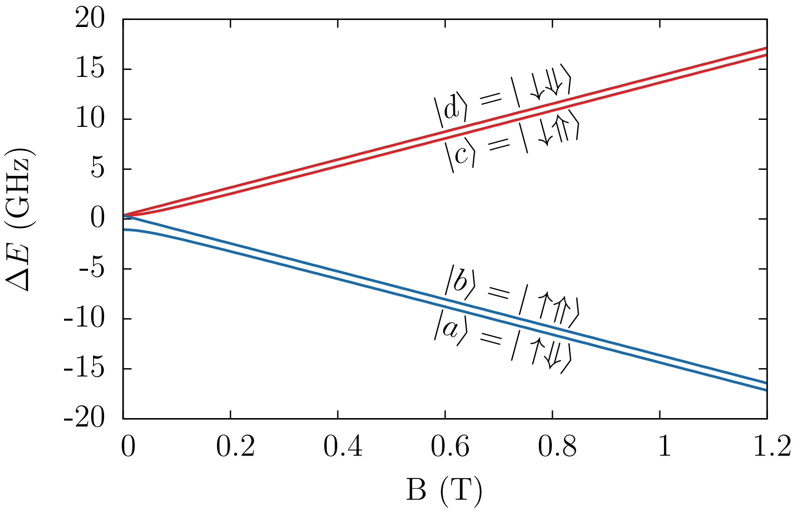

Figure 8.1: Breit-Rabi diagram for the ground state of hydrogen (and antihydrogen if CPT invariance holds) in a magnetic field showing the relative energy levels in frequency units. The arrows in the state vectors denote the positron (single arrow) and antiproton (double arrow) spins in the high field limit. Antihydrogen atoms in states $|c\rangle$ or $|d\rangle$ (red) will be trapped while those in $|b\rangle$ or $|a\rangle$ (blue) are untrapped.

lating magnetic field applied perpendicular to the magnetic trapping fields can drive these transitions, flipping antihydrogen from a trapped state to an untrapped state. The antihydrogen atom will then quickly annihilate on the surrounding electrodes, providing a clear signal of an induced transition.

To establish resonant induction of the PSR transitions, three types of measurements were performed: microwaves on resonance, microwaves off resonance, and no microwaves. All measurements started with a standard trapping attempt (see Sec. 5.2) up to the point when antihydrogen has been formed and all charged particles have been removed. Following this, a 60 s holding time was imposed to allow the current in the neutral trap magnets to be changed slightly and to stabilize. The antihydrogen atoms were then held for a further 180 s, during which time the microwaves could be introduced, before shutting down the magnetic trap to detect the annihilation of any remaining atoms.

The inhomogeneous magnetic trapping fields result in PSR lineshapes similar to

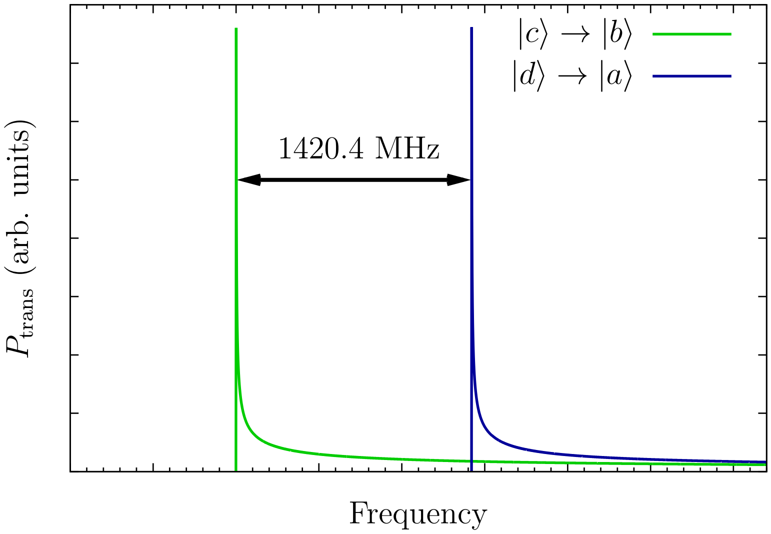

Figure 8.2: Calculated transition probability (P_{trans}) for the PSR transitions as a function of frequency in the magnetic neutral atom trap. Only the magnetic field has been taken into account here.

the expected cyclotron resonance lineshape of an electron plasma (Fig. 8.2). Similar to the cyclotron resonance lineshapes, the abrupt low-frequency onsets correspond to antihydrogen PSR transitions induced at the magnetic trap minimum, where the field is most uniform. The long high frequency tails are due to the highly inhomogeneous trapping fields surrounding the minimum. The probability of inducing a PSR transition was maximized by choosing the resonance condition such that transitions were induced at the magnetic minimum. This also has the effect of localizing the position where the transitions occur. Because the initial state of the atoms ($|c\rangle$ or $|d\rangle$) was unknown, the frequency of the microwave field was alternated between the two transition frequencies.

A total of six series of measurements were performed to demonstrate resonant transitions and rule out potential systematic effects. In series 1, the minimum on-axis magnetic field was set to a field B^{A} and a resonant microwave field was applied at the transition frequencies (Fig. 8.3(a)). The microwave frequency was first swept from -5 MHz to +10 MHz around the target $|c\rangle \to |b\rangle$ transition frequency, f^{A}_{cb}, over 15 s. The same sweep was then applied to the $|d\rangle \rightarrow |a\rangle$ transition around f_{da}^{A}. These two sweeps alternated for the full 180 s window. Series 2 used the same microwave sweeps but the mirror coil current was increased to bring the magnetic minimum to $B^{\mathrm{B}} > B^{\mathrm{A}}$ such that f_{cb}^{A} and f_{da}^{A} were detuned below resonance by 100 MHz (Fig. 8.3(b)). Note that while $|d\rangle \rightarrow |a\rangle$ transitions should be eliminated in series 2, there is still a probability of inducing $|c\rangle \rightarrow |b\rangle$ transitions. In series 3, the magnetic field was set to B^{B} and the microwave frequencies were brought back into resonance by sweeping around the target frequencies $f_{cb}^{\mathrm{B}} = f_{cb}^{\mathrm{A}} + 100$ MHz and $f_{da}^{\mathrm{B}} = f_{da}^{\mathrm{A}} + 100$ MHz (Fig.8.3(c)). Series 4 was identical to series 2 but was interspersed with series 3 measurements to control for potential changes in experimental conditions over time. Finally, series 5 and 6 measured the trapping and annihilation rate when no microwaves are injected. The minimum on-axis magnetic field was set to B^{A} in series 5 and B^{B} in series 6.

8.2 Cyclotron Resonance Measurements

The cyclotron resonance measurements described in Ch. 7 play two important roles for this experiment. First, they provide the critical ability to set and ensure the stability of the magnetic field. Second, they allow the microwave fields at each of the target frequencies to be compared and characterized. It should be noted that the microwave field measurements only probe the co-rotating component of the electric field and not the oscillating magnetic field that drives the positron spin flip. As such these measurements provide only a rough qualitative estimate but are an important diagnostic tool here where the microwave field would otherwise be entirely unknown.

Based on the strategy described in the previous section, microwave frequency sweeps over a 15 MHz range are applied around four target frequencies: f_{cb}^{A}, f_{da}^{A}, f_{cb}^{B}, and f_{da}^{B}. At a magnetic field X (where $X =$ A or B), f_{cb}^{X} and f_{da}^{X} are separated by

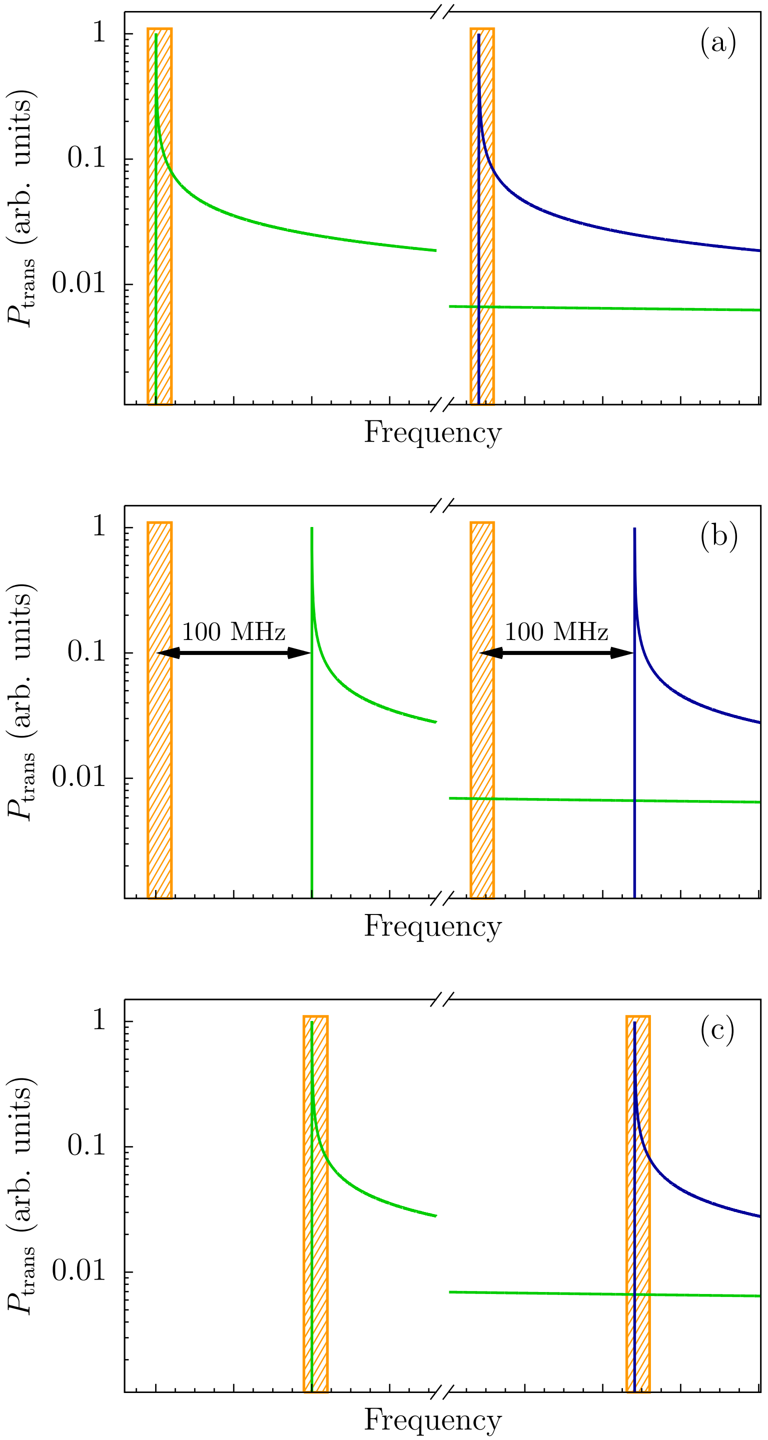

Figure 8.3: Sketches of (a) series 1 (on resonance) (b) series 2/4 (off resonance) and (c) series 3 (on resonance) experiments to demonstrate resonant induction of PSR transition in antihydrogen. The orange bands represent the range of the microwave frequency sweep from -5 MHz to + 10 MHz around the target frequencies. The transition probability has been plotted on a log scale and normalized to the probability at the minimum frequency.

the 1420.4 MHz zero-field hyperfine splitting and $f^{\mathrm{B}}_{mn} = f^{\mathrm{A}}_{mn} + 100$ MHz. In an ideal scenario, the microwave field would be identical at these four frequencies. Unfortunately, because of the Penning trap environment it is not possible to choose a set of four frequencies with identical microwave fields. Using the microwave electrometry techniques presented in Sec. 7.3, the differences between co-rotating component of the microwave electric field at each of these frequencies can be compared and minimized.

The four target frequencies were chosen to be: $f^{\mathrm{A}}_{cb} = 28.276$ GHz, $f^{\mathrm{A}}_{da} = 29.696$ GHz, $f^{\mathrm{B}}_{cb} = 28.376$ GHz, and $f^{\mathrm{B}}_{da} = 29.796$ GHz. The measured CMEF amplitudes at these frequencies are: $|E(f^{\mathrm{A}}_{cb})| = 11 \pm 3$ Vm^{-1}, $|E(f^{\mathrm{A}}_{da})| = 15 \pm 2$ Vm^{-1}, $|E(f^{\mathrm{B}}_{cb})| = 13 \pm 2$ Vm^{-1}, $|E(f^{\mathrm{B}}_{da})| = 10 \pm 3$ Vm^{-1} (see Sec. 7.3.1). These amplitudes are enhanced by a factor of $\sim$10 by using the high power microwave injection path (see Sec. 2.8) for the spin flip experiments. For hyperfine spectroscopy of trapped antihydrogen. it is desirable to estimate the positron spin flip rate expected. This rate is determined by the transverse component of the microwave magnetic field, rather than the CMEF amplitude that has been measured. If the microwave field is assumed to be a plane wave, a CMEF amplitude of 100 Vm^{-1} corresponds to a co-rotating magnetic field amplitude of $B = E/c \approx 0.33$ μT. Based on simulations of the dynamics of trapped antihydrogen interacting with an oscillating magnetic field of this amplitude, a spin flip rate of roughly 1 s^{-1} is expected [6].

In addition, the relative CMEF strengths along the length of the plasma at the four frequencies were mapped using the technique presented in Sec. 7.3.2. This provides a check of the relative CMEF strengths at the position of the axial magnetic minimum ($z = 0$) and ensures that no unfortunate nodes in the field exist at this position. Figure 8.4 plots these maps, showing comparable CMEF strengths at $z = 0$.

Before each attempt of an on resonance, off resonance, or no microwaves experiment, the minimum cyclotron frequency is measured to set and ensure the correct

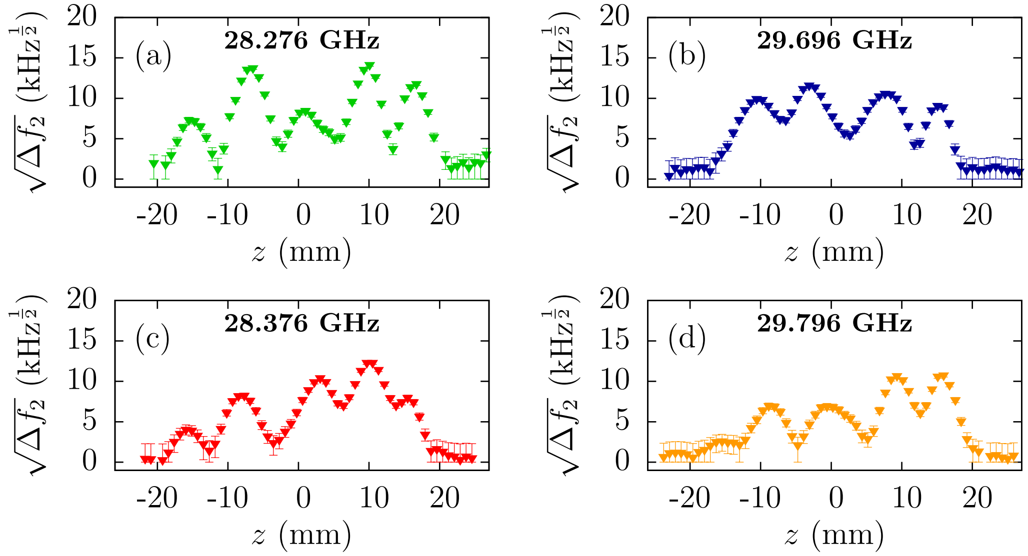

Figure 8.4: The square root of the quadrupole frequency shift, which is proportional to the local CMEF amplitude, measured as a function of position (using the technique presented in Sec. 7.3.2) at microwave frequencies of: (a) 28.276 GHz (b) 29.696 GHz (c) 28.376 GHz and (d) 29.796 GHz. Corrections for the spheroidal plasma shape and the changing magnetic gradient slope have not been applied here.

magnetic field setting. The potential -40 MHz offset between the true minimum cyclotron frequency and the measured minimum with the full neutral trap is an obvious concern here (see Sec. 7.2.2). Without a clear way to rule out this effect it was decided to assume the offset exists. The magnetic field was therefore set by measuring the minimum cyclotron frequency with the mirror coils at their standard trapping currents but with the octupole off. The minimum cyclotron resonance when the octupole is added should then be shifted up from this resonance by 40 MHz. While this offset may not exist, sitting above the minimum resonance would still result in a probability of inducing a spin flip while sitting 40 MHz below resonance would not. The target cyclotron frequency is 692.8 MHz above f_{cb} and 727.6 MHz below f_{da}. If necessary, the magnetic field is adjusted by changing the Penning trap solenoid current. The magnetic field between experiments is stable to within roughly 0.07 mT or 2 MHz in microwave frequency as set by the reproducibility of current in the mirror coils.

8.3 Detection of PSR transitions

From each series of measurements, two types of annihilation data were collected. At the end of every experiment, following the 180 s microwave window, the trapping fields were rapidly turned off to detect the annihilation of any remaining trapped antihydrogen atoms. A detection window of 30 ms was monitored for annihilation events and an effective trapping rate per attempt was measured for each series. When the microwave sweeps are on resonance the antihydrogen atoms should be ejected before the trap is shut down, reducing this rate. This method of search for a signal of resonant positron spin flips is referred to as the 'disappearance mode'. Within the 30 ms detection window after the trap shutdown, annihilations were identified by the standard set of selection criteria outlined in Sec. 5.2.1. The overall annihilation detection efficiency is 58 ± 7% with a background (due to noise and cosmic rays) rate of $(4.7 \pm .2) \times 10^{-2}$ events per second (0.14 background events expected in 100 attempts).

Complementary to the disappearance mode is the 'appearance mode' wherein annihilation events were monitored during the 180 s window. Resonant microwaves will flip the positron spin, putting the antihydrogen atom in an untrapped state that will quickly annihilate on the trap walls. In contrast, attempts with off resonance microwaves (or no microwaves) should not result in any events above background. Because the observation window is much longer than the disappearance mode window, an alternative set of acceptance criteria was developed. Like the standard annihilation event criteria, this approach uses variables related to the event topology to distinguish between annihilation and background events [6]. Annihilation events are separated from background events, based on these variables, using a machine-learning approach known as the Random Forest method [139, 140]. The Random Forest method distinguishes signal from background by training a number of decision trees using a chosen figure of merit. The training data-sets used for this algorithm are similar to those used for the standard selection criteria. A signal data-set is collected from annihilations during the mixing phase of a set of antihydrogen trapping attempts and the background data-set consists of readout from the silicon detector while the neutral atom trap magnets are engaged but no particles are present in the trap. The figure of merit used for training is known as the ‘Punzi figure of merit’ [141] given by $s/(N_\sigma/2+\sqrt{N_\mathrm{B}})$, where s is the signal efficiency, N_B is the expected number of background events, and N_σ is the desired level of significance, taken here to be 3. After training, the optimized set of selection criteria accept 25% fewer annihilation events compared to the standard selection criteria but reject background events roughly 10 times more efficiently [6]. In addition to satisfying the optimized selection criteria, appearance mode annihilation events must have an axial position within 6 cm of trap centre. This cut is motivated by the fact that the microwave fields are resonant only when the antihydrogen atoms pass through $z = 0$. The choice of 6 cm is based on simulations of the annihilation position of antihydrogen atoms that undergo a positron spin flip transition. With this final cut, the background rate is suppressed by a further factor of 3, resulting in a overall rate of only $(1.7 \pm 0.3) \times 10^{-3}$ s^{-1} [6]. As with the standard selection criteria, the optimized selection criteria were finalized before analyzing the appearance mode data-sets to avoid experimenter bias.

8.4 Results

8.4.1 Disappearance Mode

Table 8.1 summarizes the disappearance mode results of series 1 - 6. These results are analyzed by evaluating the probability (P-value) that the observed number of antihydrogen annihilations in a ‘signal’ series could be the result of statistical fluctuation of ‘background’ alone (see [79]). In this case, ‘signal’ refers to on resonance experi-

Series	Microwave Frequencies	Magnetic Field	# of Attempts	# of Annihilations	Rate	Type
1	$f_{cb}^{\mathrm{A}}, f_{da}^{\mathrm{A}}$	B^{A}	79	1	0.01 ± 0.01	On resonance
2	$f_{cb}^{\mathrm{A}}, f_{da}^{\mathrm{A}}$	B^{B}	88	16	0.18 ± 0.05	Off resonance
3	$f_{cb}^{\mathrm{B}}, f_{da}^{\mathrm{B}}$	B^{B}	24	1	0.04 ± 0.04	On resonance
4	$f_{cb}^{\mathrm{A}}, f_{da}^{\mathrm{A}}$	B^{B}	22	7	0.32 ± 0.12	Off resonance
5	Off	B^{A}	52	17	0.33 ± 0.08	No microwaves
6	Off	B^{B}	48	23	0.48 ± 0.10	No microwaves

Table 8.1: Summary of the disappearance mode results for each series in the PSR experiment. Data reproduced with permission from [6].

ments and 'background' to off resonance experiments. The survival rate of series 1 (on resonance) is compared to series 3 (off resonance) and series 2 (on resonance) is compared to series 4 (off resonance). These two pairs of measurements may be subject to different systematic effects. In series 1 and 2, the resonance is shifted by changing the mirror magnetic field, potentially altering the dynamics of trapped antihydrogen atoms; although this is not supported by numerical simulations of the dynamics. In series 3 and 4, on the other hand, the magnetic field is the same but the microwave frequency is changed. This could result in different microwave field characteristics between the two series, although no significant difference between the fields was observed in Sec. 8.2. Even if the systematics differ, however, both pairs of measurements show a decrease in the on resonance event rate per attempt compared to the off resonance measurements with P-values of 1.6×10^{-4} (series 1/3) and 1.5×10^{-2} (series 2/4), consistent with the observation of resonant positron spin flips. Table 8.2 summarizes the results in terms of the measurement type. The overall survival rate of antihydrogen atoms in on resonance experiments shows a clear decrease compared to off resonance experiments, with a P-value of 1×10^{-5}.

It is also interesting to note that the survival rate in off resonance measurements is lower than the experiments without microwaves (with a P-value of 6×10^{-3}). This difference can be explained by the finite probability of inducing $|c\rangle \rightarrow |b\rangle$ transitions in the off resonant experiments (see Fig. 8.3(b)).

Type	Attempts	Annihilations	Rate
On resonance (1 + 3)	103	2	0.02 ± 0.01
Off resonance (2 + 4)	110	23	0.21 ± 0.04
No microwaves (5 + 6)	100	40	0.40 ± 0.06

Table 8.2: Total number of annihilation events and overall rate per attempt for each type of measurement in the PSR experiment. Data reproduced with permission from [6].

8.4.2 Appearance Mode

Figure 8.5 summarizes the appearance mode results by plotting the number of events satisfying the alternative criteria as a function of time. Each bin in Fig. 8.5 covers a 15 MHz sweep around either target frequency, starting at $t = 0$ with f_{cb}. A significant excess of on resonance events over off resonance events are observed during the first set of frequency sweeps (between $t = 0$ s and $t = 30$ s) with a P-value of 2.8×10^{-5}. In the first sweep over the $|c\rangle \rightarrow |b\rangle$ transition, 7 of the 19 events come within the first second. Similarly, 7 of 18 events in the first sweep over the $|d\rangle \rightarrow |a\rangle$ transition occur in the first second. This is consistent with an estimate of the transition rate based on the measured CMEF amplitude and numerical simulations (Sec. 8.2) .

A small excess of annihilation events above the no microwave case is observed in the off resonance measurements with a P-value of 5.6×10^{-2}. This is consistent with the difference between these experiments observed in the disappearance mode. The fact that the majority of these off resonance events occur between $t = 15$ s and $t = 30$ s, when the microwaves are sweeping over the upper frequency band (see Fig. 8.3(b)), provides additional confidence that they are due to $|c\rangle \rightarrow |b\rangle$ transitions.

8.4.3 Conclusion

It is difficult to envision a process other than resonant positron spin flips that could produce these results. The only plausible alternative is a vacuum effect due to the observed heating of the electrodes from 8 K to 11 K by the microwaves. This small

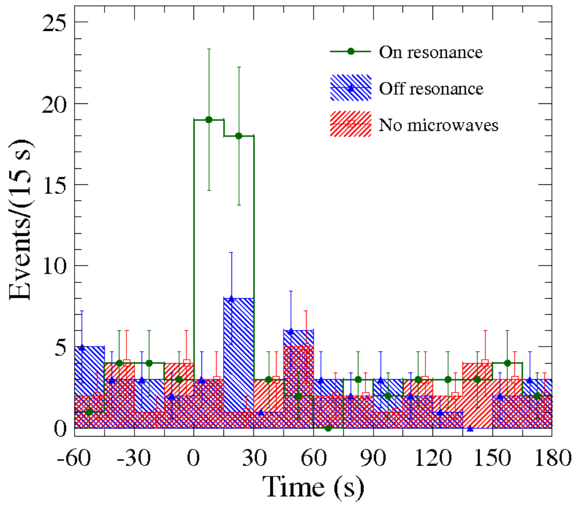

Figure 8.5: A summary of the appearance mode results of the PSR experiment. The number of events satisfying the alternative selection criteria is plotted as a function of time between the end of antihydrogen production and the trap shutdown. The 180 s microwave window starts at $t = 0$ s. The expected number of background events in each 15 s bin is approximately 2.7. The error bars are due to counting statistics.

temperature change could result in desorption of cryo-pumped material from the electrode surface, which could then scatter or annihilate antihydrogen atoms. Such a vacuum effect, however, would be identical in series 1 and 2, as only the magnetic field is changed between the experiments. Furthermore, a vacuum effect would evenly apply throughout the trapping volume. This is inconsistent with the observed axial distribution of the annihilations (Fig. 8.6). The annihilations are highly localized at the axial centre, consistent with simulations of the annihilation position of spin flipped antihydrogen atoms [6].

It is therefore concluded that resonant positron spin flip transitions have been induced in trapped antihydrogen atoms. This experiment is a proof of principle demonstration rather than an attempt to accurately measure the transition frequencies or the resonance lineshapes. By demonstrating that the transition frequencies fall between the off resonance frequency sweep and the on resonance frequency sweep, they have been bounded to within 100 MHz (4 parts in 10^{-3}) of the expected hydro-

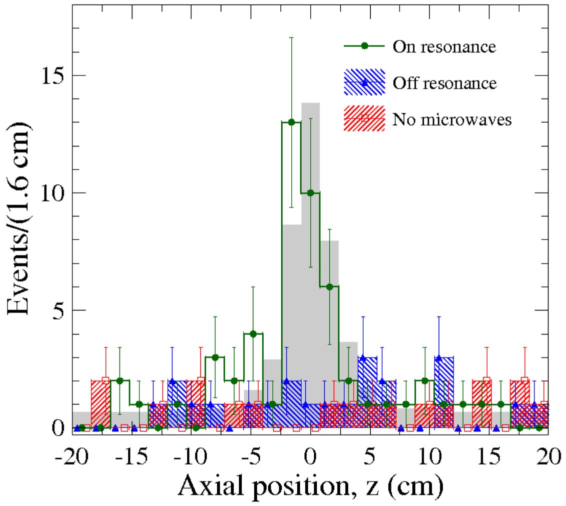

Figure 8.6: A plot of the number of events satisfying the alternative selection criteria as a function of axial position in the PSR experiment. The $|z| < 6$ cm requirement is not imposed here. The grey histogram shows the results of simulations of the annihilation position of spin flipped antihydrogen atoms.

gen resonance frequencies. This experiment is also an important demonstration of the viability of performing measurements on small numbers of trapped antihydrogen atoms and a testament to the power of ALPHA's silicon vertex detector.

Chapter 9

Outlook

This thesis has described the realization of both the first ever trapping of antihydrogen [5] as well as the first resonant interaction with antihydrogen's internal quantum state [6]. Antihydrogen trapping was made possible by a number of important advancements and studies including: evaporative cooling of charged plasmas [50], autoresonant excitation of antiproton plasmas [51], and detailed studies of annihilation signals and rejection of background [78, 79, 118]. Since the initial demonstration of antihydrogen trapping, over 400 antihydrogen atoms have been trapped and confinement times of up to 1000 s have been demonstrated [52]. With the ability to trap antihydrogen atoms, and the development of important *in situ* diagnostic tools [53], ALPHA was able to perform a first proof-of-principle experiment demonstrating the induction of positron spin flip transitions between ground state hyperfine levels. The author was fully involved in all of the aformentioned results (and all publications listed on pages vi – ix). As part of a smaller group within ALPHA, the author played a critical role in the positron spin flip experiment as well as leading the development of the *in situ* diagnostic tools that made that work possible.

With these successes, the ALPHA experiment is now in a transition period. ALPHA's focus shifted from the trapping of antihydrogen towards the study and spectroscopy of trapped antihydrogen atoms. In addition to taking the first steps towards spectroscopy, ALPHA has recently conducted the first study of the gravitational mass of antihydrogen by analyzing the vertical annihilation positions of 434 previously trapped antihydrogen atoms upon trap shutdown [142]. This study was able to rule out anomalous gravitational masses of antihydrogen that are greater than a factor of 110 times that of hydrogen or below a factor of -65 times (the negative sign implying a negative gravitational mass) that of hydrogen. While these bounds are large, future improvements to the antihydrogen trapping rate and the usage of antihydrogen cooling techniques should allow for substantial improvements to the measurement. Studies such as this are enabled by the position sensitive silicon detector that was also critical in the demonstration of antihydrogen trapping and of positron spin flip transitions.

9.1 ALPHA-2

To make the transition towards antihydrogen spectroscopy, the ALPHA collaboration is now in the process of constructing a new apparatus, known as ALPHA-2. The design of ALPHA-2 is similar to the original ALPHA design with some key additions and improvements. The most significant addition to ALPHA-2 is the inclusion of optical access to the Penning trap that will allow for laser spectroscopy and laser cooling of antihydrogen. There are four laser access paths that cross at the centre of the Penning trap, which is also the minimum of the magnetic neutral atom trap (see Fig. 9.1). By having four potential laser paths, each can be dedicated to a different task. Improvements have also been made to the neutral atom trap design that will benefit microwave spectroscopy of antihydrogen. The ALPHA-2 neutral atom trap features three additional mirror coils that can flatten the magnetic field around the minimum while maintaining the neutral atom trap depth.

Another significant aspect of the ALPHA-2 design is the addition of a second Pen-

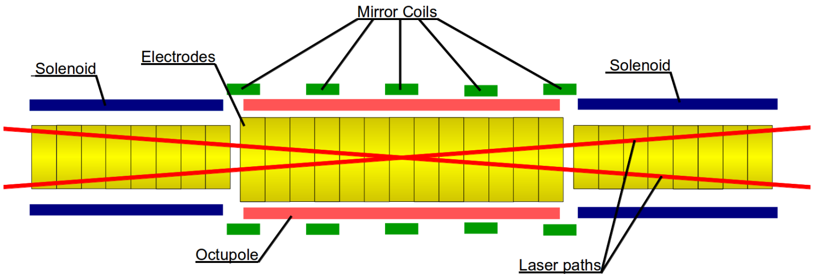

Figure 9.1: A side view sketch of the main ALPHA-2 Penning trap and neutral atom trap designed for trapping and studying of antihydrogen. The apparatus features laser access for a total of four beams that cross at the centre of the Penning trap, coinciding with the minimum of the magnetic neutral atom trap.

ning trap dedicated to antiproton catching and accumulation. This smaller Penning trap is designed to catch, cool, and manipulate antiprotons delivered by the antiproton decelerator. The ALPHA-2 catching trap will allow every antiproton bunch from the AD (roughly every 100 s) to be captured without impacting precision experiments on antihydrogen in the main Penning trap. Because experiments on antihydrogen have typically taken roughly 15 minutes (from antiproton capture to magnetic trap shutdown) this will greatly increase the number of usable antiprotons.

9.2 Trapping

Any experiment studying antihydrogen will be limited by the low trapping rates that have thus far been achieved. The fewer antihydrogen atoms that are trapped per attempt, the longer it will take to demonstrate any effect (e.g. positron spin flips, 1S - 2S transitions, gravitational interaction, etc.). Collecting enough statistics to confirm or rule out suspected systematic effects can therefore be massively time consuming. The thermal energy of the antiproton and positron plasmas appears to be a limiting factor in the number of trappable antihydrogen atoms formed. Given that the Penning trap electrode surfaces are measured to be at approximately 7.5 K one would expect the plasmas to come into equilibrium at 7.5 K, assuming there are no additional heating sources. Unfortunately, equilibrium temperatures colder than roughly 40 K have not been achieved thus far. Evaporative cooling can bring plasma temperatures to roughly 10 K but reheating is always observed. The source of this heating remains an open question.

Another way to increase the number of trappable antihydrogen atoms is to simply use more antiprotons. The number of antiprotons that are mixed to form antihydrogen is currently limited by the number of antiprotons captured upon injection from the AD. To increase the number of usable antiprotons, and to accommodate the increasing demand for antiprotons from new experiments at CERN, a small circular accelerator will be constructed within the AD hall. The ring, known as ELENA (Extra Low ENergy Antiprotons), will further decelerate antiprotons from 5.3 MeV to a target energy of 100 keV [49]. The reduced energy of the antiproton bunches are expected to result in a factor of 10 to 100 times more antiprotons captured by experiments like ALPHA. ELENA will also have the capacity to deliver antiproton bunches to multiple experiments simultaneously. ELENA is scheduled to begin delivering reduced energy antiprotons to experiments around the year 2017. In addition to ELENA, the dedicated antiproton catching trap will also greatly increase the number of antiprotons available to form antihydrogen.

Even with increases in the trapping rate of one or two orders of magnitude, future experiments will still be operating with very small numbers of anti-atoms (especially when compared to typical matter spectroscopy experiments). The success of the positron spin flip experiment and the gravitational study, however, demonstrate that meaningful physics experiments can still be made on small numbers of anti-atoms. The methods employed by ALPHA for these experiments will no doubt be extremely useful in future microwave and laser spectroscopy experiments.

9.3 Hyperfine Spectroscopy

The demonstration of induced positron spin flips between antihydrogen's ground states is an important first step towards true hyperfine spectroscopy of antihydrogen. An ultimate goal of antihydrogen experiments is to measure the frequency of the zero-field hyperfine splitting to within the same precision as reached with hydrogen (1.4 parts in 10^{12}). The next major step towards this goal is to map out the lineshapes of the positron spin flip transitions so that the difference between the two transition frequencies (which is equivalent to the zero-field hyperfine splitting) can be precisely determined. Because the microwave field can change drastically as a function of frequency, the lineshapes should be mapped out by changing the resonant frequency of the atoms rather than the frequency of the microwaves. This can be accomplished by changing the current in the Penning trap solenoid. In ALPHA-1 this was not possible due to hardware constraints but will be required to properly measure the resonance lineshapes. One of the factors that will limit the achievable resolution is the inhomogeneity of the neutral atom trap magnetic fields. With the ALPHA-1 magnetic fields, this limits the precision of the measurement to roughly 1 part in 10^6, assuming a high trapping rate. The additional mirror coils featured in the ALPHA-2 trap will allow the magnetic field to be flattened around the minimum to increase the achievable resolution by roughly an order of magnitude.

In the long term, the zero-field hyperfine splitting can be determined more accurately by measuring the antiproton spin flip frequencies rather than the positron spin flip transitions. These antiproton spin flip transition (also known as NMR transitions) frequencies pass through a broad maximum at a magnetic field of approximately 0.65 T, making the frequency much less sensitive to the magnetic field than the PSR transition frequencies. The wavelength of the NMR transitions at 0.65 T, however, is roughly 45 cm; well above the cutoff wavelength of the 2.25 cm radius Penning trap electrodes. A microwave cavity is therefore required to excite these transitions. Designing a cavity that can be incorporated into the Penning trap without compromising the ability to store and manipulate charged plasmas presents a technical challenge. It is hoped that a future upgrade to ALPHA-2 will include the addition of such a cavity.

The resolution of hyperfine spectroscopy of antihydrogen also depends on how precise the magnetic field can be measured. The electron cyclotron frequency measurements can determine the static magnetic field strength to within 3.4 parts in 10^4, with a potential systematic offset of 1.4 parts in 10^3 at the moment. With hardware improvements (e.g. flatter magnetic field, microwave cavity for cyclotron frequencies) this could be improved to a level of one part in 10^6, comparable to the magnetic field homogeneity in the ALPHA-1 magnetic trap.

9.4 Conclusion

With the successful trapping of antihydrogen by ALPHA and ATRAP, the construction of the ALPHA-2 apparatus, and with the new AeGIS experiment coming online, the field of antihydrogen research is entering an exciting new phase where the focus has shifted from trapping to studying antihydrogen. True precision measurements on antihydrogen are still a number of years away, but ALPHA's proof-of-principle PSR experiment represents a significant first step toward that goal.

Bibliography

[1] C. G. Parthey *et al.*, Phys. Rev. Lett. **107**, 203001 (2011).

[2] H. Hellwig *et al.*, IEEE Trans. Instrum. Meas. **19**, 200 (1970).

[3] G. Lüders, Ann. Phys. **2**, 1 (1957).

[4] M. Amoretti *et al.*, (ATHENA Collaboration), Nature **419**, 456 (2002).

[5] G. B. Andresen *et al.*, (ALPHA Collaboration), Nature **468**, 673 (2010).

[6] C. Amole *et al.*, (ALPHA Collaboration), Nature **483**, 439 (2012).

[7] C. S. Wu, E. Ambler, R. W. Hayward, D. D. Hoppes, and R. P. Hudson, Phys. Rev. **105**, 1413 (1957).

[8] J. H. Christenson, J. W. Cronin, V. L. Fitch, and R. Turlay, Phys. Rev. Lett. **13**, 138 (1964).

[9] B. Aubert *et al.*, (BABAR Collaboration), Phys. Rev. Lett. **86**, 2515 (2001).

[10] K. Abe *et al.*, (Belle Collaboration), Phys. Rev. Lett. **87**, 091802 (2001).

[11] J. P. Lees *et al.*, (The BABAR Collaboration), Phys. Rev. Lett. **109**, 211801 (2012).

[12] A. Angelopoulos *et al.*, Phys. Lett. B **471**, 332 (1999).

[13] M. S. Fee *et al.*, Phys. Rev. A **48**, 192 (1993).

[14] R. J. Hughes and B. I. Deutch, Phys. Rev. Lett. **69**, 578 (1992).

[15] R. S. Van Dyck, P. B. Schwinberg, and H. G. Dehmelt, Phys. Rev. Lett. **59**, 26 (1987).

[16] M. Hori *et al.*, Nature **475**, 484 (2011).

[17] J. Beringer *et al.*, (Particle Data Group), Phys. Rev. D **86**, 010001 (2012).

[18] D. Colladay and V. A. Kostelecký, Phys. Rev. D **55**, 6760 (1997).

[19] R. Bluhm, V. A. Kostelecký, and N. Russell, Phys. Rev. Lett. **82**, 2254 (1999).

[20] R. Hughes, Nucl. Phys. A **558**, 605 (1993).

[21] P. A. M. Dirac, Proc. R. Soc. Lond. A **117**, 610 (1928).

[22] P. A. M. Dirac, Proc. R. Soc. Lond. A **133**, 60 (1931).

[23] C. D. Anderson, Science **76**, 238 (1932).

[24] C. D. Anderson, Phys. Rev. **43**, 491 (1933).

[25] O. Chamberlain, E. Segrè, C. Wiegand, and T. Ypsilantis, Phys. Rev. **100**, 947 (1955).

[26] G. Baur *et al.*, Phys. Lett. B **368**, 251 (1996).

[27] G. Blanford *et al.*, Phys. Rev. Lett. **80**, 3037 (1998).

[28] G. Gabrielse *et al.*, (ATRAP Collaboration), Phys. Rev. Lett. **63**, 1360 (1989).

[29] M. Holzscheiter *et al.*, Phys. Lett. A **214**, 279 (1996).

[30] X. Feng, M. Holzscheiter, R. Lewis, R. Newton, and M. Schauer, Hyperfine Interact. **100**, 103 (1996).

[31] H. Kalinowsky, Sov. J. Nucl. Phys. **55**, 848 (1992).

[32] G. Gabrielse *et al.*, (ATRAP Collaboration), Phys. Rev. Lett. **89**, 213401 (2002).

[33] M. Amoretti *et al.*, (ATHENA Collaboration), Phys. Lett. B **590**, 133 (2004).

[34] M. Amoretti *et al.*, (ATHENA Collaboration), Phys. Lett. B **583**, 59 (2004).

[35] G. Gabrielse *et al.*, (ATRAP Collaboration), Phys. Rev. Lett. **93**, 073401 (2004).

[36] D. E. Pritchard, Phys. Rev. Lett. **51**, 1336 (1983).

[37] G. Andresen *et al.*, (ALPHA Collaboration), Phys. Rev. Lett. **98**, 023402 (2007).

[38] G. Andresen *et al.*, (ALPHA Collaboration), Phys. Lett. B **685**, 141 (2010).

[39] G. Gabrielse *et al.*, (ATRAP Collaboration), Phys. Rev. Lett. **98**, 113002 (2007).

[40] G. Gabrielse *et al.*, (ATRAP Collaboration), Phys. Rev. Lett. **100**, 113001 (2008).

[41] G. B. Andresen *et al.*, (ALPHA Collaboration), Phys. Plasmas **15**, 032107 (2008).

[42] G. B. Andresen *et al.*, (ALPHA Collaboration), Phys. Rev. Lett. **100**, 203401 (2008).

[43] G. B. Andresen *et al.*, (ALPHA Collaboration), Rev. Sci. Instrum. **80**, 123701 (2009).

[44] A. Speck *et al.*, (ATRAP Collaboration), Phys. Lett. B **650**, 119 (2007).

[45] G. Gabrielse *et al.*, (ATRAP Collaboration), Phys. Lett. B **548**, 140 (2002).

[46] Y. Enomoto *et al.*, Phys. Rev. Lett. **105**, 243401 (2010).

[47] M. Doser *et al.*, (AEGIS Collaboration), Classical Quant. Grav. **29**, 184009 (2012).

[48] P. Perez and Y. Sacquin, Classical Quant. Grav. **29**, 184008 (2012).

[49] W. Oelert, T. Eriksson, P. Belochitskii, and G. Tranquille, Hyperfine Interact. **213**, 227 (2012).

[50] G. B. Andresen *et al.*, (ALPHA Collaboration), Phys. Rev. Lett. **105**, 013003 (2010).

[51] G. B. Andresen *et al.*, (ALPHA Collaboration), Phys. Rev. Lett. **106**, 025002 (2011).

[52] G. B. Andresen *et al.*, (ALPHA collaboration), Nat. Phys. **7**, 558 (2011).

[53] C. Amole *et al.*, (ALPHA Collaboration), New J. Phys. **16**, 013037 (2014).

[54] D. Möhl, Hyperfine Interact. **109**, 33 (1997).

[55] T. J. Murphy and C. M. Surko, Phys. Rev. A **46**, 5696 (1992).

[56] S. Maury, Hyperfine Interact. **109**, 43 (1997).

[57] D. Möhl and A. M. Sessler, Nucl. Instr. Meth. A **532**, 1 (2004).

[58] S. van der Meer, Rev. Mod. Phys. **57**, 689 (1985).

[59] G. Budker, Sov. Atom. Energy **22**, 438 (1967).

[60] H. Poth, Phys. Rep. **196**, 135 (1990).

[61] M. Charlton and J. Humberston, *Positron Physics* (Cambridge University Press, 2001).

[62] M. H. Holzscheiter, M. Charlton, and M. M. Nieto, Phys. Rep. **402**, 1 (2004).

[63] C. Amole *et al.*, (ALPHA collaboration), Nucl. Instrum. Meth. A **735**, 319 (2014).

[64] R. S. Van Dyck and P. B. Schwinberg, Phys. Rev. Lett. **47**, 395 (1981).

[65] M. Mukherjee *et al.*, Eur. Phys. J. A **35**, 1 (2008).

[66] D. Hanneke, S. Fogwell, and G. Gabrielse, Phys. Rev. Lett. **100**, 120801 (2008).

[67] J. DiSciacca and G. Gabrielse, Phys. Rev. Lett. **108**, 153001 (2012).

[68] D. J. Heinzen, J. J. Bollinger, F. L. Moore, W. M. Itano, and D. J. Wineland, Phys. Rev. Lett. **66**, 2080 (1991).

[69] D. H. E. Dubin and T. M. O'Neil, Rev. Mod. Phys. **71**, 87 (1999).

[70] L. S. Brown and G. Gabrielse, Rev. Mod. Phys. **58**, 233 (1986).

[71] J. H. Malmberg and C. F. Driscoll, Phys. Rev. Lett. **44**, 654 (1980).

[72] X.-P. Huang, F. Anderegg, E. M. Hollmann, C. F. Driscoll, and T. M. O'Neil, Phys. Rev. Lett. **78**, 875 (1997).

[73] W. H. Wing, Prog. Quant. Electron. **8**, 181 (1984).

[74] J. Fajans, W. Bertsche, K. Burke, S. F. Chapman, and D. P. van der Werf, Phys. Rev. Lett. **95**, 155001 (2005).

[75] W. Bertsche *et al.*, Nucl. Inst. Meth. A **566**, 746 (2006).

[76] E. Butler, *Antihydrogen formation, dynamics, and trapping*, PhD thesis, Swansea University, 2010.

[77] S. Orfanidis and V. Rittenberg, Nucl. Phys. B **59**, 570 (1973).

[78] G. Andresen *et al.*, (ALPHA collaboration), Phys. Lett. B **695**, 95 (2011).

[79] G. Andresen *et al.*, (ALPHA Collaboration), Nucl. Inst. Meth. A **684**, 73 (2012).

[80] R. Hydomako, *Detection of Trapped Antihydrogen*, PhD thesis, University of Calgary, 2011.

[81] R. Hydomako, *Detection of Trapped Antihydrogen*, Springer Theses (Springer, 2012).

[82] R. W. Gould and M. A. LaPointe, Phys. Rev. Lett. **67**, 3685 (1991).

[83] J. J. Bollinger *et al.*, Phys. Rev. A **48**, 525 (1993).

[84] F. Anderegg, C. F. Driscoll, D. H. E. Dubin, T. M. O'Neil, and F. Valentini, Phys. Plasmas **16**, 055705 (2009).

[85] D. H. E. Dubin, Phys. Rev. Lett. **66**, 2076 (1991).

[86] M. E. Glinsky, T. M. O'Neil, M. N. Rosenbluth, K. Tsuruta, and S. Ichimaru, Phys. Fluids B **4**, 1156 (1992).

[87] T. M. O'Neil and P. G. Hjorth, Phys. Fluids **28**, 3241 (1985).

[88] M. D. Tinkle, R. G. Greaves, C. M. Surko, R. L. Spencer, and G. W. Mason, Phys. Rev. Lett. **72**, 352 (1994).

[89] M. D. Tinkle, R. G. Greaves, and C. M. Surko, Phys. Plasmas **2**, 2880 (1995).

[90] D. L. Eggleston, C. F. Driscoll, B. R. Beck, A. W. Hyatt, and J. H. Malmberg, Phys. Fluids B **4**, 3432 (1992).

[91] M. H. Holzscheiter, Phys. Scripta **46**, 272 (1992).

[92] G. Gabrielse *et al.*, Phys. Rev. Lett. **57**, 2504 (1986).

[93] G. B. Andresen *et al.*, (ALPHA collaboration), J. Phys. B **41**, 011001 (2008).

[94] B. R. Beck, J. Fajans, and J. H. Malmberg, Phys. Plasmas **3**, 1250 (1996).

[95] F. Anderegg, E. M. Hollmann, and C. F. Driscoll, Phys. Rev. Lett. **81**, 4875 (1998).

[96] R. G. Greaves and C. M. Surko, Phys. Rev. Lett. **85**, 1883 (2000).

[97] E. M. Hollmann, F. Anderegg, and C. F. Driscoll, Phys. Plasmas **7**, 2776 (2000).

[98] J. R. Danielson and C. M. Surko, Phys. Rev. Lett. **94**, 035001 (2005).

[99] H. F. Hess, Phys. Rev. B **34**, 3476 (1986).

[100] M. H. Anderson, J. R. Ensher, M. R. Matthews, C. E. Wieman, and E. A. Cornell, Science **269**, 198 (1995).

[101] K. B. Davis *et al.*, Phys. Rev. Lett. **75**, 3969 (1995).

[102] A. E. Leanhardt *et al.*, Science **301**, 1513 (2003).

[103] T. Kinugawa, F. J. Currell, and S. Ohtani, Phys. Scripta **2001**, 102 (2001).

[104] W. Ketterle and N. V. Druten, Adv. At. Mol. Opt. Phys. **37**, 181 (1996).

[105] G. Andresen, *Evaporative cooling of antiprotons and efforts to trap antihydrogen*, PhD thesis, Aarhus University, 2010.

[106] G. Gabrielse, S. Rolston, L. Haarsma, and W. Kells, Phys. Lett. A **129**, 38 (1988).

[107] F. Robicheaux, J. Phys. B **41**, 192001 (2008).

[108] F. Robicheaux, Phys. Rev. A **73**, 033401 (2006).

[109] M. C. Fujiwara *et al.*, (ATHENA Collaboration), Phys. Rev. Lett. **101**, 053401 (2008).

[110] F. Robicheaux, Phys. Rev. A **70**, 022510 (2004).

[111] J. L. Hurt, P. T. Carpenter, C. L. Taylor, and F. Robicheaux, J Phys. B **41**, 165206 (2008).

[112] J. Fajans, E. Gilson, and L. Friedland, Phys. Plasmas **6**, 4497 (1999).

[113] S. J. Peale, Nature **365**, 788 (1993).

[114] W.-K. Liu, B. Wu, and J.-M. Yuan, Phys. Rev. Lett. **75**, 1292 (1995).

[115] A. I. Nicolin, M. H. Jensen, and R. Carretero-González, Phys. Rev. E **75**, 036208 (2007).

[116] M. C. Fujiwara *et al.*, (ATHENA Collaboration), Phys. Rev. Lett. **92**, 065005 (2004).

[117] F. Chen, *Introduction to Plasma Physics and Controlled Fusion: Plasma Physics* (Plenum Press, New York, 1984).

[118] C. Amole *et al.*, (ALPHA collaboration), New J. Phys. **14**, 015010 (2012).

[119] H. F. Hess *et al.*, Phys. Rev. Lett. **59**, 672 (1987).

[120] J. D. Bowman and S. I. Penttila, J. Res. Natl. Inst. Stand. Technol. **110**, 361 (2005).

[121] G. Gabrielse *et al.*, (ATRAP Collaboration), Phys. Rev. Lett. **108**, 113002 (2012).

[122] S. Chapman, *The Effect of Multipole-Enhanced Diffusion on the Joule Heating of a Cold Non-Neutral Plasma*, PhD thesis, University of California, Berkeley, 2011.

[123] T. M. ONeil, Phys. Fluids **23**, 725 (1980).

[124] E. M. Purcell, Phys. Rev. **69**, 674 (1946).

[125] G. Gabrielse and H. Dehmelt, Phys. Rev. Lett. **55**, 67 (1985).

[126] D. Kleppner, Phys. Rev. Lett. **47**, 233 (1981).

[127] N. Evetts and W. Hardy, *Cyclotron Cooling Rates for Trapped Modes in the ALPHA Stack*, ALPHA Internal Communication (2011).

[128] A. G. Marshall, C. L. Hendrickson, and G. S. Jackson, Mass Spectrom. Rev. **17**, 1 (1998).

[129] I. Bergström *et al.*, Nucl. Instrum. Meth. A **487**, 618 (2002).

[130] J. Dilling *et al.*, Int. J. Mass Spectrom. **251**, 198 (2006).

[131] B. Odom, D. Hanneke, B. D'Urso, and G. Gabrielse, Phys. Rev. Lett. **97**, 030801 (2006).

[132] E. Sarid, F. Anderegg, and C. F. Driscoll, Phys. Plasmas **2**, 2895 (1995).

[133] M. Affolter, F. Anderegg, C. F. Driscoll, and D. H. E. Dubin, AIP Conf. Proc. **1521**, 175 (2013).

[134] R. W. Gould, Phys. Plasmas **2**, 1404 (1995).

[135] D. Kleppner, H. M. Goldenberg, and N. F. Ramsey, Phys. Rev. **126**, 603 (1962).

[136] Commercial product from Cobham Technical Services, http://www.cobham.com/technicalservices.

[137] C. L. Cesar, Phys. Rev. A **64**, 023418 (2001).

[138] M. Ashkezari, *Microwave spectroscopy of magnetically trapped atomic antihydrogen*, PhD thesis, Simon Fraser University, 2014, (in progress).

[139] L. Breiman, Machine Learning **45**, 5 (2001).

[140] I. Narsky and H. B. Prosper, Optimization of Signal Significance by Bagging Decision Trees, in *Statistical Problems in Particle Physics, Astrophysics and Cosmology*, edited by L. Lyons and M. Karagöz Ünel, p. 143, 2006.

[141] G. Punzi, arXiv:physics/0308063 .

[142] C. Amole *et al.*, (ALPHA Collaboration), Nat, Commun. **4**, 1785 (2013).